

---


Electronic Theses and Dissertations, 2004-2019

---

2014

## Quantifying Ultra-high Performance Concrete Flexural System Mechanical Response

Yulin Xiao  
*University of Central Florida*

 Part of the [Civil Engineering Commons](#)  
Find similar works at: <https://stars.library.ucf.edu/etd>  
University of Central Florida Libraries <http://library.ucf.edu>

This Doctoral Dissertation (Open Access) is brought to you for free and open access by STARS. It has been accepted for inclusion in Electronic Theses and Dissertations, 2004-2019 by an authorized administrator of STARS. For more information, please contact [STARS@ucf.edu](mailto:STARS@ucf.edu).

---

### STARS Citation

Xiao, Yulin, "Quantifying Ultra-high Performance Concrete Flexural System Mechanical Response" (2014). *Electronic Theses and Dissertations, 2004-2019*. 4854.  
<https://stars.library.ucf.edu/etd/4854>

QUANTIFYING ULTRA-HIGH PERFORMANCE CONCRETE FLEXURAL SYSTEM  
MECHANICAL RESPONSE

by

YULIN XIAO

B.S. Russia St-Petersburg State University of Architecture and Civil Engineering, 2009

M.S. University of Central Florida, 2011, Orlando, FL, US

A dissertation submitted in partial fulfilment of the requirements  
for the degree of Doctor of Philosophy  
in the Department of Civil, Environmental and Construction Engineering  
in the College of Engineering and Computer Science  
at the University of Central Florida

Fall Term  
2014

Major Professor: Kevin R Mackie

© 2014YULIN XIAO

## **ABSTRACT**

The research and application of Ultra-high Performance Concrete (UHPC) has been developed significantly within the last 1-2 decades. Due to the specific property of high strength capacity, it is potential to be used in bridge deck system without shear reinforcement so that it provides even lighter self-weight of the deck. However, one of the shear component, dowel action, has not been adequately investigated in the past. In this dissertation, a particular test was designed and carried out to fully investigate the dowel action response, especially its contribution to shear resistance. In addition, research on serviceability and fatigue behavior were expanded as well delete the concern on other factors that may influence the application to the deck system. Both experimental and analytical methods including finite element modeling, OpenSees modeling and other extension studies were presented throughout the entire dissertation where required.

## **ACKNOWLEDGMENTS**

I would like to express my sincere appreciation to the faculty members at civil engineering department of University of Central Florida for their fully support along my Ph.D studies. More specifically, i would like to express my appreciation to my major advisor Dr Kevin Mackie for his guidance and support to my graduate study. I would also like to thank Dr Necati Catbas, Dr Manoj Chpra, Dr Ali Gordon and Dr Jun Xia for being my committee members. In addition, thank Dr Amir Mirmiran and his entire group at Florida International University for sharing experience and test materials.

In addition, i want to say thanks to the crew of the structures laboratory, specifically Juan Cruz, for his help and support in the testing. A special thanks to my colleagues members such as Elie EI Zghayar, Munaf Al-Ramahee and Mohammad Mehdizadeh for their assistance throughout the past years. Also, thanks Florida Department of Transportation for sponsoring my research project and Larfage Northe America for providing the test materials.

Finally, i would like to thank my wife Xiaoqin Peng and my baby Wilson Xiao for their supports.

# TABLE OF CONTENTS

LIST OF FIGURES . . . . .	ix
LIST OF TABLES . . . . .	xiv
CHAPTER 1: INTRODUCTION . . . . .	1
Background and Motivation . . . . .	1
Objective . . . . .	3
Plan . . . . .	3
Material Introduction . . . . .	4
UHPC . . . . .	5
HSS bar and MMFX . . . . .	7
FRP Bar . . . . .	10
CHAPTER 2: DOWEL ACTION . . . . .	12
Introduction . . . . .	12
Chapter Concept Introduction . . . . .	12
Shear Transfer Mechanisms . . . . .	13

Analytical Methods Overview . . . . .	15
Finite Element Modeling of Dowel Action . . . . .	16
Dowel Action Contribution to Shear Resistance of UHPC Beams . . . . .	17
Experimental Studies . . . . .	19
Specimens Summary . . . . .	19
Specimen Design . . . . .	20
Results . . . . .	22
Theoretical Analysis . . . . .	23
Beam on Elastic Foundation (BEF) . . . . .	23
Beam on Nonlinear Foundation (BNF) . . . . .	28
Chapter Discussion and Conclusions . . . . .	33
 CHAPTER 3: UNIAXIAL FATIGUE INVESTIGATION ON UHPC STRUCTURES . . . . .	 36
Introduction . . . . .	36
Experimental Work . . . . .	40
Analytical Work . . . . .	49
Strain Life Approach . . . . .	52
Peak Strain Method . . . . .	54

Mean Strain Method . . . . .	55
Maximum Vertex Method . . . . .	56
Mean Stress Approach . . . . .	59
Opensees Modeling Approach . . . . .	62
Chapter Conclusion . . . . .	66
CHAPTER 4: MID-SCALE UHPC “T” SECTION BEAMS INVESTIGATION . . . . .	68
Introduction . . . . .	68
Experimental Work . . . . .	69
Results and Discussion . . . . .	73
Bar strength utilization ratio study . . . . .	80
Shear reduction factor study . . . . .	88
Estimation of shear reduction factor with specimens from Cast I . . . . .	89
Verification of shear reduction factor with specimen from Cast II . . . . .	91
Chapter Discussion . . . . .	93
CHAPTER 5: CONCLUSION . . . . .	96
APPENDIX A: SAMPLE UHPC APPLICATIONS WORLDWIDE . . . . .	98



LOUIS VUITTON FOUNDATION FACADE . . . . . 99

SHAWNESSY LIGHT RAIL TRANSIT STATION . . . . . 101

THE JAKWAY PARK BRIDGE . . . . . 101

MARS HILL BRIDGE IN WAPELLO COUNTY . . . . . 103

ARCHITECTURE AND ARTS DESIGN . . . . . 106

THE SHEPHERDS CREEK DUCTAL BRIDGE . . . . . 106

LIST OF REFERENCES . . . . . 110

## LIST OF FIGURES

1.1	UHPC on-site cast and Wapello bridge application . . . . .	8
1.2	Commercially available HSS sample and MMFX sample . . . . .	9
1.3	Structures of equivalent strength with conventional steel and MMFX . . . . .	10
2.1	Dowel action mechanism along the cracked reinforced concrete member . . .	12
2.2	Dowel sample and dowel force distribution along longitudinal direction . . .	13
2.3	Mechanism of shear transfer . . . . .	15
2.4	Experimental specimen geometry and loading setup . . . . .	18
2.5	Load vs displacement curves for beam with and without dowel action . . . .	19
2.6	Block samples before and after failure . . . . .	20
2.7	Detailed specimen test setup . . . . .	21
2.8	Specimen design details and dimension for base group specimen . . . . .	22
2.9	Failure mode of typical specimen . . . . .	24
2.10	Experimental results . . . . .	25
2.11	Load versus table displacement for additional group specimens . . . . .	25
2.12	Test setup and simplified model . . . . .	26

2.13	BNF finite element model . . . . .	28
2.14	Stress and crack width relation for nonlinear spring . . . . .	29
2.15	BNF finite element model results comparison to experiment results . . . . .	30
2.16	Load displacement model for linear and nonlinear foundation . . . . .	31
2.17	Schematic drawing of the BNF model . . . . .	32
2.18	Load versus yielding range for various $\alpha$ values . . . . .	33
3.1	Fatigue Specimen Dimension . . . . .	40
3.2	Test specimens during and after cast . . . . .	41
3.3	Test Setup . . . . .	43
3.4	Failure of strain gage due to concrete surface crack . . . . .	44
3.5	Specimen 3 Strain 1 (front) response at selected cycles . . . . .	45
3.6	Samples of tensile fatigue failure due to steel fiber pulled out . . . . .	46
3.7	Micro-tensile failure verification . . . . .	47
3.8	Stress response under cyclic loading in specimen 2 . . . . .	48
3.9	Stress response under cyclic loading in specimen 8 . . . . .	49
3.10	Compiled tension strain response versus number of cycles in specimen 2 . . . . .	50
3.11	Compiled tension strain response versus number of cycles in specimen 3 . . . . .	51

3.12	Compiled tension strain response versus number of cycles in specimen 8 . . . . .	52
3.13	Estimated fatigue strain life curve of UHPC by peak strain approach . . . . .	56
3.14	Estimated fatigue strain life curve of UHPC by mean strain approach . . . . .	57
3.15	Illustration of strain gages and maximum vertices strain locations . . . . .	59
3.16	Estimated fatigue strain life curve of UHPC by max vertices strain method . . . . .	60
3.17	Estimated fatigue strain life curve of UHPC by mean stress approach . . . . .	61
3.18	Comparison of estimated strain vs Nf from all presented approaches . . . . .	62
3.19	Strain strain relationship adopted for Opensees modeling . . . . .	63
3.20	Predicted fatigue force vs number of cycles of failure for sp6 . . . . .	64
3.21	Predicted fatigue force vs displacement for sp6 . . . . .	64
3.22	Predicted fatigue moment Mx vs displacement for sp6 . . . . .	65
3.23	Predicted fatigue moment Mz vs displacement for sp6 . . . . .	65
4.1	Designated beam with cross section details . . . . .	69
4.2	3D simulation for section 1 “UHPC-CFRP” . . . . .	71
4.3	Designed MMFX reinforcing system layout . . . . .	71
4.4	Designed CFRP reinforcing system layout (h=5’ sample) . . . . .	72
4.5	Anchorage processing for CFRP specimens before and after test . . . . .	72

4.6	String pots instrumentation . . . . .	73
4.7	Test setup and instrumentation of “UHPC-MMFX” specimen . . . . .	74
4.8	Crack observation for “UHPC-MMFX” specimens . . . . .	74
4.9	“UHPC-MMFX” specimen prior to failure . . . . .	75
4.10	CFRP cracks . . . . .	75
4.11	Load vs displacement for “UHPC-MMFX” specimens . . . . .	76
4.12	Load vs displacement for “UHPC-CFRP” specimens in 4’ height . . . . .	77
4.13	Load vs displacement for “UHPC-CFRP” specimens in 5’ height . . . . .	77
4.14	Load vs strain for “UHPC-MMFX” specimens . . . . .	78
4.15	Load vs strain for “UHPC-MMFX” specimens in 4’ height . . . . .	79
4.16	Load vs strain for “UHPC-MMFX” specimens in 5’ height . . . . .	79
4.17	MMFX reinforced section with moment illustration . . . . .	81
4.18	MMFX reinforced beam section analysis . . . . .	82
4.19	CFRP reinforced beam section analysis . . . . .	84
4.20	Optimized section property for the second cast . . . . .	87
4.21	Load vs displacement compared with CFRP and MMFX beams at cast II . . . . .	87
4.22	Stress-strain of UHPC adopted in OpenSees model . . . . .	89

4.23	Stress-strain relationship of MMFX adopted in OpenSees model . . . . .	90
4.24	Simulated moment curvature of MMFX reinforced UHPC “T” section . . . . .	90
4.25	Simulated moment curvature of optimized MMFX reinforced “T” section . . . . .	92
4.26	Load vs displacement of CFRP and MMFX system at both two casts . . . . .	95
1	LOUIS VUITTON FOUNDATION OVERVIEW PHOTO 1 . . . . .	100
2	LOUIS VUITTON FOUNDATION OVERVIEW PHOTO 2 . . . . .	100
3	THE SHAWNESSY LIGHT RAIL TRANSIT STATION PHOTO 1 . . . . .	102
4	THE SHAWNESSY LIGHT RAIL TRANSIT STATION PHOTO 2 . . . . .	103
5	THE JAKWAY PARK BRIDGE PHOTO 1 . . . . .	103
6	THE JAKWAY PARK BRIDGE PHOTO 2 . . . . .	104
7	MARS HILL BRIDGE IN WAPELLO COUNTY PHOTO 1 . . . . .	105
8	MARS HILL BRIDGE IN WAPELLO COUNTY PHOTO 2 . . . . .	105
9	BUS SHELTERS MADE OF UHPC . . . . .	107
10	BMI AZULY STREET FURNITURE MADE OF UHPC . . . . .	107
11	THE SHEPHERDS CREEK DUCTAL BRIDGE PHOTO 1 . . . . .	109
12	THE SHEPHERDS CREEK DUCTAL BRIDGE PHOTO 2 . . . . .	109

## LIST OF TABLES

1.1	United States Bridge Statistics . . . . .	1
1.2	Comparison of Characteristics of Different Types of Concrete . . . . .	6
1.3	Basic Components of UHPC . . . . .	7
1.4	Components and Property of the 1st Express Way UHPC Bridge in France . . . . .	8
1.5	Typical MMFX Chemical Composition . . . . .	10
2.1	Shear transfer mechanisms (NSC) . . . . .	14
2.2	Compression strength of specimen . . . . .	20
2.3	Designed specimen with comparison groups . . . . .	22
2.4	Peak dowel load from different groups . . . . .	23
2.5	Peak dowel load from base group and group with bar concrete bonded . . . . .	23
2.6	Results from the BEF analysis . . . . .	28
3.1	Fatigue load classes and applications . . . . .	37
3.2	Specimen History Record . . . . .	41
3.3	Specimen testing matrix with achieved stress ranges . . . . .	42
3.4	Maximum tensile and compressive strain readings for all valid specimens . . . . .	45

3.5	Calculated fatigue exponent b from maximum strain approach . . . . .	55
3.6	Calculated fatigue exponent b from mean strain approach . . . . .	57
3.7	Calculated fatigue exponent b from maximum vertices strain method . . . . .	59
3.8	Calculated fatigue exponent b from mean stress approach . . . . .	61
4.1	Designated T section beams property . . . . .	70
4.2	Test results summary . . . . .	80
4.3	Estimated CFRP bar strength utilization ratio . . . . .	85
4.4	Section property of MMFX-4in specimen at second cast . . . . .	86
4.5	Section property of CFRP-4in specimen at second cast . . . . .	86
4.6	Estimated CFRP bar strength utilization ratio from 2nd cast . . . . .	88
4.7	Estimated shear reduction factors from Cast I specimens . . . . .	91
4.8	Predicted maximum peak load by using estimated shear reduction factor . . .	92
1	SUMMARY OF LOUIS VUITTON FOUNDATION FACADE . . . . .	99
2	SUMMARY OF SHAWNESSY LIGHT RAIL TRANSIT STATION . . . . .	101
3	SUMMARY OF THE JAKWAY PARK BRIDGE . . . . .	102
4	SUMMARY OF MARS HILL BRIDGE IN WAPELLO COUNTY . . . . .	104
5	ARCHITECTURE AND ARTS DESIGN . . . . .	106



6 THE SHEPHERDS CREEK DUCTAL BRIDGE . . . . . 108

# CHAPTER 1: INTRODUCTION

## Background and Motivation

According to American Society of Civil Engineers (ASCE) 2009 report card for America's infrastructure, the state of the country's bridges received a rank of "C". The average age of U.S. bridges is now 45 years which is below the designated 50 years. Of all the approximate 600,000 urban and rural bridges in the country, more than 25% are considered structurally deficient or functionally obsolete [1] Table 1.4. In the state of Florida, the data indicates that 262 of the 11982 bridges are considered structurally deficient and 1764 of the 11982 bridges are considered functionally obsolete. Among all these bridges in Florida, there are 98 movable bridges including 3 lift type, 94 bascule type and 1 swing type bridge which represent one of the largest population of movable bridges in the United States. Despite of the disadvantages such as need of additional expense for machinery, power, and operators, particular maintenance and repair procedures, hazardness in case of emergency, the movable bridge still plays significant role in city planning because of its lower cost due to the absence of high piers and long approaches and less usage of surrounding lands.

Table 1.1: United States Bridge Statistics

	Year 2000	Year 2005	Year 2010
All Bridges	589,674	595,363	604,460
Structurally Deficient Bridges Total	86,692	75,923	69,220
Functionally Obsolete Bridges Total	81,510	80,412	77,412

One of the biggest concerns for movable bridge is the deck system which generally requires periodic rehabilitation or replacement due to increased traffic volumes, demand for heavier semi freight loads, deterioration from corrosion or components fatigue and even pavement widening, etc. Hence, the strength of the deck, thickness of the panel (e.g. the self weight) and fatigue

resistance of the deck system are considered as several of the most important parameters of movable bridge due to the specific operation procedures it works with. While some rehabilitation approaches like deck overlay system applied in the field [2], several alternative deck replacement systems such as adhesively-bonded pultruded fiber reinforced polymer (FRP) deck system, Aluminum extrusions deck system were proposed and investigated as well [3, 4]. However, some concerns like shear strength and heavy self-weight of the deck system remained. A potential solution is to use ultra-high performance concrete (UHPC) in passively-reinforced beams without any shear reinforcement which will bring down the self-weight of the deck significantly as well as increase the system strength because of the ultra high strength property of the material. It is potentially a good choice since tests indicated that the failure mode of beams made of UHPC with longitudinal high strength steel (HSS) rebars under bending exhibited diagonal shear failure rather than the conventional flexural failure. Therefore, the conventional shear reinforcement may be waived due to the particular property of the material.

Then, firstly, how to well predict the shear strength of the UHPC related structures becomes important. Some previous work estimated the ultimate shear capacity [5]; however, the estimation was not accurate due to shortage of shear contribution factor consideration. More experimental and analytical investigations are required to support accurate prediction of the shear strength. To better analyze the entire shear response, each of the shear contribution components such as aggregate interlocking, concrete in compression zone and dowel action, need to be taken into consideration individually. Since dowel action was rarely investigated previously and it is non-ignorable for the situation without applying shear reinforcement, it becomes significant important and worth a detailed investigation. Secondly, the serviceability check is of importance for both live load deflection as well as the fatigue behavior under moving loads represented by United States Department of Transportation (USADT) over the life of the bridge deck. Thirdly, a suggested combination of UHPC with HSS bar deck system is being considered to meet a designated 17 psf deck weight

targeted by Florida Department of Transportation (FDOT). Alternatively, since a commercially available material Carbon Fiber Reinforced Polymer (CFRP) bar has only approximately 25% self-weight of equivalent HSS bar size, it will even lower the self weight of the structure if used to replace MMFX. However, the shortage of the CFRP bar is it has lower stiffness which brings relatively larger deflection. Hence, the UHPC with CFRP bar as reinforcement system is also being investigated in current research to verify if it would be another better option for the deck system.

## **Objective**

To summarize discussion above, in order to reduce the maintenance cost and time, simplify construction procedures, and increase the bridge life durability, two proposed systems titled “UHPC-HSS” combined deck system and “UHPC-CFRP” combined system are being investigated. The critical objective of current research is to:

- 1) Identify the appropriate dowel action contribution to shear resistance to adequately capture the strength behavior of UHPC related structure while respecting the tenets of future economic designs.
- 2) Investigate the tensile fatigue influence on UHPC component and estimate the number of cycles upon failure based on different levels of loading.
- 3) Check the serviceability issues for both “UHPC-HSS” system and “UHPC-CFRP” system which include but not limited to qualification of strength, deflections and crack widths, reinforcing bar strength attribution ratio study, shear reduction analysis, etc.

## **Plan**

- a) Since suggested “UHPC-HSS” deck system has no shear reinforcement, one of the negligible shear component, dowel action, becomes considerable in this particular situation. In order to well

estimate the full shear strength of the system, a pure dowel action performance test is designed and implemented. This test will help reveal dowel action effects of UHPC matrix which will bring a even accurate estimation of shear prediction. Several variables such as beam length, concrete covers, reinforcing bar size, etc. will be considered to reflect individual variables to dowel action peak strength.

b) An uniaxial fatigue test is designed to find the estimated limit design loading and life time fatigue prediction based on different scale of loading. The test will focus on tensile failure and the potential fatigue stress and cycle of failure was expected. Several different fatigue approaches such as mean stress approach, maximum strain approach, mean strain approach, Opensees model approaches, etc. will be analyzed and discussed.

c) Two groups of “UHPC-HSS” “T” beam with different cross section properties as well one group of “UHPC-CFRP” “T” beam were casted and tested by the cooperative UCF (University of Central Florida)-FIU (Florida International University) group to verify if all of them would qualify for the designated load capacity as well as the targeted dead load requirement. In addition, due to the fact that CFRP bars are not eligible to bend for anchorage, an unavoidable bar slip will occur which means the CFRP bar strength will never fully attributed to the strength resistance. Hence, a bar strength attribution ratio due to slippage is also expected.

## **Material Introduction**

The UHPC material used throughout all chapters in this research is the commercially available product under brand name Ductal<sup>®</sup>. The longitudinal reinforcement used in chapter 2 is the high-strength microcomposite steel rebar MMFX made from a low-carbon, chromium alloy steel. It meets the requirement of ASTM A1035 standard [6] for Grade 100 rebar with yielding stress of 100 Ksi and ultimate strength as high as 174 Ksi. The reinforcing bars used in chapter 4 are MMFX bar and CFRP bar, respectively. The CFRP bar is Aslan 200 with ultimate tensile strength of 300

Ksi and tensile modulus of elasticity of 18,000 Ksi [7].

### *UHPC*

Ultra-high performance concrete (UHPC) refers to a high-tech concrete material which was being developed over the last two to three decades. It demonstrates a series of unique and superior properties compared with normal strength concrete (NSC) or high performance concrete (HPC). The standard UHPC is made of fine sand, ground quartz, water, cement, silica fume, super-plasticizer, and 2% volume fraction of steel or organic fibers. The association Francaise de Genie Civil Interim Recommendations for Ultra-High Performance Fiber-Reinforced Concretes define the minimum compressive strength of UHPC material as 150 MPa [8]. In past several years, UHPC with even higher compressive strength up to 240 MPa has been achieved [9]. In addition, UHPC material exhibits other features such as ultimate bending strength up to 62 MPa[10], ultimate strain around 0.0045 [11], water-cement ratio as low as 0.2, high durability (96% after being subjected to two times the normal number of ASTM C666 freeze-thaw cycles [12]), long-time stability, low creep around 0.039 [13] as well as high resistance on explosion, etc. It is emphasized that thermal treatment plays a significant role on improving UHPC properties, since it eventually changes the cementitious matrix due to the fact that the reaction of silica fume and other phases may be activated, leading to a reduction of average pore size [14, 15, 16]. Other studies also concluded that both shrinkage and swelling in UHPC were reduced upon steam curing, suggesting nano-to micro-structural refinement within the material [17].

In early publications, UHPC is also called reactive powder concrete (RPC) or ultra-high strength concrete (UHSC). Some mechanical investigations and comparison work with conventional concrete have also been done by previous researchers [18, 19]. A detailed characteristic comparison between NSC, HPC and UHPC was summarized in Table 1.2.

Table 1.2: Comparison of Characteristics of Different Types of Concrete

	NSC	HPC	UHPC
Compressive Strength (MPa)	20-40	40-96	170-240
Water cement ratio	0.40-0.70	0.24-0.35	0.14-0.27
Tension strength (MPa) (Cylinder)	2.5-2.8	–	6.8-24
Diameter of Max aggregate (mm)	19-25	9.5-13	0.4-0.6
Porosity	20-25%	10-15%	2-6%
Fracture energy (kN-m/m)	0.1-15	–	10-40
Modulus (GPa)	14-41	31-55	55-62
Ultimate bending moment (MPa)	–	–	20-62
Permeability (mm) (24h/40c)	30	0	0
Absorbent (kg/mm) (225h)	20	24	35
Cl- diffusion coefficient	10	49	20
Freeze- thaw(300 cycles)	10%	90%	100%
Corrosion	1	0.08	0.01
Poison Ratio	0.11-0.21	–	0.19-0.24
Creep, Cu	2.35	1.6-1.9	0.2-0.8
Shrinkage	–	400-800 after treatment	<10 after treatment
Air volume	4-8%	2-4%	0

Compared with NSC or HPC, UHPC has no coarse aggregate. The typical main component is fine with size generally between 150 and 600  $\mu\text{m}$ . It is dimensionally the largest granular material in UHPC. The next largest particle is cement with an average diameter of approximately 15  $\mu\text{m}$ . Of similar, size of the ground quartz is averagely 10  $\mu\text{m}$ . The smallest particle, the silica fume, has a diameter that is small enough to fill the interstitial voids between the cement and the crushed quartz particles. The largest constituent in the mix is steel fibers, with a diameter of 0.2 mm and a length of 10-15 mm. They were included in the mix at a proportion of 2% by volume. The detailed percentage for individual components [20] are summarized in Table 1.3.

The mechanical properties of reinforced UHPC material can be close to steel. Meanwhile, UHPC also demonstrates outstanding resistant to wear and explosion. Based on these unique properties, UHPC is used for design of long-span bridges, ultra-thin-walled structures, and some anti-

Table 1.3: Basic Components of UHPC

	Amount(kg/m <sup>3</sup> )	Percentage in weight
Portland cement (type V)	700-1010	27-38
Silica fume	230-320	8.5-9.5
Quartz sand	0-230	0-8.0
Fine sand	760-1050	39-41
Organic or steel fiber (approx. 0.2*12.7mm)	150-190	5.5-8.0
Super plasticizer	15-32	0.5-1.0
Water (or ice)	155-210	5.5-8.0

explosion structures such as military projects and bank vaults. However, UHPC in the past two decades only had limited applications worldwide due to its high initial cost, inconvenient on-site casting, and uncompleted design codes. Over the last several years, the research and applications have been apparently accelerated and some field-casts began to take place. For example, the Federal Highway Administration (FHWA) has investigated UHPC Type II AASHTO girders [21, 22] and is studying a unique bulb-double-tee girder [23]. Virginia used UHPC in one span of the 10-span Cat Point Creek Bridge in Richland County [24]. The deck-lever connections on-site cast has been implemented in New York in 2009 recorded in Fig. 1.1a. Some famous applications include Pedestrian Bridge in Sherbrooke (Canada 1997), The Seonyu Footbridge in Seoul (Korea 2002), Sakata Mirai Footbridge in Sakata (Japan 2002), and The Wapello County Mars Hill Bridge in Wapello, Iowa (U.S 2006) as saved in Fig. 1.1b) etc. Refer to APPENDIX A to F located by the end of current dissertation for more UHPC application samples worldwide. The general components and properties of The First Express Way Bridge in France is listed in Table 1.4 .

#### *HSS bar and MMFX*

High Strength Steel (HSS) reinforcing bar is a new material commercially available with yield strength up to 550 MPa and tensile strength up to 590 MPa with sample photo shown in Fig. 1.2a.



Table 1.4: Components and Property of the 1st Express Way UHPC Bridge in France

Material Components	Density (kg/m <sup>3</sup> )	Property Description	Property Data
Portland cement	1114	Slump test	630-640 mm
Silica fume	169	Compressive strength @28 days	175Mpa
0-6mm aggregate	1072	Tension strength @28 days	8Mpa
Fiber: 20mm(L)*0.3mm(d)	234	Post crack tension strength @28 days	9.1Mpa
Super plasticizer	40	Modulus	64Gpa
Water	209	Proportion	2800kg/m <sup>3</sup>
Water cement ratio	0.19	-	-



(a) Longitudinal connections cast between deck-bulb-tee girders ([25])



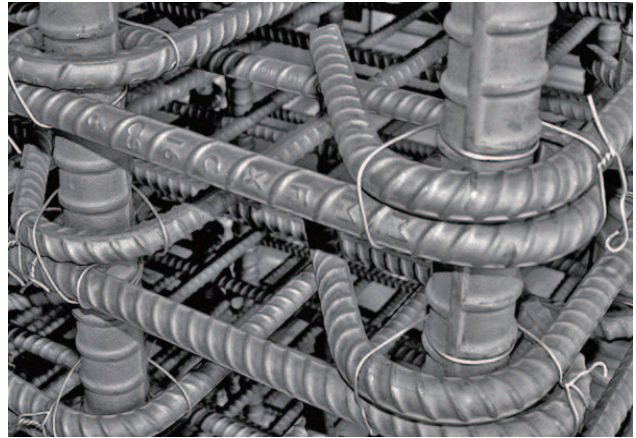
(b) The first UHPC bridge in U.S.: Wapello County Bridge ([25])

Figure 1.1: UHPC on-site cast and Wapello bridge application

It is also called structural steel bar since it's mainly used for structural applications. The typical represent of HSS, commercially known as Micro-composite Multi-Structural Formable (MMFX) steel as shown in Fig. 1.2b, is a promising material which is estimated for service life use more than 75 years. MMFX has been extensively used in automotive component structure where good durability is required. In addition, MMFX bar is appropriate reinforcing material for concrete used in industrial, transportation, utilities and waterways. The application of MMFX bar on bridge engineering accelerated in the past few decades due to the following superior advantages:



(a) Commercial HSS(Photo: Qian Fang Steel Resources Co., Ltd)



(b) MMFX sample(Photo: www.mmfx.com)

Figure 1.2: Commercially available HSS sample and MMFX sample

1. MMFX bar offers twice the strength of conventional steel (e.g. 120 Ksi versus 60 Ksi) which means a huge save of steel when equivalent strength required. It is estimated that structure using MMFX bar reduces the amount of bar needed for project by 20%-50%. Fig. 1.3 shows structure with the same strength provided by conventional steel (left side) and MMFX steel (right side).

2. A less material leads to less labor, the estimated lab costs can be lowered by up to 60%. On the other side, a less steel also leads to shorter construction times and faster project completions.

3. MMFX offers better constructability since the higher strength usually provides more flexibility and efficiency in design.

MMFX is produced by using microalloying elements such as Mn, Si, Mo, V, Cr, etc Table 1.5 [26]. Due to the low-carbon and low-alloy content, MMFX usually has sufficiently good formability at the strength levels and good weldability [27] as well as high corrosion resistant [28]. It is verified that bridge decks reinforced with 33% less MMFX steel developed the same ultimate load carrying

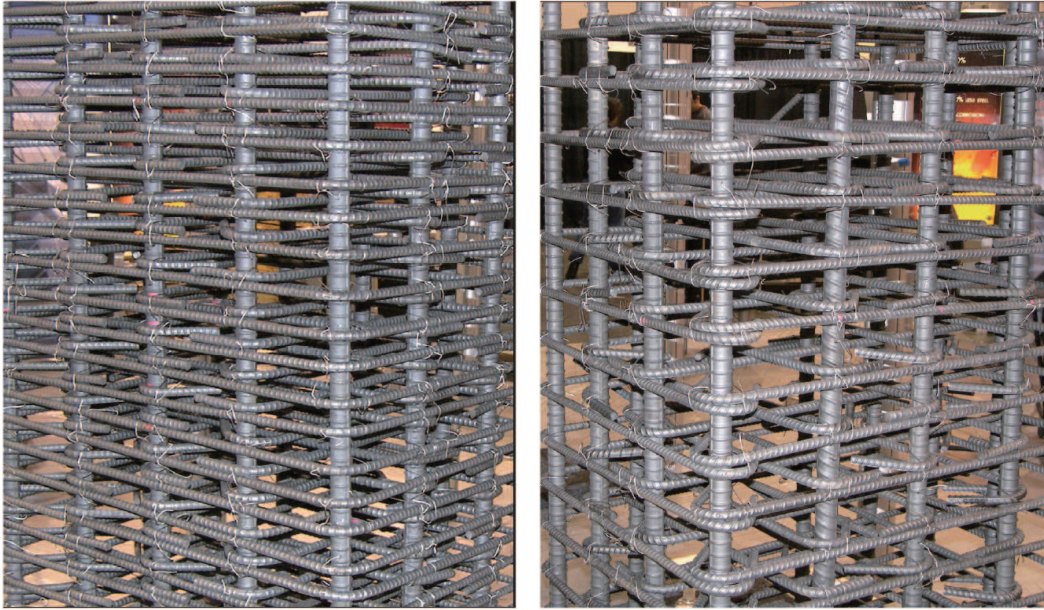


Figure 1.3: Structures of equivalent strength with conventional steel and MMFX

capacity and deflection at service load as those reinforced with Grade 60 steel [29].

Table 1.5: Typical MMFX Chemical Composition

No.	Heat	C	Mn	Si	S	P	Cu	Cr	Ni	Mo	V	Nb
1	810737	0.06	0.46	0.23	0.011	0.01	0.1	9.13	0.08	0.02	0.018	0.007
2	710778	0.06	0.46	0.25	0.012	0.01	0.07	9.17	0.07	0.01	0.18	0.007
3	809465	0.07	0.011	0.01	0.013	0.01	0.13	9.61	0.1	0.02	0.027	0.006
4	810736	0.08	0.43	0.22	0.007	0.01	0.1	9.4	0.08	0.02	0.023	0.007
5	710789	0.06	0.43	0.29	0.008	0.01	0.1	9.28	0.08	0.02	0.018	0.007

### *FRP Bar*

Fiber Reinforced Polymer (FRP) bar, a structural reinforcing bar made of filaments or fibers held in a polymeric resin matrix binder, has been resulted in a rapid increase in usage in the field of polymers and implementation of authoritative design guidelines in the past 15 years. It can be

made from various types of fibers such as glass (GFRP), carbon (CFRP) as well as aramid (AFRP). FRP rebars have been proposed for uses in lieu of steel reinforcement or steel prestressing tendons in nonprestressed or prestressed concrete structure (ACI 440R 2006).

The advantage of using FRP bars basically includes high tensile strength which makes the bars suitable for use as structural reinforcement, light self-weight which leads the entire structure more convenient for transportation and installation, zero conductive, zero corrosion and excellent fatigue resistance which delete the concern on long term stiffness decrease. In addition, the more design guidelines have been recently accelerated for preparation for using FRP bars in concrete structures for bridges and buildings (ACI 440H 2000; CSA 2000; ISIS-Canada 2000).

## CHAPTER 2: DOWEL ACTION

### Introduction

#### *Chapter Concept Introduction*

Dowel, according to the definition, is a solid cylindrical rod usually made of wood, plastic or metal with sample shown in Fig. 2.2a. The dowel component is widely applied in structural engineering. As illustrated in Fig. 2.1 for the reinforced beam, the rebar represents dowel which prevents crack along the vertical direction and the load acting on the dowel bar is defined as dowel force.

Dowel action performance with normal strength concrete (NSC) has been extensively studied over the years. Previous research on NSC dowel action specimens revealed that the shear capacity contribution of dowel action is influenced by four design parameters: compressive strength of concrete, yielding strength of steel, inclination angle of transverse reinforcement, and size of dowel rebar [30, 31]. For beams without shear reinforcement, Kim [32] stated that the dowel action contribution is largely dependent on the flexural rigidity of the reinforcing rebar and the strength

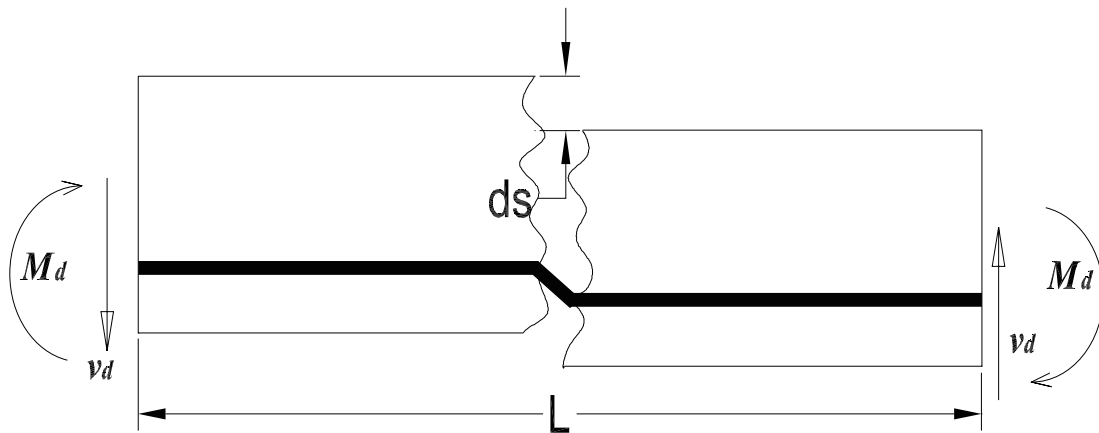
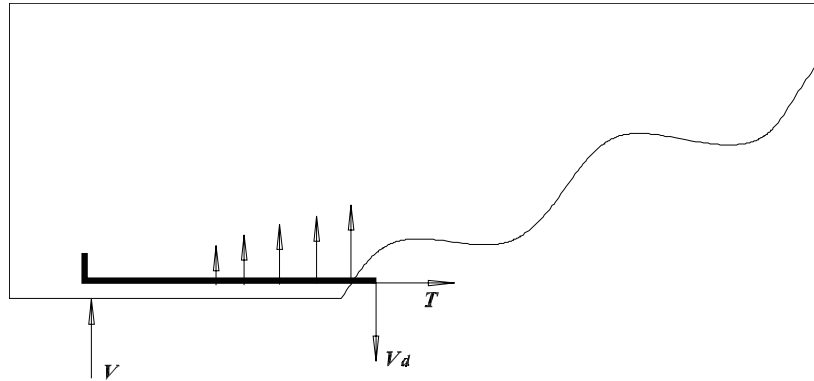


Figure 2.1: Dowel action mechanism along the cracked reinforced concrete member



(a) Dowel Samples



(b) Dowel force distribution along longitudinal direction

Figure 2.2: Dowel sample and dowel force distribution along longitudinal direction

of surrounding concrete. Both the strength of concrete and size of the cover will affect the strength of surrounding concrete. Ince [33] concluded that the contribution of the dowel action to the total shear capacity of a cracked reinforced concrete specimen increases with the value of  $\rho f_y$ , in which  $\rho$  is the reinforcement ratio and  $f_y$  is the yield stress of the longitudinal reinforcement. Soroushian [34] concluded that the bearing strength of concrete increased with increasing concrete strength and concrete cover normal to the direction of bearing action. It also increased with the decrease of bar diameter. The concrete bearing stiffness under dowel bars increased with increasing concrete strength and bar spacing, and with decreasing bar diameter. Moreover, it is emphasized that the shear capacity can be also affected by specimen size and maximum aggregate size.

### *Shear Transfer Mechanisms*

Generally, the shear resistance upon crack of concrete structures under bending test can be divided into three components which are aggregates interlock, un-cracked concrete compression zone and dowel action of longitudinal reinforcement. An approximate percentage contribution from

each component was summarized in Table 2.1. For beam constructed with NSC, the dowel action impact was neglected in most of the cases since vertical reinforcement always considered upon structure design. Hence, the shear is mainly transferred to two parts. One is the concrete portion in compression zone and the other is the effects of aggregate interlocking. However, for beams made of UHPC, the situation is different due to the absence of vertical reinforcement. The shear can be transferred to all three main parts as shown in Fig. 2.3: concrete in compression, fiber reaction contribution and dowel action. The failure model for the conventional three-point bending test changed from regular flexural failure to shear failure. Since UHPC has considerable tensile strength, very high post-crack strength and good bond strength with the longitudinal reinforcement, the flexural cracks hence can be fully controlled under limited width. Under this circumstance, the dowel action contribution is important, because the dowel force can be fully activated due to the localized deformation at the shear cracks. Basically, the total shear resistance can be expressed as follows in Eq. (2.1), in which the dowel action contribution towards the total loading capacity is considered explicitly. The estimation of peak dowel force are essentials for a better estimation of the shear strength in flexural reinforced UHPC beams without shear reinforcement.

Table 2.1: Shear transfer mechanisms (NSC)

Description		Contribution from literature review (Based on NSC)
$V_c$	Un-cracked concrete compression zone	20-40%
$V_d$	Dowel action of longitudinal reinforcement	15-25%
$V_a$	Vertical aggregates interlock	33-50%

$$V = V_c + V_d + V_a \quad (2.1)$$

As summarized from the literature review, it is obvious that almost all previous work done on dowel performance investigation was based on NSC or fiber reinforced concrete. The dowel investigation

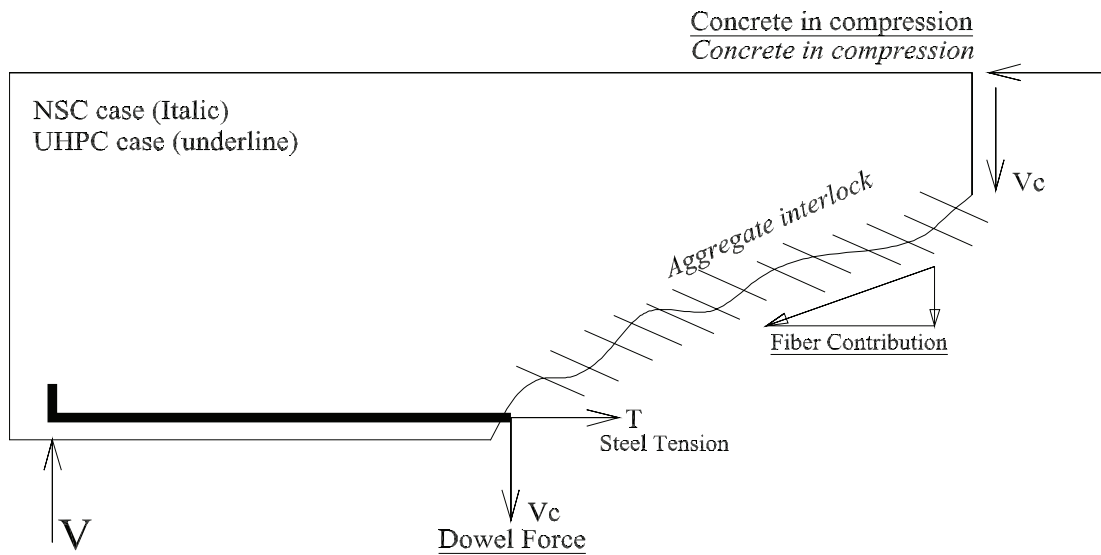


Figure 2.3: Mechanism of shear transfer

on structures containing UHPC was not investigated previously. To better understand dowel force contribution to the shear resistance, a pure “dowel action” test with specimens made of UHPC was designed and carried out at the University of Central Florida. The steel bar represents a dowel embedded into the UHPC specimen as shown in Fig. 2.2b. Several parameters such as dowel bar size, concrete compressive strength, specimen longitudinal length, and concrete boundary widths will be considered as the investigation variables.

#### *Analytical Methods Overview*

A simplified model from Friberg [35] is widely used to predict elastic dowel action response. The model treated the rebar as a semi-infinite beam on elastic foundation under a concentrated dowel load. The foundation properties were calculated based on concrete properties. This elastic model can calculate the elastic stiffness and predict the peak elastic dowel response. The nonlinear dowel force and displacement relation is usually assumed to be polynomial [36] or exponential



[37]. By knowing the peak dowel force, which depends on the various parameters mentioned previously, the complete load versus displacement relation can be obtained. Several curve fitting equations were proposed to estimate the ultimate dowel load. The equation proposed by Helen [38] includes the compressive strength of concrete and the yielding stress of the dowel rebar, while other equations [39, 36] use the tensile strength of the concrete explicitly. The peak dowel action force against concrete cover can be estimated using the following equation proposed by Soroushian [36] as shown in Eq. (2.2). The maximum dowel action force governed by the yielding strength of rebar  $f_y$  is also presented in Eq. (2.2) [38]; however, it appears that this restraint is not critical when the concrete cover is relatively small and failure occurs due to concrete cracking domination. Because all existing equations were curve fitted based on the test results of normal strength concrete specimens. hence, the expansion of these equations to UHPC beams needs further verification.

$$V_{du} = c f_t b_{eff} \frac{\pi}{2\beta} \leq 1.27 d_b^2 \sqrt{f'_c f_y} \quad (2.2)$$

#### *Finite Element Modeling of Dowel Action*

The one-dimensional finite element analysis using beam elements usually does not count for shear deformation, therefore, it can not be used to explore the effect of dowel action. A two-dimensional plane stress model with smeared four node planar elements was used by He [40]. In order to avoid the detailed modeling of contact between rebar and concrete, this method smeared the dowel action effect into all elements by adding additional shear modulus term after concrete cracking, which follows the similar approach dealing with aggregate interlocking effect. This method can be used to predict the flexural response considering the dowel action effect; however, the corresponding shear modulus due to dowel action needs calibration from experimental results. Swatie et al. [41] performed three-dimensional dowel action analysis on the dowel bar between two adjacent traffic

panels loaded in pure shear. Linear elastic spring elements were used to reflect the dowel action effect between bar and concrete while contact elements were used to take care of the possible compressive and interfacial stresses between the bar and surrounding concrete. The fact that this type of model involves detailed modeling of the rebar and surrounding concrete, while interested in global responses, such as deflection of the beam and/or the strain of rebars, cause difficulties in modeling and post-processing, therefore, can not be used for design purpose. Furthermore, the calibrated dowel action parameters using this approach might be sensitive to the stress state of the concrete that surrounds the rebar, which is different under pure shear condition than that under flexural bending condition.

The contribution of dowel action on the shear strength is usually difficult to measure during the experiment because it always combines with other shear resistance mechanisms. For the case of fiber reinforced concrete (FRC), the fibers bridging the diagonal cracks also play an important role on the shear strength and the ductility, which is also the case for UHPC. Several test setups aimed at obtaining the dowel action strength were summarized by Soroushian [36], and a double L-shaped specimen was used to investigate the dowel action against the concrete cover. Bush [42] used single shear block specimens to evaluate the dowel action contribution, and the deflected shape of the dowel rebar was measured using multiple LVDTs. However, the real in-situ condition of longitudinal rebar embedded in the bending beam with diagonal shear cracks is not represented in the previous attempts.

#### *Dowel Action Contribution to Shear Resistance of UHPC Beams*

A series of T-shaped deck strips made of UHPC and high strength steel rebars were tested in a simply-supported configuration in previous experimental studies [43]. The dimensions, rebar placement, and the loading configuration are shown in Fig. 2.4. Most of the beam specimens failed

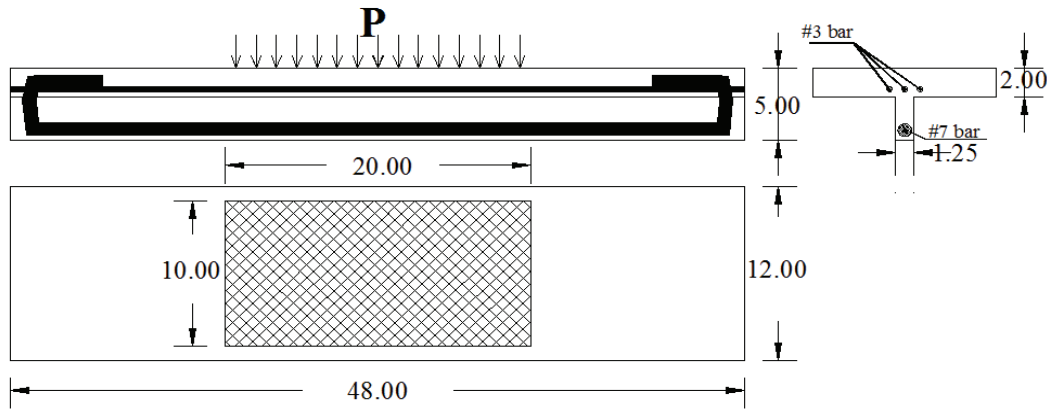


Figure 2.4: Experimental specimen geometry and loading setup

in shear and it was observed that the dowel action effect is an important component of the total shear resistance according to the deformation shapes of the specimens.

To investigate the percentage of the dowel action contribution, a two-dimensional finite element model was built in OpenSees (<http://opensees.berkeley.edu/>). The UHPC was modeled using a plane stress low-tension material model that enables crack formation in the direction of the peak principal strain. The post-cracking tension hardening and softening behaviors were included in the model. The high strength steel was modeled based on experimental uniaxial stress and strain relationships. Discrete two-node beam elements were used to simulate the rebar, and one-dimensional interface elements were created to link the rebar to surrounding UHPC elements (both top and bottom layers). The interface elements have independent bilinear force-deformation relationships in each of the normal and shear (to the rebar) directions.

The interface properties were calibrated based on the experimental results as shown in Fig. 2.5. The case without rebar anchorage (no hook case) was used to calibrate the element properties along the span, whereas the case with end anchorage (hook case) was used to calibrate the interface elements within the anchorage zone of the beam. The analytical model includes the effect of dowel

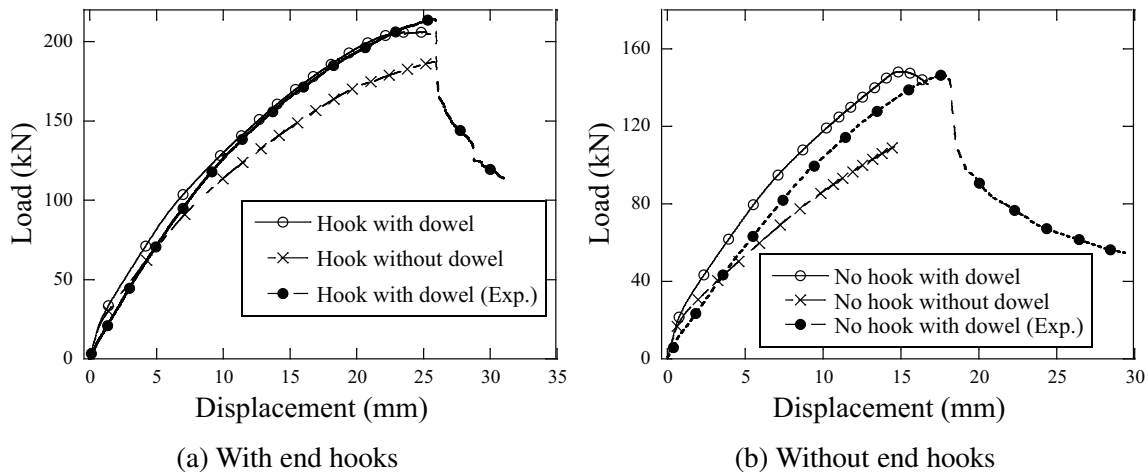


Figure 2.5: Load vs displacement curves for beam with and without dowel action

action because the rebar bearing on the cover is captured through the interface elements and the tension behavior of the concrete cover material. A permutation of the model was then created that uses a tension-free interface that can only transfer compressive stress in the normal direction with same interfacial shear property as the first model. This second model represents the case of beam without dowel action effects. The load-displacement curves from the two models are shown in Fig. 2.5 together with the experimental measurements. It can be concluded that the contribution of dowel action is approximately 10% of the shear strength for this type of specimen.

## Experimental Studies

### *Specimens Summary*

A total number of 20 cubes from the first two mixing batches and 8 cylinders from the last batch were tested to obtain the compressive strength of UHPC at an average age of 55 days. The cubes were sized at approximately 1 in. with samples shown in Fig. 2.6a and the cylinder was 5 in. by

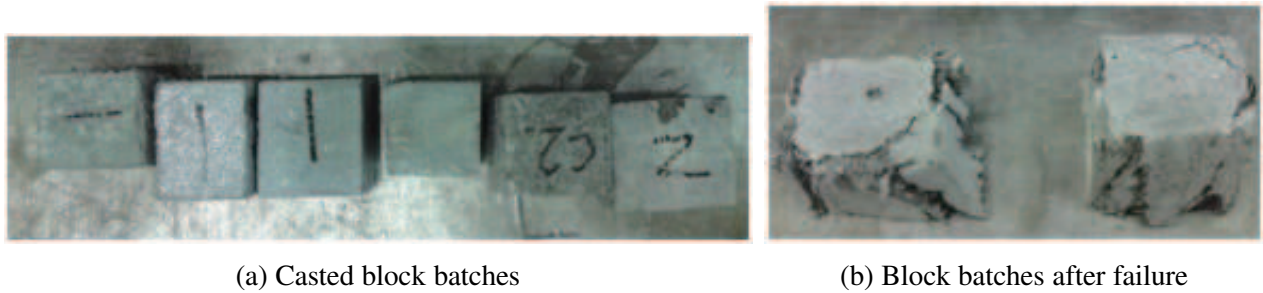


Figure 2.6: Block samples before and after failure

Table 2.2: Compression strength of specimen

Batch	Age upon test	Test Model	Avg. $f'_c$ (Ksi)	Max. $f'_c$	Proposed $f'_c$
1	55 days	Cubic	19.3	24.1	24.1
2	55 days	Cubic	17.8	22.3	22.3
3	55 days	Cylinder	24.9	26.0	24.9
Average					23.8

diameter and 10 in. by length. The average and maximum compressive strengths upon failure Fig. 2.6b from each batch were summarized in Table 2.2. Due to the fact that none of the cubes were surface ground while the cylinders were all well ground on both sides, an average of 23.8 ksi compressive strength was adopted from the test results and was used for the following calculations.

### *Specimen Design*

The dowel action specimen is designed as shown in Fig. 2.7. The notched beam is simply supported and double reinforced to minimize the bending deformation of the upper portion and to avoid undesired flexural cracks developed at the notched area. The bottom longitudinal reinforcement is the rebar of interest and it was designed so that its middle portion was completely exposed in the notched area. The dowel force was then applied at the middle portion of the bottom rebar using

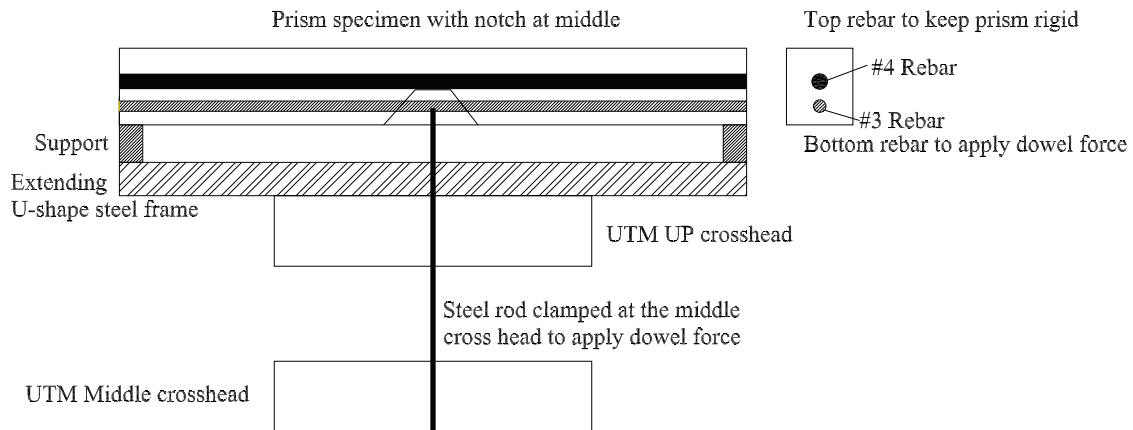


Figure 2.7: Detailed specimen test setup

a steel hook and clamp. Plastic tubes were used to debond the rebar embedded in UHPC on both sides of the notches to reduce the interface bond. Therefore, the applied force was transferred to both sides purely by dowel action against the UHPC cover. Five groups of notched UHPC prisms were constructed and a sample of group 1 (base group) real specimen with dimensions illustrated was shown in Fig. 2.8. The notch is 2 in wide at rebar locations for all specimens and the entire bottom bar was well covered with appropriate size of plastic tube except the portion exposed in the notch. Variations of the specimens among different groups, including length, depth, side cover and bottom cover size, as well as rebar size of the specimens, are listed in Table 2.3.

Additionally, another 3 specimens with parameters the same as the base group but without plastic tube covered on the bar were also constructed. They are used to check the concrete and bar bonding capacity.

The dowel bar deformation was monitored using six linear potential meters attached to the back side surface of the specimens while the front side surface was ground and painted for crack observation purposes. The tensile load was applied by a universal testing machine (UTM) under displacement control at 0.01 in per minute. The loading rate was doubled after reaching 0.1 in

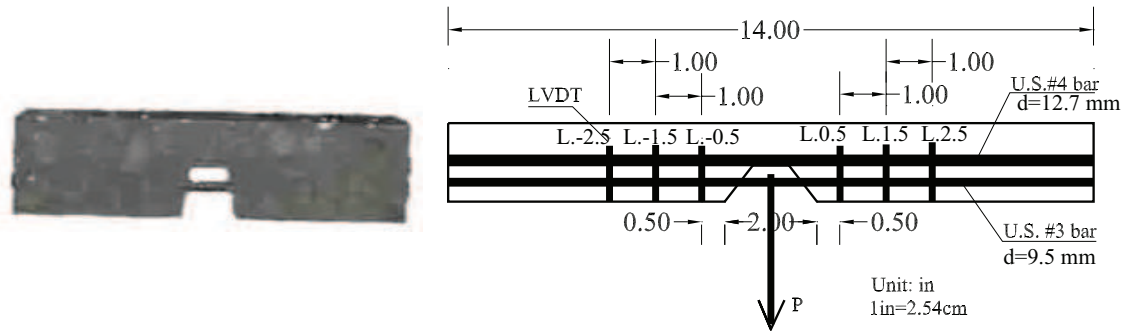


Figure 2.8: Specimen design details and dimension for base group specimen

Table 2.3: Designed specimen with comparison groups

Specimen group ID	Length $L$ (in)	Height $H$ (in)	Width $B$ (in)	Bond length $L_b$ (in)	Bottom cover (in)	Side cover (in)	Steel bar size ( $d_b$ ) (in)
1	14	4.25	1.5	12	1	0.55	#3 (0.375)
2	<b>18</b>	4.25	1.5	16	1	0.55	#3 (0.375)
3	14	4.00	1.5	12	<b>0.75</b>	0.55	#3 (0.375)
4	14	4.25	1.14	12	1	<b>0.40</b>	#3 (0.375)
5	14	4.50	1.73	12	1	0.55	<b>#4 (0.5)</b>

deformation. The test was terminated if the displacement gauge reached the limit or the cracks widened such that it prevents the continuation of loading, whichever occurred first.

### Results

The progression of failure of a typical specimen was demonstrated in Fig. 2.9. The dowel load increased rapidly initially until the first crack appeared at one or both sides of the notch. After

Table 2.4: Peak dowel load from different groups

	Average load (kip)	Load standard deviation (kip)
Group 1 (base)	2.88	0.23
Group 2 (longer span)	3.59	0.16
Group 3 (smaller bottom cover)	2.85	0.16
Group 4 (smaller side cover)	1.83	0.15
Group 5 (larger rebar)	4.03	0.59

Table 2.5: Peak dowel load from base group and group with bar concrete bonded

	Average load (kip)
Group 1 (base)	2.88
Additional Group (without debonding)	4.84

that, the dowel load increased slowly with lower stiffness and the cracks widened on both sides. The specimen reached its peak load shortly after the visibility of the side cracks. The average peak load for each group and standard deviation is reported in Table 2.4. In addition, the contrast of specimens without debonding to base group specimens was also reported in Table 2.5. The load versus UTM table movement for specimen group one is shown in Fig. 2.10a and the displacement distribution along the longitudinal direction of the beam with respect to different load level is shown in Fig. 2.10b for specimen 1-2. The recorded load and displacement for the additional group was plotted as shown in Fig. 2.11

## Theoretical Analysis

### *Beam on Elastic Foundation (BEF)*

The experiment setup and corresponding simplified model are shown in Fig. 2.12. The embedded rebar was treated as an elastic beam, while the support from surrounding UHPC was treated as two



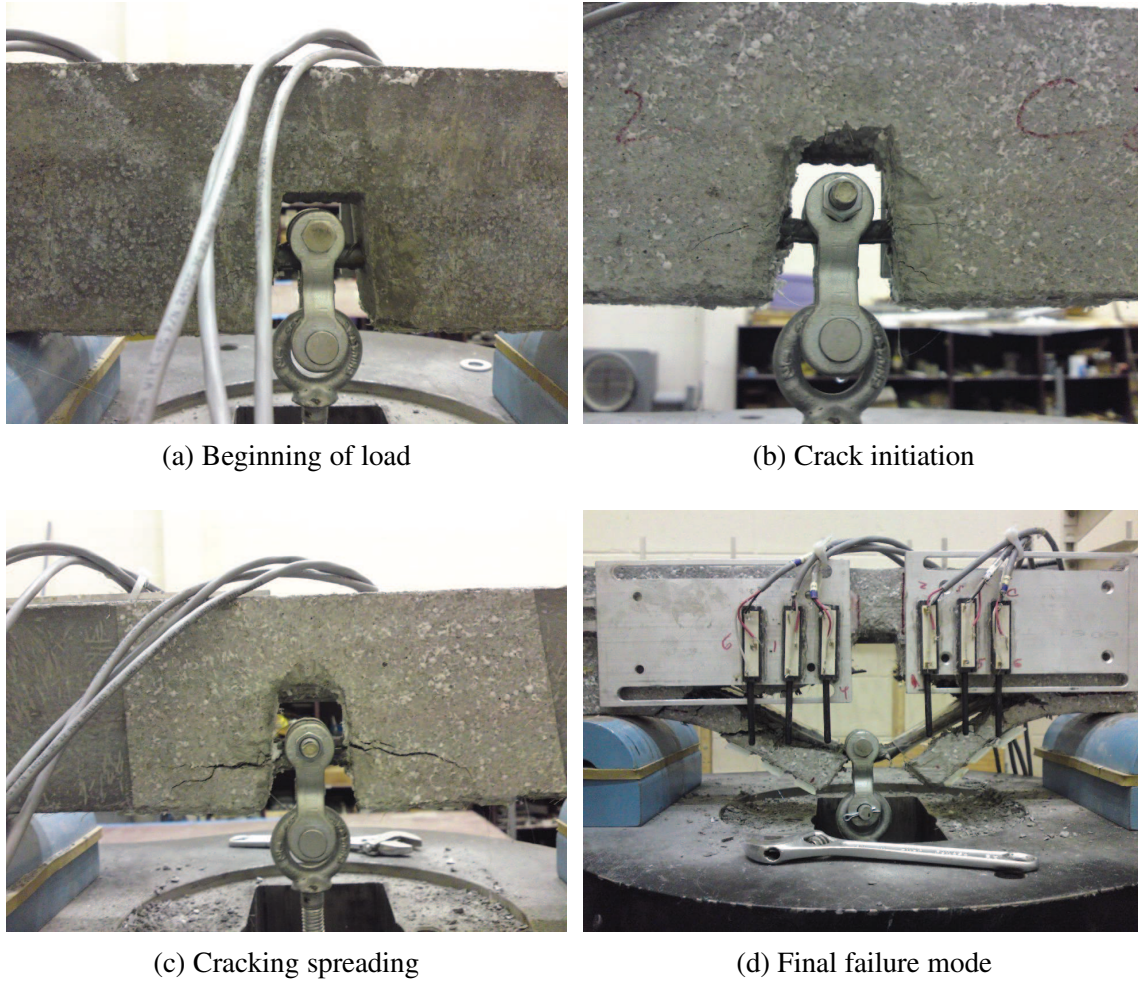


Figure 2.9: Failure mode of typical specimen

separate finite length elastic foundations. Because the model is symmetric, only the right part of the beam was considered in the analytical model. The width of the free span in the middle equals the width of the notch. The complementary solution to the BEF differential equation,  $y_1(x)$ , satisfies the displaced shape in the free span (notched region), as shown in Eq. (2.3), when  $x \in (0, d]$ . The solution,  $y_3(x)$ , for the remaining domain  $x \in (d, d + L_d]$  as shown in Eq. (2.4) is assumed from existing approximate BEF solutions for finite length beams on elastic foundations [44].

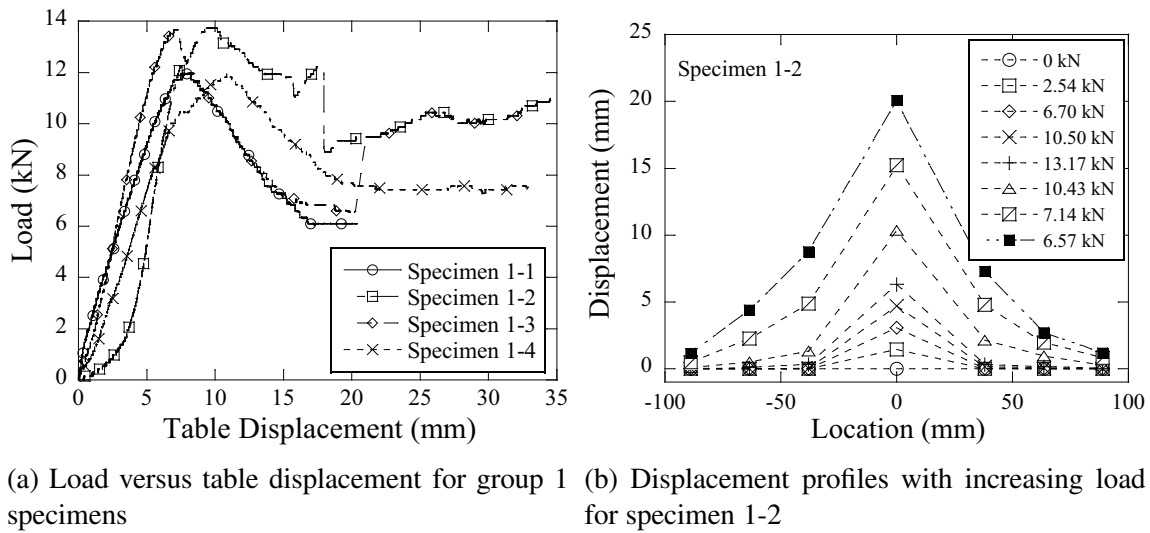


Figure 2.10: Experimental results

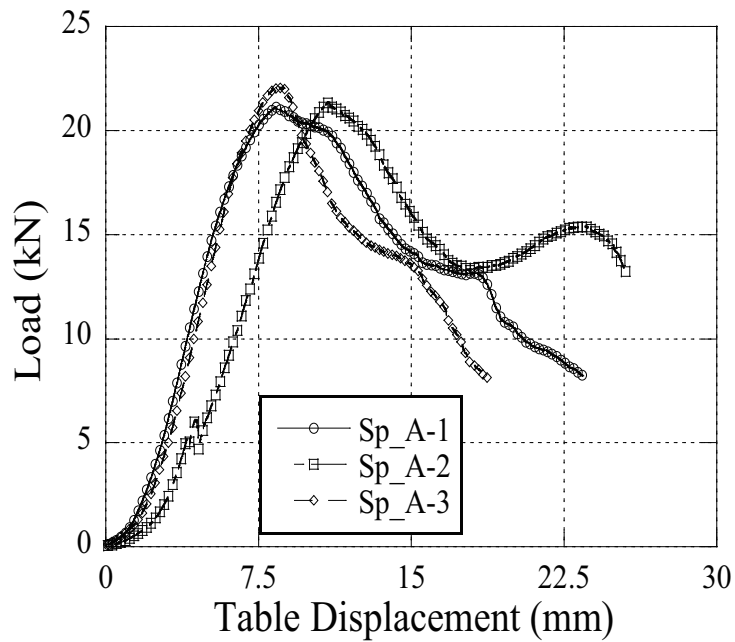


Figure 2.11: Load versus table displacement for additional group specimens

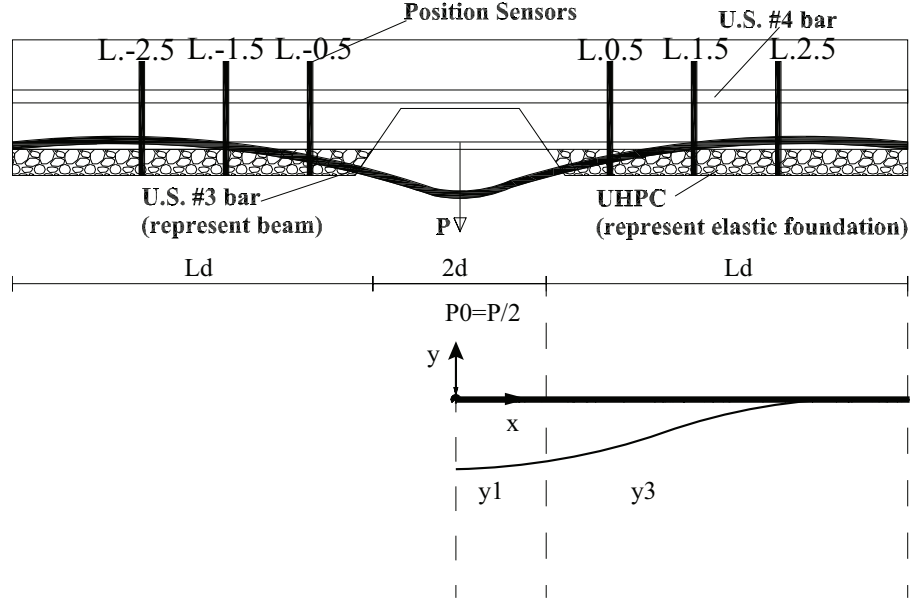


Figure 2.12: Test setup and simplified model

$$y_1(x) = \frac{1}{6}c_1x^3 + \frac{1}{2}c_2x^2 + c_3x + c_4, x \in (0, d) \quad (2.3)$$

$$y_3(x) = \frac{P_0\beta}{4k} [4e^{-\gamma} \cos \gamma - (2 - 2\beta d)e^{-\gamma}(\cos \gamma - \sin \gamma)], x \in (d, d + L_d) \quad (2.4)$$

where  $\beta = \sqrt[4]{\frac{k}{4EI}}$  and  $\gamma = \beta(x - d)$ . The boundary conditions can be expressed as follows:

$$\left\{ \begin{array}{l} y_1(x = d) = y_3(x = d) \\ \frac{dy_1}{dx}(x = d) = \frac{dy_3}{dx}(x = d) \\ \frac{dy_1}{dx}(x = 0) = 0 \\ -EI \frac{d^3 y_1}{dx^3}(x = 0) + P_0 = 0 \end{array} \right. \quad (2.5)$$

By solving these equations for the four unknown constants, the final displacement expressions are:

$$y_1(x) = \frac{P_0\gamma^2}{24\beta^3 EI}(2\gamma + 3\beta d) - \frac{P_0\beta}{2k}(\gamma^2 + 2\gamma\beta d - 1 - \beta d) \quad (2.6)$$

$$y_3(x) = \frac{P_0\beta e^{-\gamma}}{2k}(\cos \gamma + \sin \gamma + \beta d(\cos \gamma - \sin \gamma)) \quad (2.7)$$

The elastic solution is valid only before the initiation of cracking. After that, the UHPC cover will lose stiffness at the crack location and the foundation modulus will no longer be uniform along the length of beam. Because at such an early loading stage, the linear displacement gauge at locations L3.5 and L2.5 did not show any significant deformations, only recorded data at location L1.5 were used for the calibrations. The expressions of foundation deformation in Eqs. (2.6) and (2.7) were used in a nonlinear regression on the data recorded between 5 to 40% of the peak load to have a close to elastic response based on the load versus displacement curves. The nonlinear regression coefficients are summarized in Table 2.6. Related parameters, such as  $EI$  are calculated based on individual specimens with respect to the rebar used and specimen dimensions.

Once the foundation modulus  $\beta$  was quantified, the peak load can be estimated using Eq. (2.2) using an appropriate tensile strength of UHPC. The tensile strength was estimated as  $f_t = 1.1$  ksi based on average results from two estimation equations shown in Eqs. (2.8) (2.9) [45]. The results are shown in Table 2.6 with an additional safety factor calculated based on the ratio of the experimental peak load, as listed in Table 2.4, to the value computed with Eq. (2.2). The magnitude of the safety factor being larger than one is understandable as the foundation stiffness of UHPC is higher than normal concrete, and the portion that participates to provide the dowel action resistance is wider.

Table 2.6: Results from the BEF analysis

ID	Group 1	Group 2	Group 3	Group 4	Group 5
Modulus ( $\beta$ )	2.36	2.02	2.07	2.30	2.31
Peak Load ( $2V_{du}, c = 0.83$ )	5.96	6.97	6.81	6.11	6.09
Safety Factor	2.15	1.59	1.41	1.29	2.12

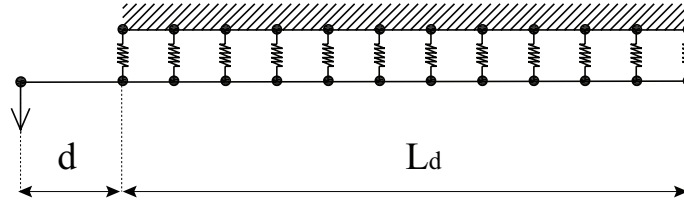


Figure 2.13: BNF finite element model

$$f_t = 0.55f_c^{0.5} \quad (2.8)$$

$$f_t = 0.049f_c \quad (2.9)$$

### *Beam on Nonlinear Foundation (BNF)*

As mentioned above, once the cover concrete cracks, the foundation modulus is no longer constant along the length of the dowel bar. The nonlinearity in the foundation modulus can be represented using standard beam on nonlinear foundation models. To better understand the appropriate nonlinear force-deformation relationship, the dowel action setup was simulated using a simple finite element model, as shown in Fig. 2.13. The rebar was modeled as a one-dimensional flexible elastic beam element. The surrounding concrete cover supporting the beam was modeled as a series of discrete nonlinear springs.

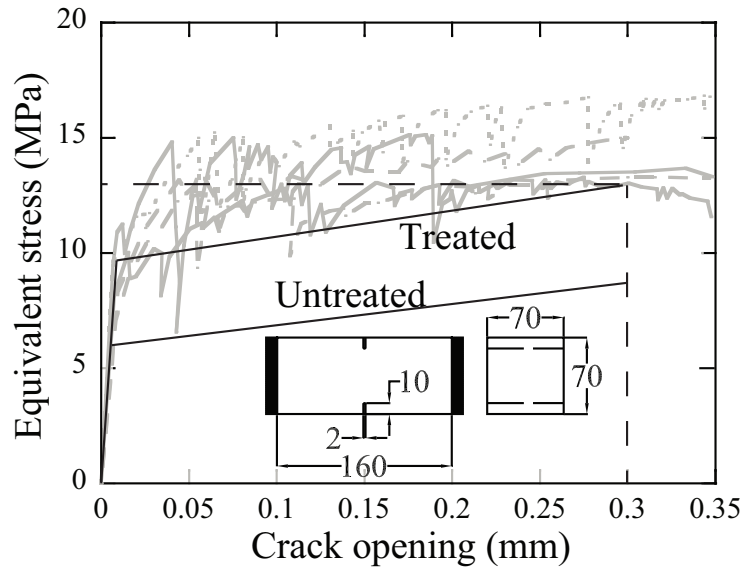


Figure 2.14: Stress and crack width relation for nonlinear spring

The stress versus crack relation utilized to calibrate the concrete springs in tension is shown in Fig. 2.13. The actual responses in the figure were obtained from previous experimental results [3]. Two bilinear relations were fitted to the experimental data as shown in Fig. 2.14, the upper representing material that was heat treated, while the lower is an assumed reduction to reflect the lack of heat treatment and its impact on the compressive strength. The material stress-crack width was then converted to the load-deformation relation for the spring, considering the width and spacing of the nonlinear spring in the model. A simulation utilizing the base group variables was performed. The load versus displacement for three measurement stations was obtained from finite element analysis, with the corresponding load values multiplied by two to consider the dowel action contribution from both sides. These curves were then compared to the experimental results (experimental specimens SP. 1 to SP. 4) as shown in Fig. 2.13. The comparison demonstrates that the spring force deformation relation used in the BNF model accurately reflects the concrete contribution during the dowel action progression from the test.

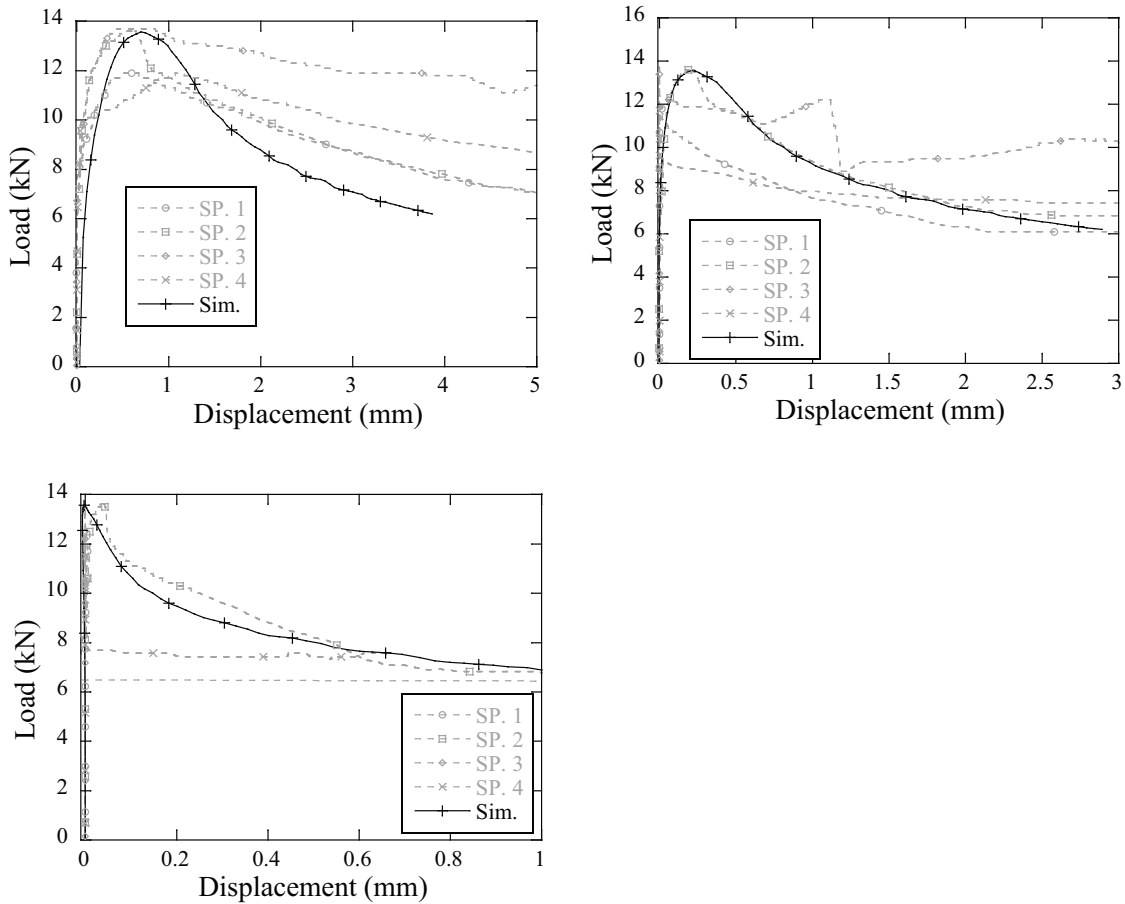


Figure 2.15: BNF finite element model results comparison to experiment results

Although finite element analysis gave reasonable results when compared to the experiment results, a simplified theoretical derivation similar to that presented for BEF is still desirable. A schematic for the BNF proposed is shown in Fig. 2.17. Conceptually, the model is the same as the BEF model in Fig. 2.12; however, to investigate the nonlinear dowel action load displacement relation including post-peak responses, an additional domain  $y_2(x)$  was added. The figure shows both the expected deformed shape of the rebar, as well as the foundation reaction.

Between the free span and elastic portion of the foundation, the foundation response is assumed to be perfectly-plastic with reaction  $f_t$ . Given the expected behavior is not perfectly-plastic from

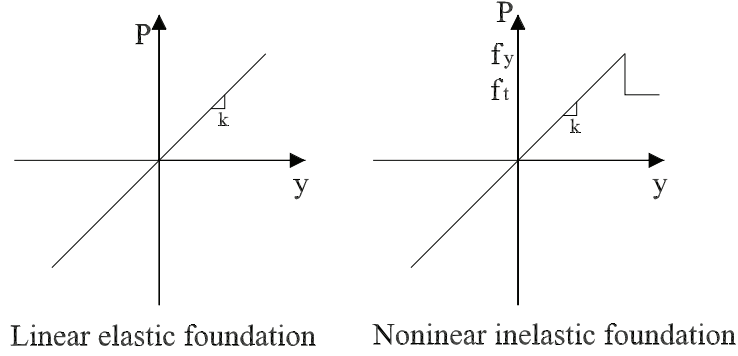


Figure 2.16: Load displacement model for linear and nonlinear foundation

Fig. 2.14, the foundation force-displacement was generalized slightly by allowing the reaction  $f_t$  to be proportional (with parameter  $\alpha$ ) to the estimated cracking reaction  $f_y$ , as shown in the two force-deformation relations of Fig. 2.17. This introduces an extra parameter related to the length over which the plastic behavior occurs,  $d_m$ .

The schematic drawing of the model is shown in Fig. 2.17. The solution for the deformation of the rebar in the three domains of the nonlinear foundation are labeled as  $y_1(x)$ ,  $y_2(x)$ , and  $y_3(x)$ . Solution of differential equations for each domain yields expressions with eight constants of integration. The complementary solution for the free span is the same as Eq. (2.3) and not repeated. The solution for  $y_2(x)$  in the domain  $x \in (d, d + d_m)$  is shown in Eq. (2.10). Finally, the approximate solution for the finite beam on elastic foundation [44] is the same as used previously, but updated to reflect the length over which the response is elastic  $x \in (d + d_m, d + d_m + L_{d0})$ , as shown in Eq. (2.11).

$$y_2(x) = -\frac{f_y x^4}{24EI} + \frac{1}{6}c_9 x^3 + \frac{1}{2}c_{10} x^2 + c_{11} x + c_{12} \quad (2.10)$$

$$y_3(x) = \frac{P_0 \beta}{4k} [4e^{-\beta x} \cos(\beta x) - (2 - \beta L_{d0})e^{-\beta x} (\cos(\beta x) - \sin(\beta x))] \quad (2.11)$$



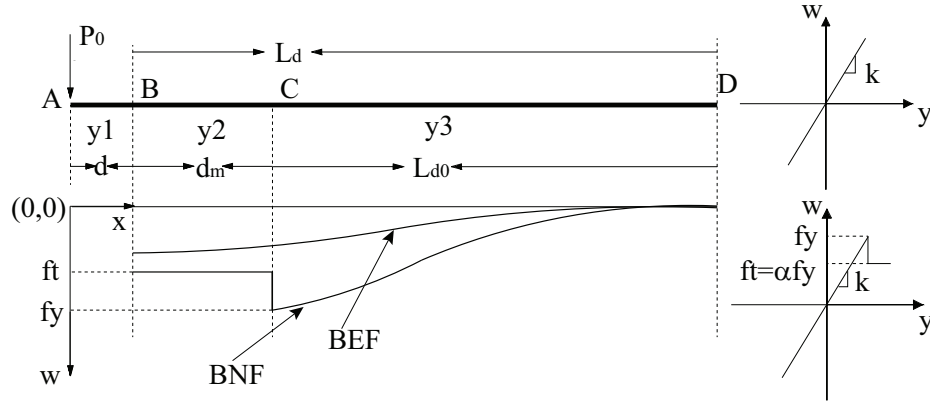


Figure 2.17: Schematic drawing of the BNF model

Parameter  $L_{d0}$  is the equivalent length of the free span for the right part. It can be calculated as  $L_{d0} = L_d - f_y d_m^2 / P_0$  based on the equivalence of moment and shear force at location C as illustrated in Fig. 2.17. Six integration constants can be solved by similar boundary conditions as the elastic solutions, and are not repeated here. Two additional constraint equations are introduced as follows:

$$\begin{cases} f_t = \frac{1}{4}(P_0 \beta (2 + \beta L_{d0})) \\ f_y = \alpha f_t (1 - \frac{d_m}{L_d}) \end{cases} \quad (2.12)$$

The first equation ensures that the force at location C equals the critical cracking force  $f_t$ , and the second equation specifies the reduction function of the yielding force  $f_y$  with respect to the spreading length of the yielding portion. Parameter  $\alpha$  is the factor taking care of the stress change at the onset of the cracking, as shown in Fig. 2.17.

By specifying the numerical values of known parameters, the force versus  $d_m$  relation can be obtained, which shows the spreading of nonlinear foundation behavior away from the notch as the load is increased. This relation is a function of parameter  $\alpha$ , which can be estimated based on the experimental results. The load versus yielding width  $d_m$  is shown in Fig. 2.18, with the

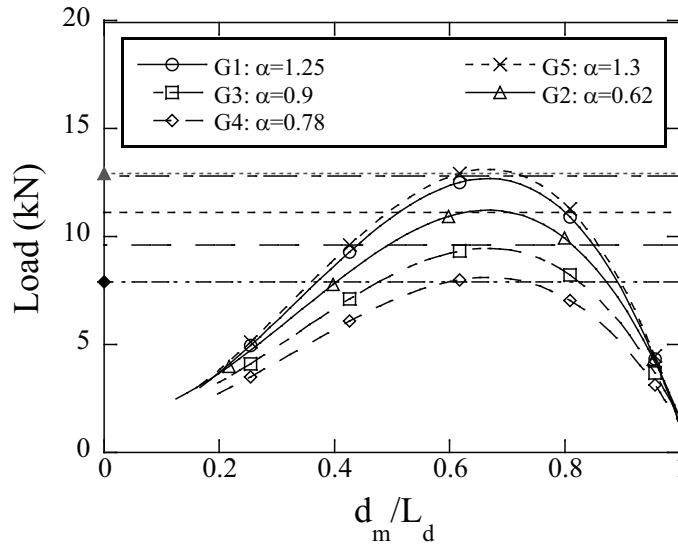


Figure 2.18: Load versus yielding range for various  $\alpha$  values

horizontal axis being normalized by  $L_d$  to allow comparison for groups with different lengths. For all  $\alpha$  values, the peak load happens around  $d_m = 4$  in., which is determined by the linear decay relation between  $f_y$  and  $d_m$ . This can be improved by verification of more experimental deflection data with different beam length.

The elastic foundation modulus  $\beta$  used in the calculation is the same for all groups and equals 1.7.

## Chapter Discussion and Conclusions

This chapter investigated the dowel action between high strength rebar and surrounding UHPC using analytical, experimental, and theoretical approaches. Experimental specimens were tested with notches to load the rebars embedded in UHPC. By using the plastic separation tubes, the test setup successfully obtained the peak dowel force without the influence of the interfacial bond. Dowel forces obtained were on the order of 2.88 kip for the base group. Therefore, the dowel action attribution percentage to shear can be computed once shear force from the tested specimen

obtained. On the other side, the tested specimens with UHPC and bar well bonded indicated a peak dowel force of 4.84 kip which is approximately 68.1% higher than that from the base group.

By using beam on elastic foundation theory, the foundation modulus for the case of rebar bearing against UHPC cover was calibrated based on the experimental displacement results. To capture the peak dowel force, the concept of elastic beam on nonlinear foundation was utilized. By assuming the decay relation between the foundation yielding length and the average post-crack tensile strength of UHPC, the peak load can be estimated based on the initial cracking strength.

Without considering the shear strength and corresponding shear failure mode, the peak load predicted from flexural responses will be higher than what was obtained from the experiment, therefore post safety threat to the structure if we only rely on flexural design. On the other hand, use shear strength predicting equation in the current design guideline sometime under estimated the shear strength of the beam system and thus lead to a uneconomic design. Therefore, a more close to reality shear predicting mechanism shall be obtain for a better design procedure. In order to achieve this goal, the components of the shear strength contribution shall be discussed in detail, and one of them, the dowel action, was investigated in this chapter. Based on Fig. 2.5, after considering the dowel action explicitly, the peak load can increase about 25 kN from the case without its consideration, which is more than 10% of the total peak load.

Usually, all factors contributing to the shear resistance of reinforced concrete beams are linearly combined to reflect the total shear resistance, such as that shown in Eq. 2.2. When considering dowel action effects, the peak force estimated from the equation is usually used. However, in order to achieve the peak dowel reaction, the shear cracks need to widen to an extent that may affect the shear resistance from the bridging fibers. In other words, a simple linear combination of the peak reaction from individual shear resistance mechanisms may overestimate the total shear resistance. This is especially true for the case of UHPC due to the higher strength and steel fiber contribution

to shear resistance. More complicated models that involve geometric compatibility should be developed to address this phenomenon fully; however, the dowel action versus displacement relation investigated in current chapter can provide a foundation for such research.

## **CHAPTER 3: UNIAXIAL FATIGUE INVESTIGATION ON UHPC STRUCTURES**

### **Introduction**

Fatigue failure is defined as the tendency of a material to fracture by means of progressive brittle cracking under repeated alternating or cyclic stresses of an intensity considerably below the normal strength. There is usually little or no warning before failure if the crack is not noticed during the cycling process. The number of cycles required to cause fatigue failure for solid material such as concrete or even metal is generally quite large, but it decreases as the stress is increased. In terms of loading, it is usually divided into two types, one is low-cycle loading while the other is high cycle loading [46]. Low-cycle loading involves the application of a few load cycles at relatively high stress levels. For instance, it represents extreme loading scenarios like earthquake or hurricane wind loading. High-cycle loading is characterized by a large number of cycles at relatively low stress levels. For example, it may represent the traffic loading on bridges or pavements as shown in Table 3.1. Fatigue life can be affected by many factors such as environment, surface finish, creep and time-dependent phenomena. The measurement of stress-life behavior, usually presented on S-N curves, was first proposed by Wohler in approximately 1860.

Concrete is a heterogeneous cementitious material that is inherently full of flaws such as pores, air voids, lenses of bleed water, aggregates (potentially), and shrinkage cracks. It has been summarized previously that the fatigue failure mechanisms in concrete can be divided into three distinct stages [47]. The 1st stage involves the weak regions within the concrete and is termed flaw initiation. The 2nd stage is featured by slow and progressive growth of the inherent flaws to a critical size known as micro-cracking. The 3rd stage is when a sufficient number of unstable cracks have formed. The cracks will then continue to enlarge and eventually cause failure at the macroscopic

Table 3.1: Fatigue load classes and applications

class	Cycle numbers	Applications
Low-cycle fatigue	$10^0$	Structures subjected to earthquakes
	$10^1$	
High-cycle fatigue	$10^2$	Airport pavements and bridges
	$10^3$	
	$10^4$	
	$10^5$	Highway and railway bridges, highway pavements
	$10^6$	
Super high-cycle fatigue	$10^7$	Mass rapid transit structures
	$10^8$	
	$10^9$	Sea structures

level. The crack propagation can be also summarized as 2 stages [48], which are called deceleration stage and acceleration stage. The crack growth in the acceleration stage (e.g.  $a > ac$ ) is governed by the change in stress intensity factor during each load cycle. It is defined quantitatively by the Paris Law [49, 50] as shown in Eq. (3.1). The left term represents the crack growth rate, where  $a$  represents the crack length and  $N$  is the number of load cycles. The right term contains material constants  $C$  and  $n$ , and  $\Delta K$  is the range of the stress intensity factor.

The deceleration stage (e.g.  $a < ac$ ) was also proposed with equation as described in Eq. (3.2) by Subramaniam et al [51]. The rate of crack growth decreases as the length of crack grows in deceleration stage while there is a steady increase in the crack growth rate right up to failure in the acceleration stage.

$$\frac{\Delta a}{\Delta N} = C_2(\Delta K_1)^{n_2} \quad (3.1)$$

$$\frac{\Delta a}{\Delta N} = C_1(a - a_0)^{n_1} \quad (3.2)$$

Former investigations of fatigue on concrete have been concerned only with the behavior of ma-

terials when subjected to either axial or flexural loads. Those which have attempted to investigate the response of the material to axial loads were focused on compressive axial loads in most of the cases. For example, Su and Yin [52, 53] concluded that the fatigue strength of concrete in biaxial compression is greater than that under uniaxial compression. Van Ornum [54] conducted compression tests on two-inch cubes of neat cement aged four weeks and the test indicated fatigue strength of approximately 55 percent of the static ultimate strength at 7000 cycles of load. The investigation of concrete behavior under uniaxial loads was not commonly investigated as the fatigue life of concrete in uniaxial compression, particularly at service stress amplitudes, is usually not a limiting factor for design or performance prediction due to the relatively low tensile strength of concrete (relative to its compression strength). Uniaxial tension fatigue tests may not have been conducted due to the fact that concrete is seldom expected to resist tension in typical reinforced concrete. Or it may be due to the assumption by researchers such as Nordby [55] that tension failure is closely related to the fatigue of concrete flexure specimens. In addition, the difficulty in devising an appropriate tension specimen and subjecting it to repeated axial tension loads may be another factor that limits the development of tensile fatigue tests. The sole investigation related to the behavior of tensile response was reported early in 1898. The test indicated a fatigue limit of approximately 50 percent of the static strength of specimens and the number of cycles of load sustained prior to failure was inversely proportional to the frequency of application.

In recent years, as fiber reinforced concrete (FRC) including UHPC rapidly developed, a series of fatigue tests were made on it. The fatigue load test performed on Ductal<sup>®</sup> showed the material properties recommended for design by the French code are on the safe side. Under flexural test, the specimens were loaded up to 90% of the first crack strength for 106 cycles, after 1 million cycles, no sign of degradations observed and no description of reversal loading was found [56]. For high performance fiber reinforced concrete (HPFRC), quasi-static flexural strength fatigue test on notched beam were performed under third point bending. It was found that fiber number across

the section is not the only factor govern the flexural fatigue behavior. The fatigue test with UHPC examined at the Leibniz University of Hannover carried out with a constant low stress lever of 5 percent of the static strength and varying upper stress levels. More than 125 specimens were tested with up to 15 million load cycles subjected to uniaxial compression fatigue and a total number of more than 165 million cycles reached. The regression lines for the average S-N curve of UHPC mixtures display scopes both above and below the Wohler-line for normal strength concrete derived by Klausen [57]. The fatigue behavior investigation on non-stirrup UHPC I-girder by Graybeal [58] indicated that under four-point test with two actuators cycling between 30 and 200 kips, the beam had yet to reach catastrophic failure even after 12 million cycles with a 170 kip shear load range. Although multiple cracks developed during the application of these cycles, there was no noticeable change in the global behavior of the girder.

Meanwhile, an increasing number of researchers have examined the fatigue characteristics of FRC in tension [59, 60, 61] due to the tensile strength of FRC relative to NSC. and introduction of nonlinear fracture mechanics widely accepted in the analysis of concrete. The fibers are more effective in enhancing the flexural fatigue behavior, but have less or even no contribution on the compressive fatigue behavior. Therefore, fiber content is the most important factor on the fatigue performance enhancement.

As discussed in last chapter, UHPC exhibits ultra high strength due to the particular material property. Therefore, it leads to a different failure mode rather than the traditional one. In addition, the service life load amplitudes and resistance under cyclic loading are of importance since the state of stress in the UHPC beams is quite different than that of regular concrete beam. Hence, the fatigue life of cyclic loading both in compression and tension are worthy of investigation. However, due to the almost infinite fatigue life of concrete in compression, the concrete fatigue behavior in tension is of interest in limiting the fatigue life. In order to find the behavior of fatigue life in tension, an uniaxial tensile fatigue test was designed and carried out in the laboratory of University of Central



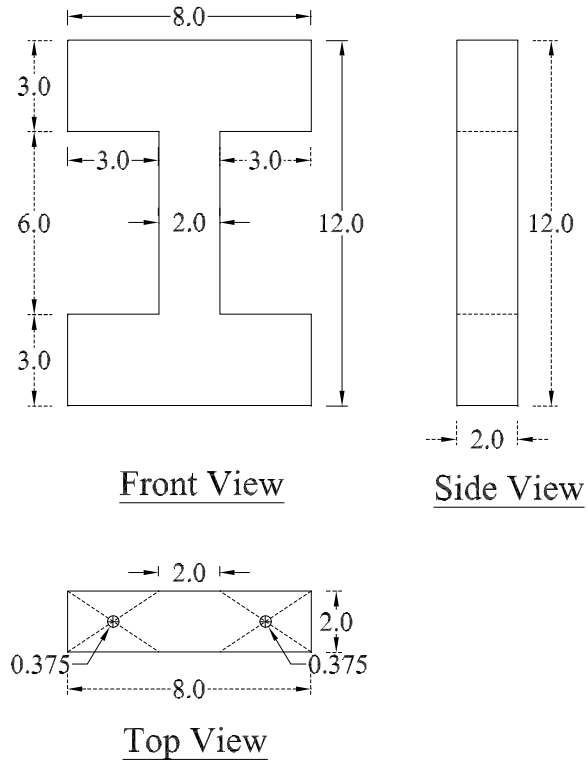


Figure 3.1: Fatigue Specimen Dimension

Florida. Direct data and phenomenon from the test as well as analytical results and discussion were presented in this chapter.

### Experimental Work

To investigate the UHPC fatigue response in uniaxial tension, an “T”-shape UHPC component as shown at Fig. 3.2 with dimensions included was designed for the test. The material used for this project is also the Ductal<sup>®</sup> as used in chapter II introduced previously.



Specimens being casted



Casted specimens

Figure 3.2: Test specimens during and after cast

Table 3.2: Specimen History Record

Number of Specimen Casted	Casting Date	Test Time	Approximate Specimen Age Upon Test (days)	Average Compression Strength $f'_c$ (ksi)
18	05/05/2011	Nov-Dec 2011	210	18

A total number of 18 “I”-shape UHPC components shown in Fig. 3.2 were cast on May-05-2011 and tested at an average age of 210 days. The concrete compression strength was determined as an average of 18 Ksi from blocks sized 1 inch by 1 inch with the same batch when the components casted. A brief summary was listed in Table 3.2

Four holes with diameter of 0.375 inch located in both top and bottom flanges were filled by PVC pipes with appropriate size during concrete casting. The designed concrete specimen was

Table 3.3: Specimen testing matrix with achieved stress ranges

Cross section (a*b)	Specimen number	Applied tension (kip)	Applied compression (kip)	Number of cycle at failure
2*2	1	2.42(40%)	15(20%)	67000
2*2	2	2.10(35%)	15(20%)	142700
2*2	3	2.00(33%)	15(20%)	2534000
2*2	5	3.25(55%)	15(20%)	13800
2*2	6	3.00(50%)	15(20%)	5000
2*2	7	2.30(38%)	15(20%)	10000
2*2	8	2.80(47%)	15(20%)	53000

connected using high strength bolts with the bottom flange bolted to a W24x146 steel section. The large “W” section was fixed to the strong floor. The upper flange of the specimen was bolted to MTS steel box as illustrated in Fig. 3.3. The loading protocol originally selected was intended to produce a uniaxial loading with constant amplitude cycles. The amplitude in compression was constant for all specimens at 3.75 ksi, which represents an approximately 20% of the assumed maximum compressive strength of the material. The amplitude in tension was ranged from 0.5 ksi to an assumed critical stress of 0.8125 ksi based on different specimens. All cyclic tests were performed at a rate of 2 Hz.

Four foil-backed resistance gauges were mounted on each of the four surfaces of the specimen webs to record the strain response. The testing matrix with actual achieved stress levels is shown in Table 3.3. Among the casted 18 specimens, 2 were used to cut for blocks for general compression test. Unfortunately, due to the difficulty on test setup accuracy, only 7 specimens were recorded as valid while the other 9 failed either due to cracks formed outside the UHPC web or used for monotonic tension or compression test. A sample photo of failed specimen can be seen in Fig. 3.4

The data acquisition system was set up to record 10 complete cycles every 100 cycles. Individual specimen test time varied from few hours to up to 45 hours. The strain history response,

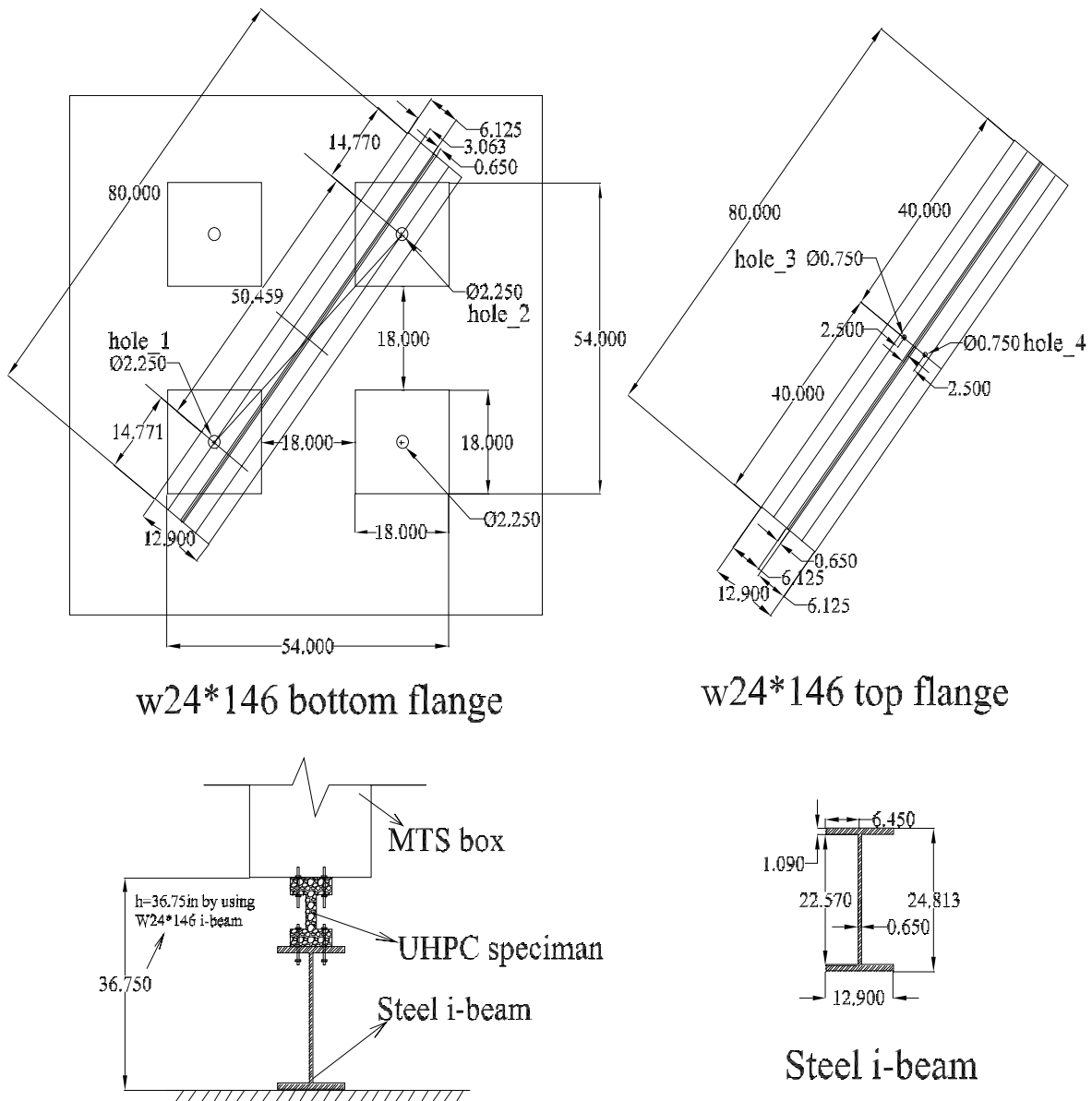


Figure 3.3: Test Setup

for example, with specimen 3 at 10,000th cycle, 100,000th cycle and 500,000th cycle as well as 1,000,000th cycle are shown in Fig. 3.5. It is obviously seen from the graphic that as the number of cycles progressed, the tension strain keeps on increasing gradually. However, it was also immediately obvious during the tests that eccentricities in the test setup and flexibilities in the specimens



Strain Gage Failure Overview



Strain Gage failure Closeview

Figure 3.4: Failure of strain gage due to concrete surface crack

and attachments prevented the response from being uniaxial with constant amplitude. During tests on all specimens, the strain gage responses on the four faces indicated non-symmetric response of the cross section, with the imposed axis of bending in the specimen changing orientation during cycling as well as during the positive vs negative excursions during each individual cycle. Therefore, the remainder of the presentation in this chapter is focused on quantifying the variation of strain across the specimen cross sections as well as the variable amplitudes experienced during cycling.

The maximum tensile and compressive strains obtained from each specimen were obtained and summarized in Table 3.4. It is noted that the strain data was obtained from all valid strain gage readings. As seen from the data, all maximum strains in compression looked close while one of the maximum strain (specimen number 2) in tension reached extremely high due to concrete surface cracking.

All the tested specimens indicated an apparent micro-tension failure due to steel fibers pulled out

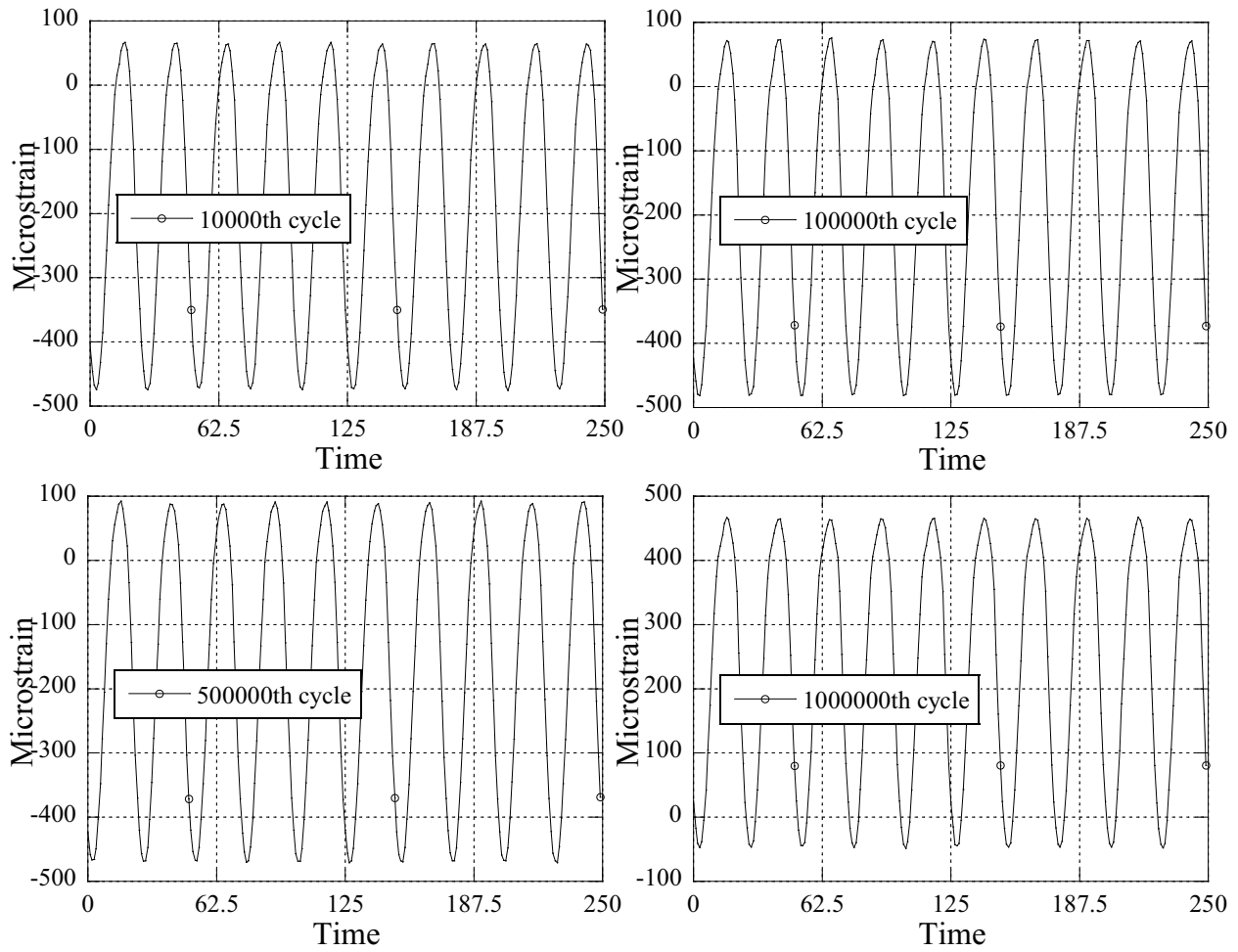
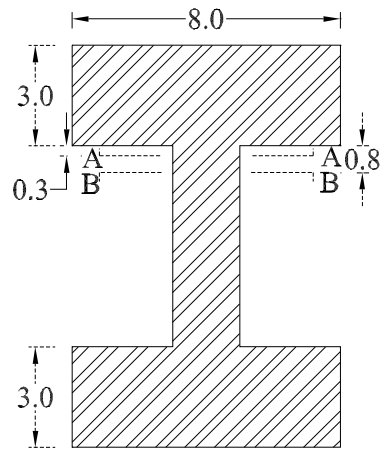


Figure 3.5: Specimen 3 Strain 1 (front) response at selected cycles

Table 3.4: Maximum tensile and compressive strain readings for all valid specimens

	Sp1	Sp2	Sp3	Sp5	Sp6	Sp7	Sp8
Max. Tension (microstrain)	194	2190	135	126	199	911	403
Max. Compression (microstrain)	-519	-473	-542	-668	-704	-610	-571



A-A: Cross section at which failure occurred (fig. on left)  
 B-B: Cross section near failed cross section (fig. below)



A-A Front View



B-B Top View

Figure 3.6: Samples of tensile fatigue failure due to steel fiber pulled out

as shown in Fig. 3.6. It was verified by cutting the cross section half inch off the failed surface as illustrated in Fig. 3.7. It is observed that all fibers at the failed cross section were vertical, however, a cross section nearby had lots of tiny pores due to fiber pulled out from the other side.

As mentioned, while the test was initially designed for a uniaxial tensile test with constant stress amplitude, varying strains were observed at different locations on the cross section. This flexural



Figure 3.7: Micro-tensile failure verification

response was due to many unexpected factors such as uneven contact surface between specimen and MTS box at top as well as W section at bottom and tightness of bolts used for connection of specimens to equipments. In addition, slight imperfections in the specimen web caused eccentricity issues throughout the test. Hence, the test eventually performed as a combination of axial tensile and flexural tests.

The load data was also recorded during the tests and post-processed into a stress to be used with the mean-stress fatigue life method in the analytical section of this chapter. The full cycle of each 1000th cycle was picked up from the original data with stress shown for specimen 2 and 8 in Fig. 3.8 and Fig. 3.9, respectively. Since the test was not an uniaxial tensile test any more, it is expected that the total (or average) stress on the cross section would no longer be accurate for the current set of data.

To reduce the volume of data recorded from the test, the complete cycle of each 1000th cycle, which consists of 25 data points, was used to represent each 1000 cycles (it was assumed any



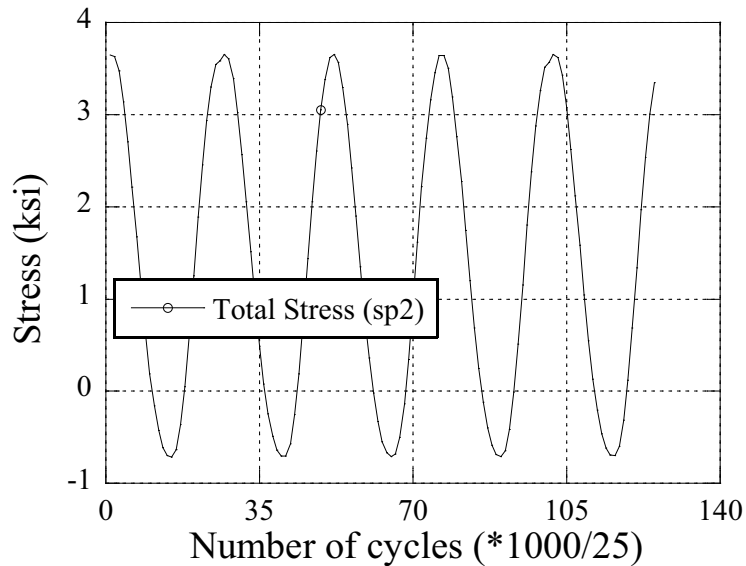


Figure 3.8: Stress response under cyclic loading in specimen 2

variation in the strain and load was small within any given set of 1000 cycles). In addition, the data of compressive behavior was removed as it is not the critical part of the analysis. Then all these individual tension cycles (each cycle now representing 1000 cycles) were concatenated into a new strain vs number of cycles relationship. Examples of the compile tension strain responses for specimen number 2 are shown in Fig. 3.10, specimen number 3 in Fig. 3.11, and specimen 8 as shown in Fig. 3.12, respectively.

Among all valid specimens, specimen number 3 was the only one that exhibited consistent compression and tension strains during cycling over the full number of cycles while all others exhibited error either from instrument or due to the concrete cracking during test. Some of the instrumentation errors exist all over the test, such as uneven surface of specimen in top and bottom, tightness of bolts used to fix specimen and asymmetry of specimen itself, have reflected in the test. For example, the jump in the strain gage 2 of specimen number 2 around cycle 65,000 occurred due to loosening of the tie-down bolts between the steel wide flange and the floor. The jump in the

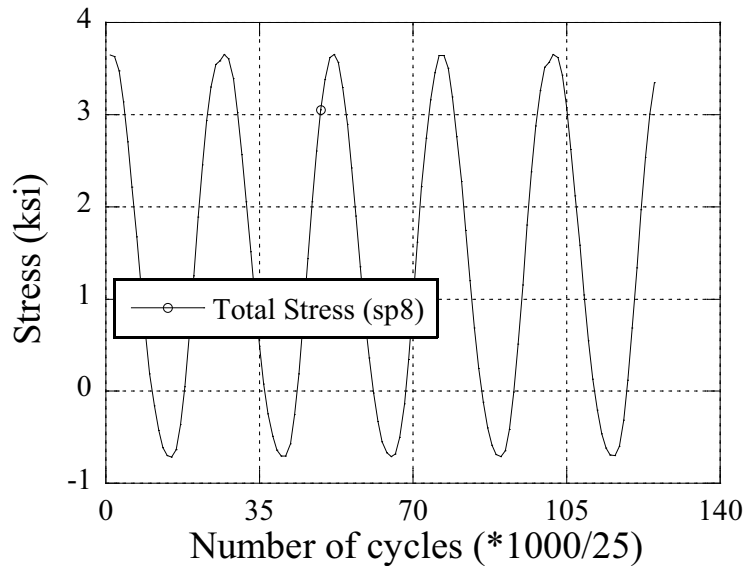


Figure 3.9: Stress response under cyclic loading in specimen 8

strain gage number 3 of specimen number 2 around cycle 20,000 occurred due to concrete surface drop off which lead the strain to a permanent maximum reading. The test for specimen number 3 was stopped after approximate 2,500,000 cycles and the specimen was monotonically tested until failure. The residual tension strength of the specimen after this number of cycles was 4.7 kip which indicated that the concrete component remained around 20% tension capacity after two and a half million cyclic loading.

### Analytical Work

Several approaches were taken to synthesize and interpret the experimental data with respect to fatigue life of the tested specimens. In this section, both strain life and mean stress approaches are presented. The strain life approach is carried out by using three different methods for analyzing strain data obtained from gages while the mean stress approach utilizes only the actuator load history. In addition, the calibrated strain life models are then implemented into a finite element

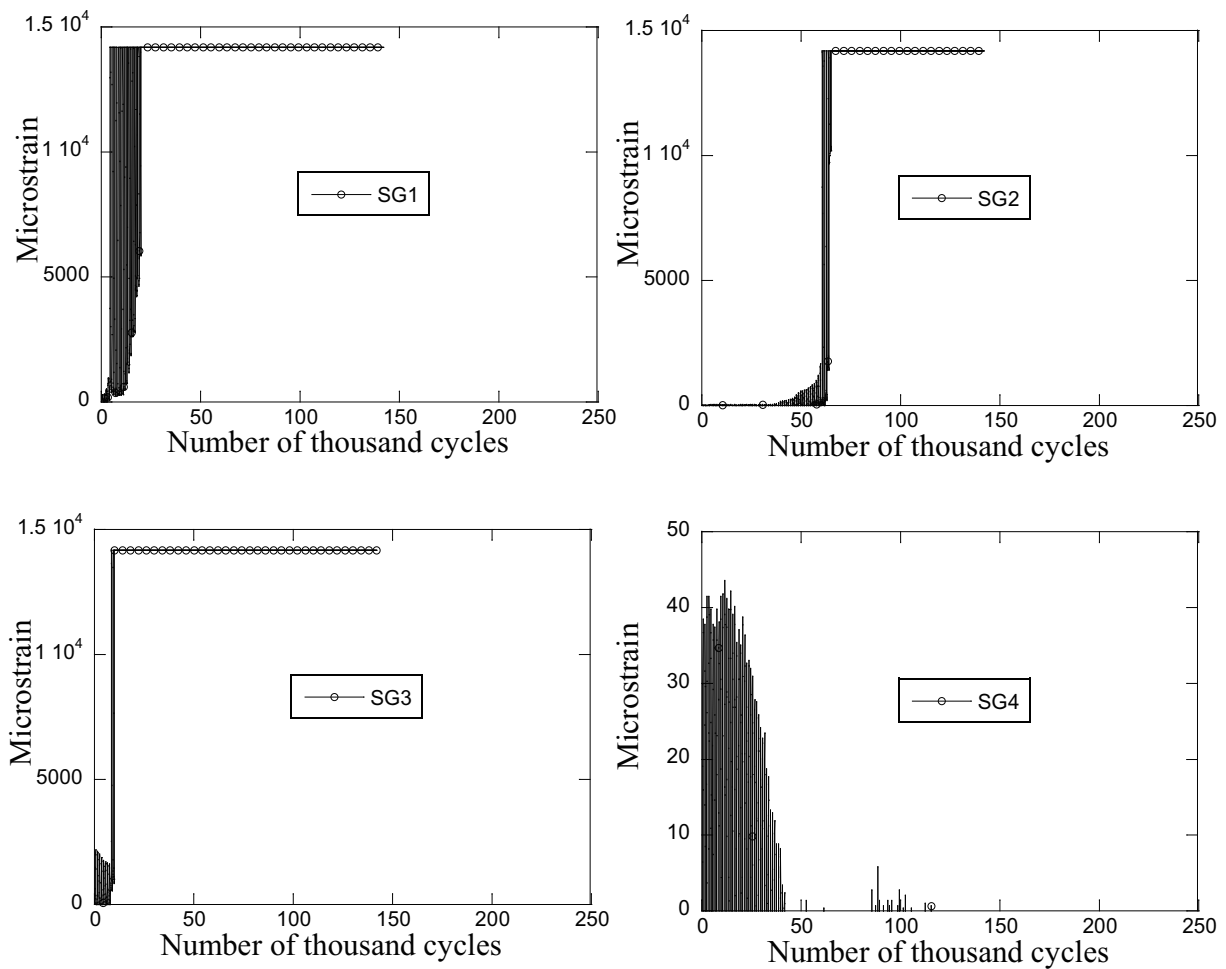


Figure 3.10: Compiled tension strain response versus number of cycles in specimen 2

code for use in numerical fatigue simulations using fiber-based beam-column elements.

The lack of constant stress or strain amplitudes applied to the specimens to failure prevented the standard fatigue life approaches from being taken. Therefore, a traditional strain life model could not be inferred from the specimen data (where each specimen represents a single point in the strain vs number of cycles space). Instead, the functional form of the fatigue life model was assumed, and the parameters of the model solved using the experimental data and the Palmgren-Miner damage accumulation typically performed during fatigue life predictions from variable amplitude test data.

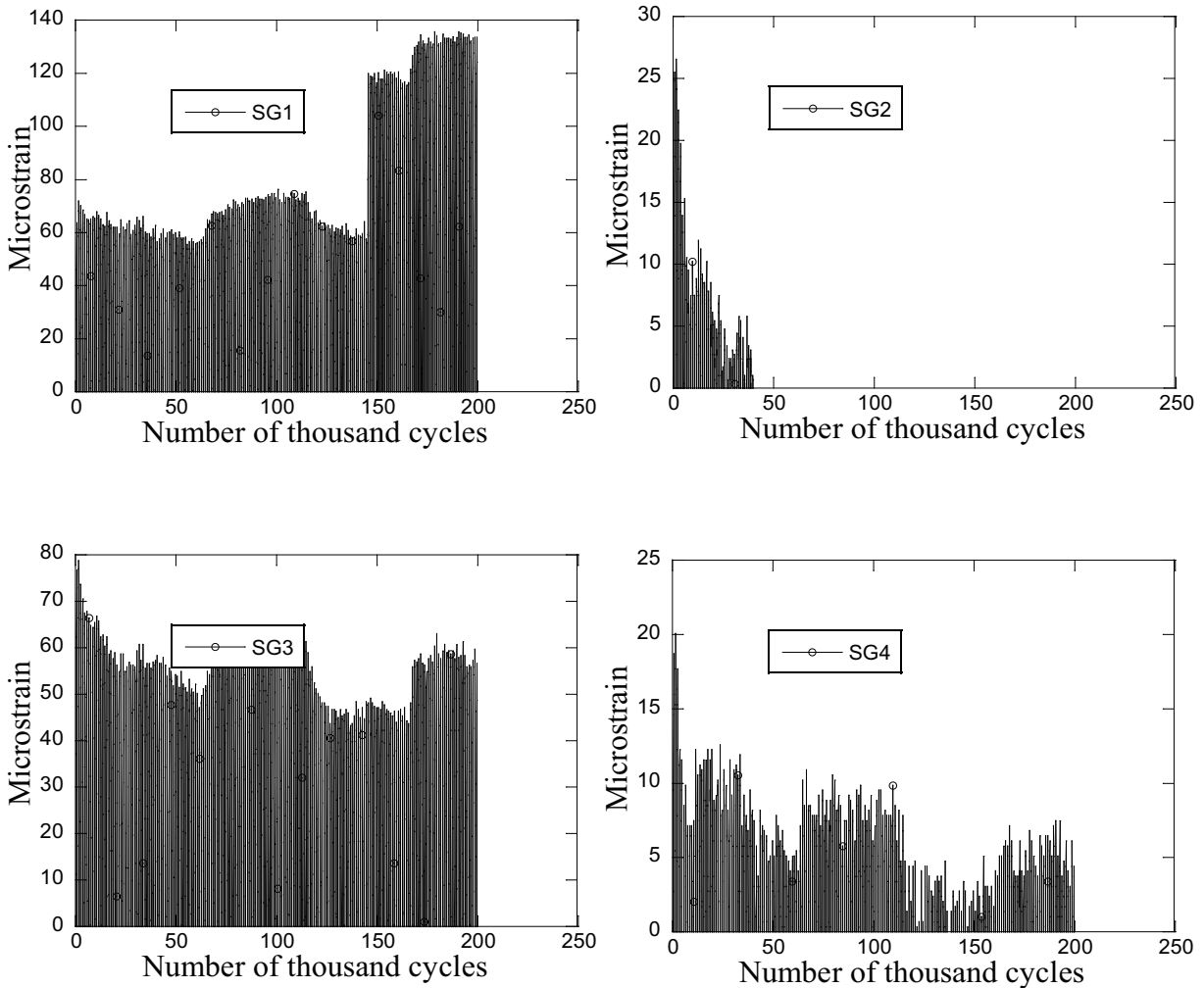


Figure 3.11: Compiled tension strain response versus number of cycles in specimen 3

Finally, as discussed previously, there were variable stress (or strain) levels that occurred in different locations on the cross section during test. It was assumed in the analyses herein that the concrete fiber experiencing the peak tensile strain would triggered fatigue failure. Therefore, simply using the recorded strain gage data was not sufficient, as the peak strains likely initiated at the specimen corners. The maximum vertex method utilized here assumed that plane sections remain plane, and that the linear damage rule can be applicable for the strain life approach at each location on the cross section.

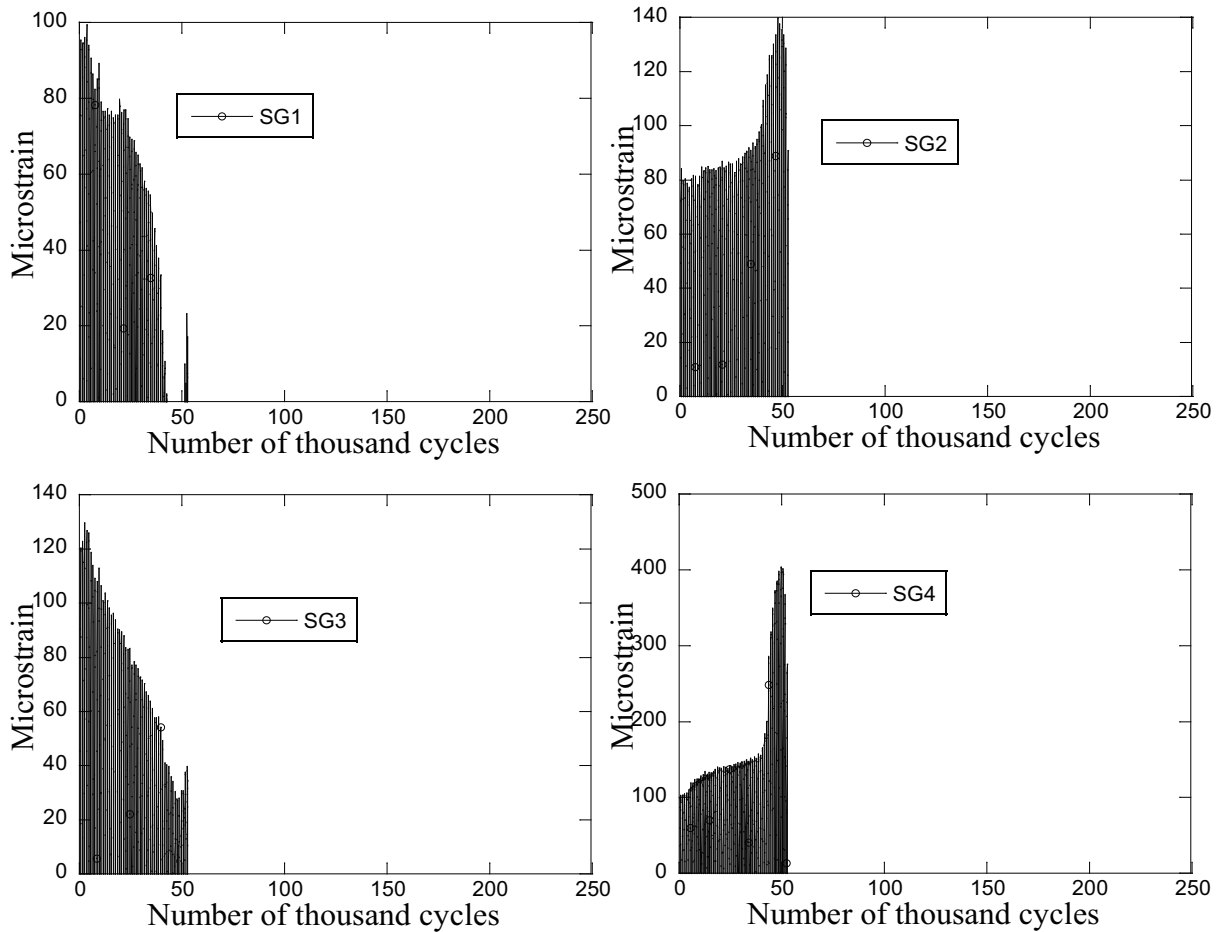


Figure 3.12: Compiled tension strain response versus number of cycles in specimen 8

*Strain Life Approach*

Three strain methods were adopted for analysis and are discussed. The first approach is named peak strain approach which only takes care of the individual maximum strain and does not consider the permanent or mean stresses that may be experienced during cycling at a location on the cross section (either due to the stress reversals being non-symmetric in tension and compression, or the flexural behavior experienced by the cross section). As long as any one of the strain gages reaches damage, the specimen would be defined as failure. The second approach is the mean strain

approach. This approach calculates the average accumulative strains in the entire tension process (tension strains are considered from the mean strain rather than from the zero point). The last approach, called maximum vertex approach, is slightly different with the peak strain approach. It accounts for the strain on the four vertices of the cross section rather than that on the four sides. Therefore, it is the superior method for accounting for strains due to the eccentricity issue.

The Palmgren-Miner damage accumulation model was adopted in the analysis, by Palmgren-Miner rule, the fatigue damage caused by a certain stress or strain level is defined in Eq. (3.3):

$$D_i = n_i/n_{fi} \quad (3.3)$$

where  $n_i$  is the number of full cycles of the applied stress or strain level and  $n_{fi}$  is the fatigue life for the same level of loading. Therefore, the total accumulated damage can be expressed in Eq. (3.4) for linear damage rule.

$$\sum_i^n n_i/n_{fi} = 1 \quad (3.4)$$

The Coffin-Manson curve is typically written as shown in Eq. (3.5) which can also be derived in Eq. (3.6). It indicates that the total strain contains both elastic strain and plastic strain. Since the test is UHPC specimens with high-cycle fatigue, due to the strong strain hardening property of the material, the elastic term can be neglected. Hence, the Basquin equation may be rearranged to be shown in Eq. (3.7):

$$\epsilon_{total} = \epsilon_e + \epsilon_p \quad (3.5)$$

$$\epsilon_{total} = \frac{\sigma_f}{E}(2N_f)^b + \epsilon_f(2N_f)^b \quad (3.6)$$

$$\epsilon_{N_f} = \epsilon'_f(2N_f)^b \quad (3.7)$$

where  $\epsilon_{N_f}$  is the strain corresponding to the fatigue life  $N_f$  (number of half cycles to failure) and  $\epsilon'_f$  is the fatigue ductility coefficient, e.g., the failure strain for a single reversal which is assumed to be 2500 microstrain for UHPC.

By substituting Eq. (3.7) into Eq. (3.4), the general expression for fatigue life based on strain can be derived, as shown in Eq. (3.8).

$$\sum_{i=1}^n \frac{1000}{\left(\frac{\epsilon_i}{2500}\right)^{(1/b)}} = 1 \quad (3.8)$$

where  $\epsilon_i$  is the maximum strain reading from each 1000 cycles and 2500 is the fatigue ductility coefficient. The equation represents a nonlinear equation that can be solved for the exponent  $b$ . The calculations were performed in Maple.

### *Peak Strain Method*

As discussed previously, the peak strain method only counts the maximum strain obtained from the tension part. Eq. (3.8) was solved using Maple for each of the four strain gages independently. The maximum tensile strain recorded from each 1000 cycles was substituted into Eq. (3.8) as  $\epsilon_i$ . The resulting fatigue strength exponents  $b$  are listed in Table 3.5. Some unavailable data in the table means the strain gage was invalid either due to instrumentation error or broken because of the concrete surface cracking in the test. The average strain data shown in the last column of the table represents the average number of the valid 4 (or 3)  $b$  values (and is not based on the average

Table 3.5: Calculated fatigue exponent  $b$  from maximum strain approach

Specimen Number	Strain Gage 1	Strain Gage 2	Strain Gage 3	Strain Gage 4	Avg. Strain
1	N/A	-0.6226	-0.3420	N/A	-0.4823
2	N/A	-0.4876	N/A	-0.4622	-0.4749
3	-0.2677	-0.5199	-0.3102	-0.4767	-0.3936
5	-0.4855	N/A	-0.3647	-0.4071	-0.4191
6	-0.3352	-0.3025	-0.5868	-0.5294	-0.4385
7	-0.1415	-0.5549	-0.2709	-0.3513	-0.3297
8	-0.3305	-0.2960	-0.3078	-0.2078	-0.2855

strain readings).

Consequently, by substituting the calculated average  $b$  into Eq. (3.7), the relationship of estimated strain life versus number of cycles of failure curve can be plotted as shown in Fig. 3.13. Several points need to be emphasized in relation to the plot. Firstly, for individual specimen, a straight line was generated to represent the relationship between strain and number of cycles due to the changing stress amplitude in the test, rather than the traditional standard uniaxial test which brings a single point data. Secondly, the plot was based on the assumption that the strain magnitude upon failure was 2500 microstrain. When the assumed strain decreases (it assumed to be closer to the tension yield strain), it actually will cause the fatigue exponent  $b$  to be larger, which makes the fatigue curve flatter. In other words, the fatigue life is even longer within certain stress life, e.g., the result presented in current analysis is conservative. Thirdly, the plot from individual specimens indicated close result. The plot with average fatigue exponent  $b$  was presented as well which was used for future comparison with result from other approaches.

#### *Mean Strain Method*

Since it is assumed that the compressive load has no impact to fatigue life damage in this test, the mean tension strain data was simply used with half of the strain obtained from maximum



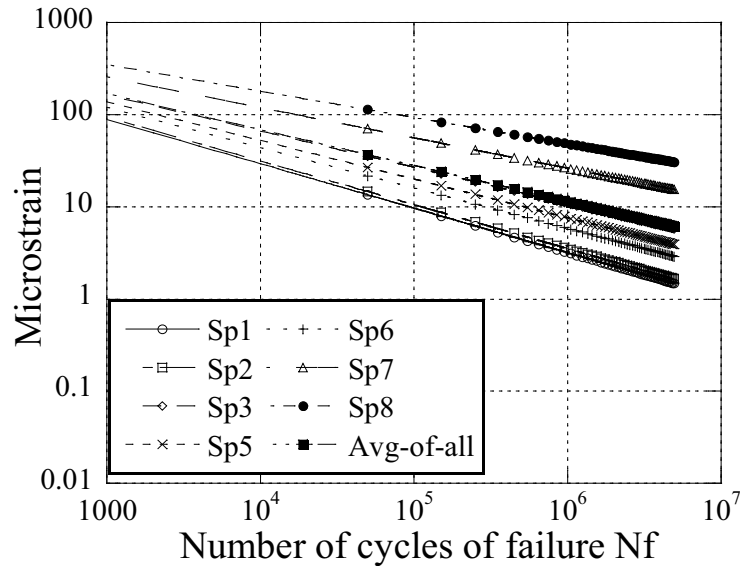


Figure 3.13: Estimated fatigue strain life curve of UHPC by peak strain approach

strain approach. By applying the same procedure listed in previous approach, the fatigue strength exponent  $b$  from mean strain method was calculated as listed in Table 3.6. Substitute calculated  $b$  into Eq. (3.7) and plot the estimated strain life curve as shown in Fig. 3.14. It is seen that from both maximum strain approach and mean strain approach, the plot of specimen 8 stands a little away from the others. This matches the data that specimen 8 reached a relative high number of cycles with high applied tensile load (40% of critical tensile load). The exponent results from the mean strain approach are of course larger than those obtained from the maximum strain approach.

#### *Maximum Vertex Method*

Due to the eccentricity and bending experienced by the specimens during testing, the peak strain is more likely to occur at the corners of the specimen where fatigue cracking will initiate. Therefore, it was assumed that plane sections remained plane during the tests, and the curvature could be computed from the strain gage responses (curvature was assumed to be constant about each axis

Table 3.6: Calculated fatigue exponent b from mean strain approach

Specimen Number	Strain Gage 1	Strain Gage 2	Strain Gage 3	Strain Gage 4	Avg. Strain
1	N/A	-0.7106	-0.4294	N/A	-0.5700
2	N/A	-0.5648	N/A	-0.5394	-0.5521
3	-0.3272	-0.5898	-0.3673	-0.5353	-0.4549
5	-0.5672	N/A	-0.4420	-0.4867	-0.4986
6	-0.4168	-0.3839	-0.6741	-0.6109	-0.5214
7	-0.2340	-0.6425	-0.3624	-0.4287	-0.4169
8	-0.3968	-0.3609	-0.3741	-0.2807	-0.3531

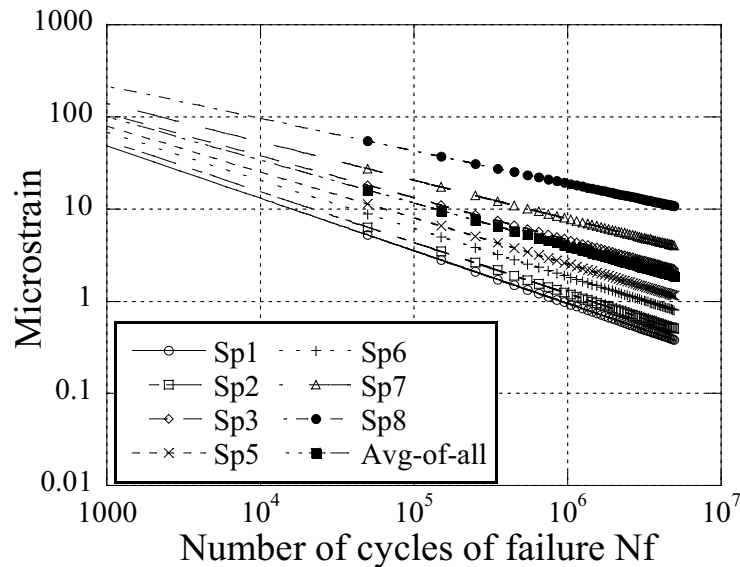


Figure 3.14: Estimated fatigue strain life curve of UHPC by mean strain approach

of the cross section consistent with the plane sections assumption). Therefore, it will theoretically bring the analysis closer to the real case and the results should exhibit less dispersion between specimens.

It is illustrated in Fig. 3.15 that A, B, C, and D are the location of the four gages on each face of the specimen web and a, b, c, and d are the locations of the four vertices where the maximum strain condition must exist (if plane sections remain plane). The equation of the plane is defined in

Eq. (3.10) and can be characterized uniquely using the three constants in Eq. (3.9). These quantities ( $\epsilon_a$  is the axial strain at the centroid and  $\kappa_z$  and  $\kappa_y$  are the curvatures about each section axis) are group together as a vector  $\mathbf{e}$  and represent the section deformations.

Obviously, there were only 3 unknowns in Eq. (3.10), but in a majority of cases 4 strain gages data available. Therefore, the numerical least squares method with equation expressed in Eq. (3.9) was used to minimize eccentricity effect raised in the test. however, as observed from the test, sometimes one of the four attached strain gages failed due to concrete crack or specimen damage which made the least square result to be unique. Consequently, the maximum strain was obtained from one of the four vertices where the maximum strain concluded by using Eq. (3.10) and Eq. (3.11).

$$\mathbf{e} = \{\epsilon_a, \kappa_z, \kappa_y\} \quad (3.9)$$

$$\epsilon(y, z) = \epsilon_a - y\kappa_z + z\kappa_y \quad (3.10)$$

$$\epsilon_m = \max \left\{ \epsilon\left(-\frac{b}{2}, \frac{b}{2}\right), \epsilon\left(-\frac{b}{2}, -\frac{b}{2}\right), \epsilon\left(\frac{b}{2}, \frac{b}{2}\right), \epsilon\left(\frac{b}{2}, -\frac{b}{2}\right) \right\} \quad (3.11)$$

Apply the same procedure discussed previously, calculate the fatigue strength exponent  $b$  from maximum vertices strain method as listed in Table 3.7. Substitute calculated  $b$  into Eq. (3.7) and plot the estimated strain life curve as shown in Fig. 3.16.

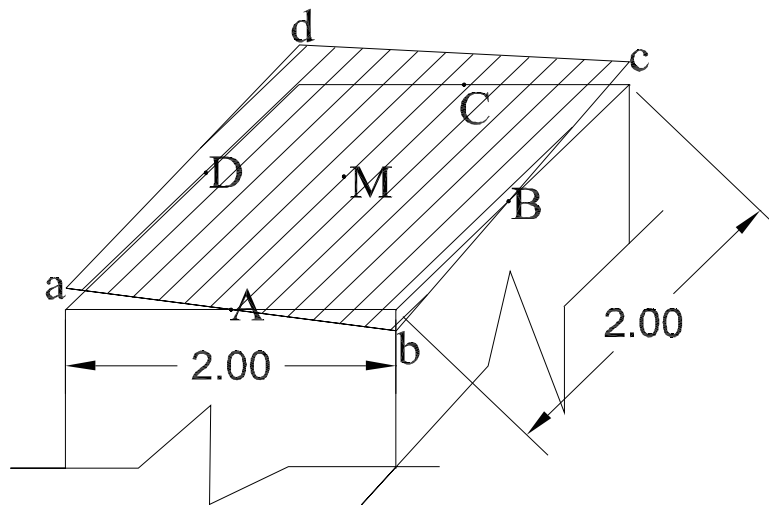


Figure 3.15: Illustration of strain gages and maximum vertices strain locations

Table 3.7: Calculated fatigue exponent  $b$  from maximum vertices strain method

Specimen number	Corresponding computed $b$
1	-0.27238
2	N/A
3	-0.29962
5	-0.30398
6	-0.27469
7	-0.16751
8	-0.23717

#### *Mean Stress Approach*

Besides the strain data obtained directly from the attached gages, the load was also recorded from the data acquisition (DAQ) system. Due to the limitations inherent in the recorded strain data such as strain gages damage or error, the strain life methods presented above may also have some disadvantages on the corresponding fatigue life curves generated. Therefore, the mean stress approach was also applied to compare with the analysis from the strain life approaches. By using the mean stress approach, it is assumed that the stress is irrelative to strain and only corresponded from

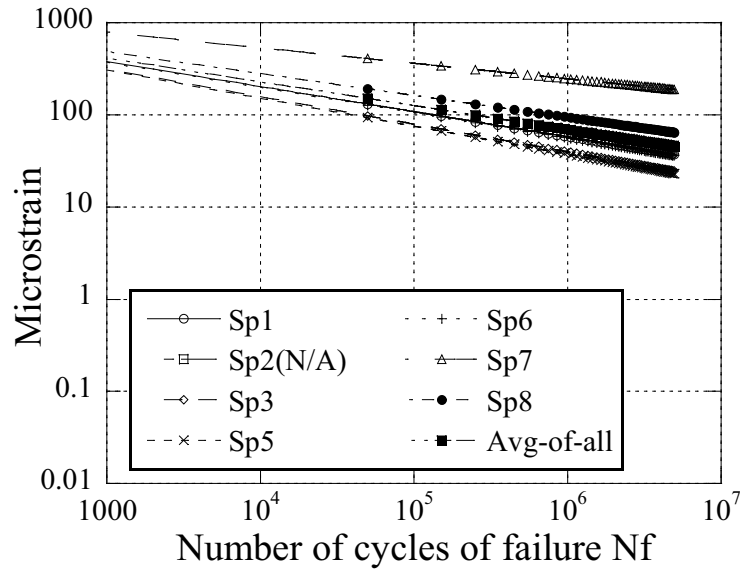


Figure 3.16: Estimated fatigue strain life curve of UHPC by max vertices strain method

applied cyclic load. The historical stress data was computed directly from the cyclic load.

By rearranging Basquin's equation, the stress life fatigue can be expressed as shown in Eq. (3.12) where  $\sigma'_f$  is the stress of tension close to material failure. A value of 1.5ksi was applied in the analysis. By substituting it into Eq. (3.8), the fatigue strength exponent  $b$  from stress approach was found as listed in Table 3.8. Also, by substituting the calculated  $b$  into Eq. (3.12), the plot of estimated stress vs number of cycles of failure was shown in Fig. 3.17.

$$\sigma_{N_f} = \sigma'_f (2N_f)^b \quad (3.12)$$

The difference of estimation from the three strain approaches discussed above was summarized in Fig. 3.18. As concluded from the mean stress approach, the average stress at number of cycles by 100,000 is close to 0.6 ksi which indicated a strain level of 75 microstrain (consider modulus of

Table 3.8: Calculated fatigue exponent b from mean stress approach

Specimen number	Corresponding computed b
1	-0.75770
2	-0.72403
3	-0.71925
5	-0.85966
6	-0.95224
7	-0.91747
8	-0.76538

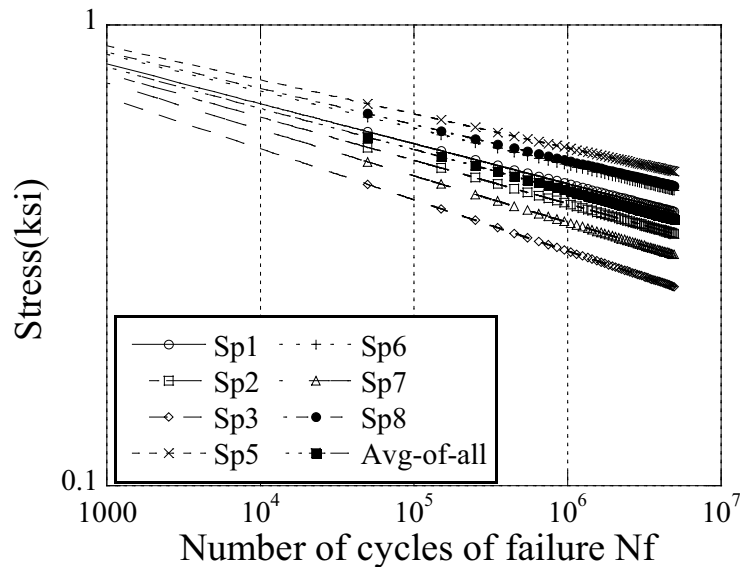


Figure 3.17: Estimated fatigue strain life curve of UHPC by mean stress approach

elasticity of UHPC as of 8000). It is located between the figure from maximum strain approach and maximum vertex approach. e.g., it is the farthest from the fatigue analyzed by mean strain approach. This might be due to the reason that only limited number of cycles was involved in mean strain calculation. Since with strain approach, the strain data becomes invalid once gage damaged. However, with stress approach, data is valid until failure of the specimen cross section, even if strain gages fail during such time. However, the predominant reason relates to the assumption that the stress at each cycle is accumulating damage relative to  $\sigma'_f$ , whereas a majority of the time, the

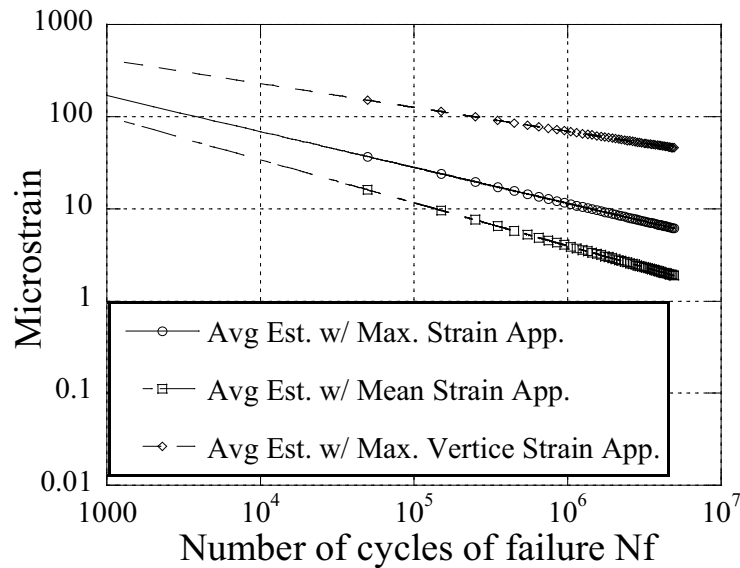


Figure 3.18: Comparison of estimated strain vs Nf from all presented approaches

vertices of the specimen were experiencing strains into the strain hardening region.

### Opensees Modeling Approach

To compare with the analytical result processed from experimental data, a numerical computer model of the cross section was built in OpenSees (<http://opensees.berkeley.edu/>) to perform some analytical analysis of the experimental data as well as for some predictive analysis. In the model, both compressive and tensile cyclic behaviors were considered. The stress strain relationship adopted was shown in Fig. 3.19. The cross section was discretized into a 40 by 40 grid of equally sized fibers. The concrete compressive strength of 18ksi and Poisson's ratio of 0.17 were used. The tensile strength was assumed to be 14% of the compressive strength. In addition, the maximum elastic compressive strain of concrete was assumed to be 0.00223 and ultimate compressive strain to be 0.007.

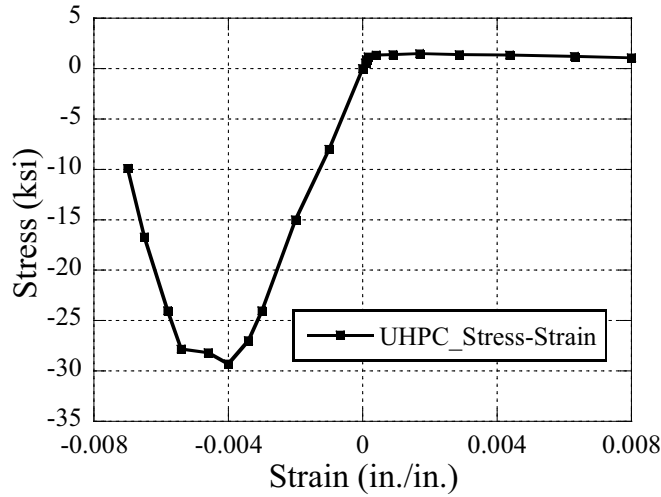


Figure 3.19: Strain strain relationship adopted for Opensees modeling

Since the stress level in different locations keeps on changing, the rainflow counting algorithm was coded into OpenSees. The demand on the cross section was specified directly as the vector of section deformations described above in the maximum vertex method. A verification of specimen number 6 with fatigue strength exponent  $b$  of  $-0.274689$  (obtained from maximum vertex strain approach) and UHPC failure strain in tension of  $2500$  microstrain was used for model analysis. For each specimen, all valid complete cycles with  $25$  data points each as discussed previously in strain approach were imposed on the cross section. The The predicted results from OpenSees model such as number of cycles, axial force versus displacement, moment about the  $x$  axis, moment about the  $z$  axis are illustrated in Fig. 3.20, Fig. 3.21, Fig. 3.22 and Fig. 3.23, respectively.

In order to make the numerical calculation complete faster, the Opensees model was coded to count  $10$  cycles as  $1$  reflected in the time axis of Fig. 3.20. Hence, the corresponding number of cycles upon failure in Fig. 3.20 can be expressed as Eq. (3.13)

$$f(x) = \frac{10x}{25} \tag{3.13}$$



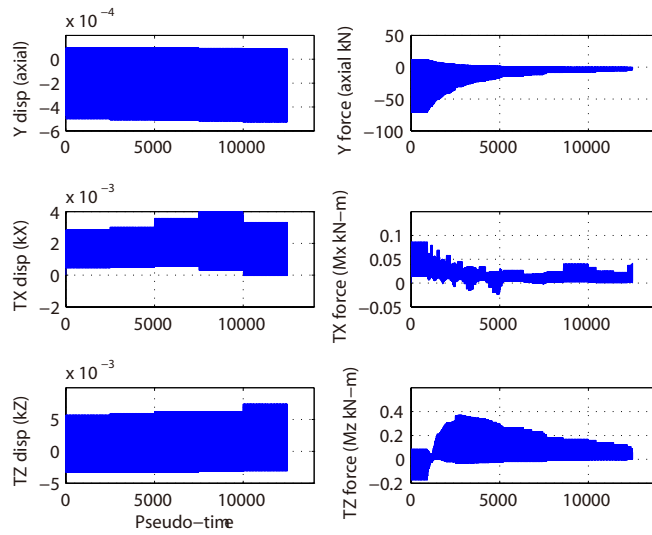


Figure 3.20: Predicted fatigue force vs number of cycles of failure for sp6

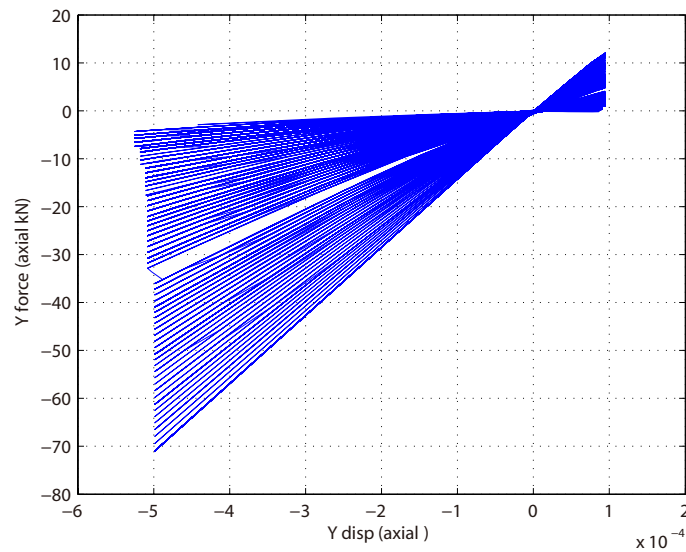


Figure 3.21: Predicted fatigue force vs displacement for sp6

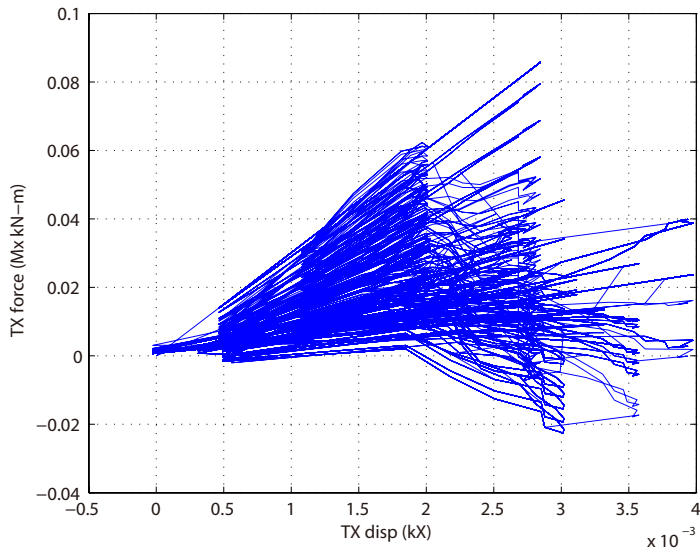


Figure 3.22: Predicted fatigue moment  $M_x$  vs displacement for sp6

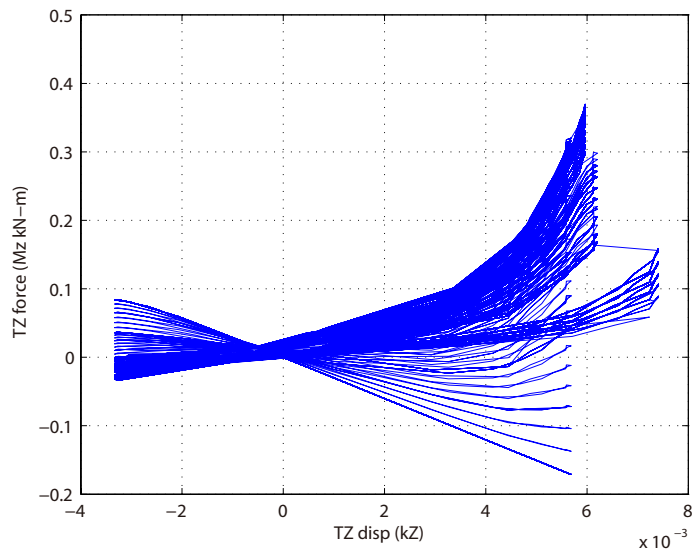


Figure 3.23: Predicted fatigue moment  $M_z$  vs displacement for sp6

where  $x$  is number as shown by  $x$  axial in Fig. 3.20,  $f(x)$  is corresponding number of cycles. In the plot of  $Y$  force versus number of cycles shown in Fig. 3.20, it well captured number of cycles based on each given force. The other two plots of  $M_x$  and  $M_z$  versus number of cycles described specimen rotation to both  $x$  and  $z$  directions. It gives guidance how specimen real performed in the test.

## **Chapter Conclusion**

In this chapter, a series of uniaxial tension fatigue test was performed. Reversed stress conditions were used in order to investigate compressive strength influence on the tensile fatigue behavior. The curves of strain versus number of cycles upon failure were estimated by using several different approaches.

The largest number of cycles achieved during the test reached as high as two and half millions under a given combination of compression stress with magnitude of approximately 20% of the maximum strength and tensile stress with magnitude of approximately 33% of maximum tensile strength. The specimen tensile strength decreased to around 20% of its original strength after 2.5 million cyclic fatigue loading. This indicated a more than expected strength lost in the tensile strength and post safety threat for those structures failed mainly due to shear. The fatigue strength of shear is highly related to the tensile fatigue strength and worth investigation. However, the test approaches used in this research has some limitations and drawbacks. The uniaxial test is generally hard to do due to alignment issue. The gripping is another problematic part for concrete test in tension. The designed test setup used in this research minimize the impact of gripping by using bolt connections, however, at the same time suffered from inevitable misaligned stress concentration. The test results gave some fundamental test results on the fatigue uniaxial tensile stress and in the future flexural fatigue tests will be performed to further quantified the tensile

fatigue behavior.

## **CHAPTER 4: MID-SCALE UHPC “T” SECTION BEAMS INVESTIGATION**

### **Introduction**

As mentioned in chapter 1 that in order to qualify for the increased traffic loads, two new combined systems titled “UHPC-MMFX” system and “UHPC-CFRP” system were introduced. Each of the two systems has its advantages and shortcomings. The “UHPC-MMFX” combined system would exhibit much higher strength capacity due to the high stiffness and formability of the steel. However, the heavy self weight of the steel would bring difficulty on installation and construction as well as concerns on bridge deck dead load. The “UHPC-CFRP” combined system would demonstrate higher ultimate tensile strength and lighter self weight due to the specialty of CFRP bar. However, a fundamental issue in using CFRP steel is that the stress at service load is expected to be greater than when conventional steel such as Grade 60 is used. Consequently, the service-load reinforcing strains are larger than those from conventional steel. The larger strains affect deflection and crack widths at service loads. Hence, deflections and crack widths at service load levels require evaluation.

Based on the particular properties of these two systems, issues need to be investigated include but not limit to optimization of “UHPC-MMFX” system for an appropriate cross section with the highest ratio of load capacity to weight, evaluation of “UHPC-CFRP” system deflection, estimation of shear reduction of “UHPC-CFRP” system and estimation of CFRP bar strength attribution ratio and so on.

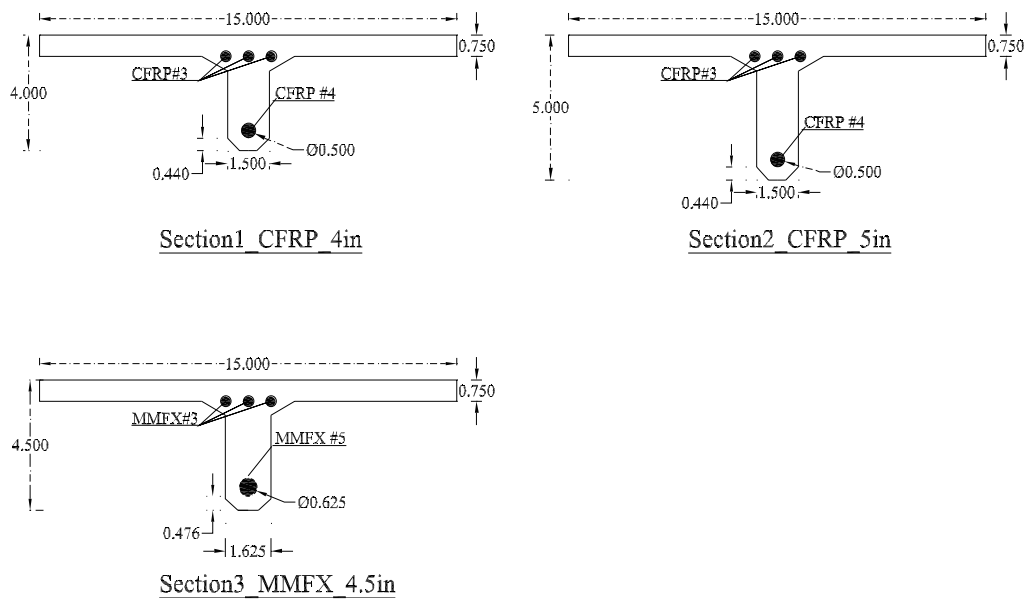


Figure 4.1: Designated beam with cross section details

## Experimental Work

A deck system including self weight up to 17 psf was considered a qualified system in current project. In order to achieve the goal, two types of sections with MMFX and CFRP as reinforcement were proposed as listed in Fig. 4.1.

The “UHPC-MMFX” system was used to verify strength qualification while the “UHPC-CFRP” system was used to investigate the deflection response at service load level. Meanwhile, the two CFRP sections in different height were used to verify if the one with less height would qualify for all of the designated requirements as well. In addition, the general cost on each section was estimated. A 3-D finite element model was created as shown in Fig. 4.2 to simulate the practical case and the preliminary results show that both the load capacity and amount of deformation are highly correlated to the interface properties, which represents the bond condition between the rebar and surrounding UHPC. A minimum of 5% load capacity over the demand load was estimated

based on the design parameters as listed in Table 4.1.

Table 4.1: Designated T section beams property

	Properties	Section 1	Section 2	Section 3
General	Height of section (in)	4	5	4.5
	Width of web (in)	15	15	15
Weight	Self-weight deck only	13.98	15.27	16.33
	Total self-weight	18.63	20.36	21.77
	Failure mode	CFRP Rupture	CFRP Rupture	MMFX Ultimate
Capacity	Demand Load (lb)	15524	15524	15524
	Estimated Capacity/Demand	1.05	1.37	1.16
Cost	Cost per unit specimen	\$156.20	\$162.90	\$43.00

For each section mentioned above, a number of two “T” beams were casted in March 2013 at the engineering center of Florida International University (FIU) with detailed dimensions as shown in Fig. 4.3 (MMFX sample) and Fig. 4.4 (CFRP sample), respectively.

All designed sections had flange thickness as thin as 0.75 inch and two blocks with length of 6 inch each were casted at both sides of the “T” beam. For the MMFX reinforced section, three U.S. number 3 MMFX bars were embedded in the flange while one U.S. number 5 MMFX bar embedded in the web for reinforcement. Additionally, a 180 degree rebar hook was well made to prevent bar slip. For the CFRP reinforced sections, three U.S. number 3 CRRP bars were used in the flange and one U.S. number 4 CFRP bar used in the web. Since it is ineligible to bend for anchorage, a 3 inch rebar extension was made out of the concrete block at each side and then wrapped by CFRP sheet as shown in Fig. 4.5a to form an end anchorage in order to minimize the bar slip. Upon loading, a steel plate sized at 10 inch by 10 inch was placed in the middle of the top beam to transfer load from MTS to the specimens. Three string potentiometers with distance of 5 in were located transversely below the middle line of the beam to measure the deflection illustrated in Fig. 4.6. All specimens were tested with displacement control at a rate of 0.015 inch/min with sample view in Fig. 4.7.

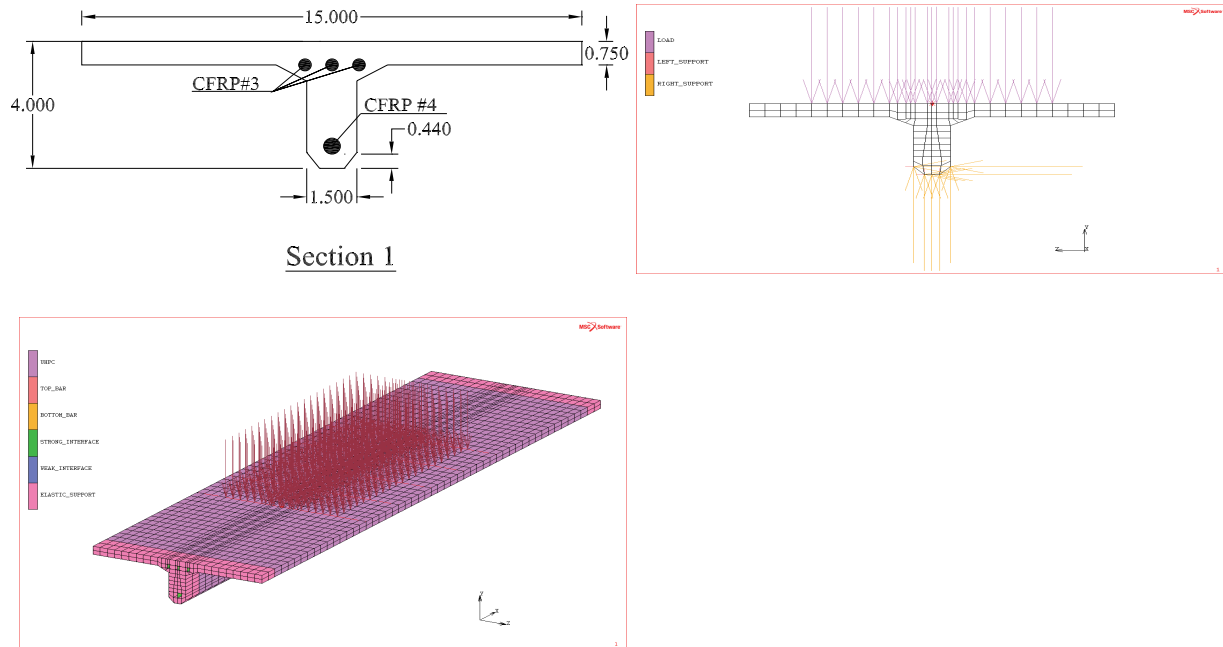


Figure 4.2: 3D simulation for section 1 “UHPC-CFRP”

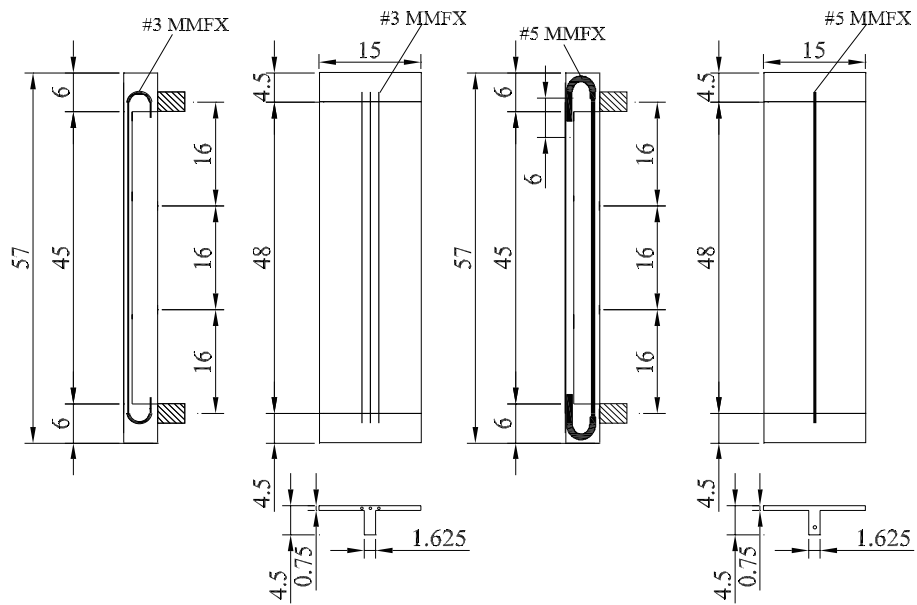


Figure 4.3: Designed MMFX reinforcing system layout



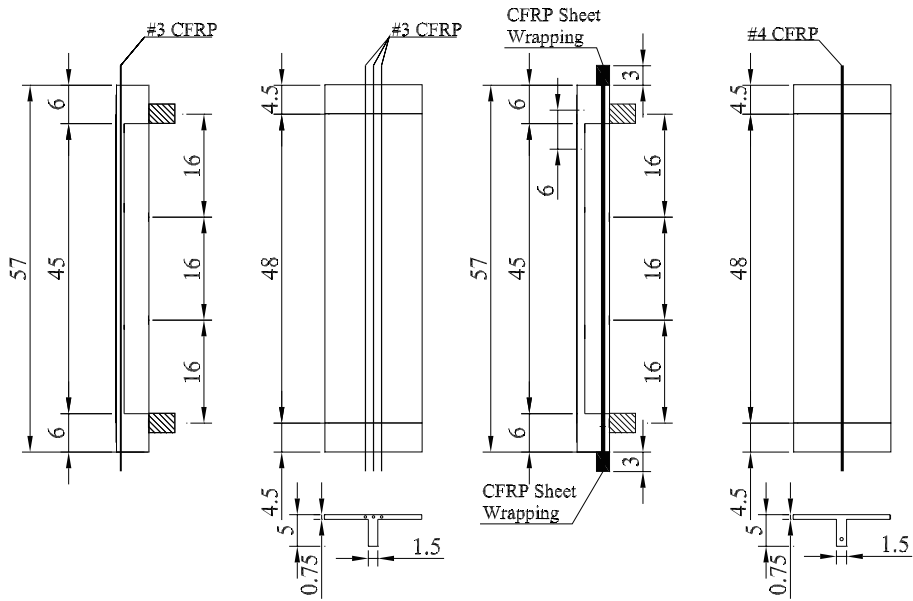


Figure 4.4: Designed CFRP reinforcing system layout (h=5' sample)



(a) End anchorage for CFRP Rods



(b) Close up view of CFRP Rod slippage

Figure 4.5: Anchorage processing for CFRP specimens before and after test

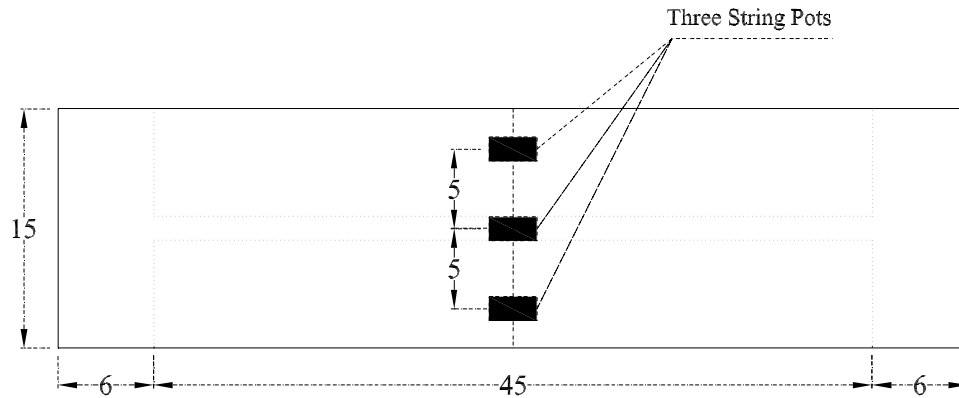


Figure 4.6: String pots instrumentation

## Results and Discussion

As expected, specimens reinforced with MMFX rebar initiated obvious shear cracks as seen in Fig. 4.8a. As the load increased, the shear cracks widened as seen in Fig. 4.8b till a shear failure occurred as observed in Fig. 4.9. It is consistent with previous work done by Jun [5], the failure is rather ductile than brittle. The load increased with the widen of the shear cracks, and then decreased slowly with the opening of the crack directly under the loading pad.

On the other side, specimens with CFRP bar as reinforcement exhibited both flexural crack as seen in Fig. 4.10a and shear crack as seen in Fig. 4.10b.



Figure 4.7: Test setup and instrumentation of “UHPC-MMFX” specimen

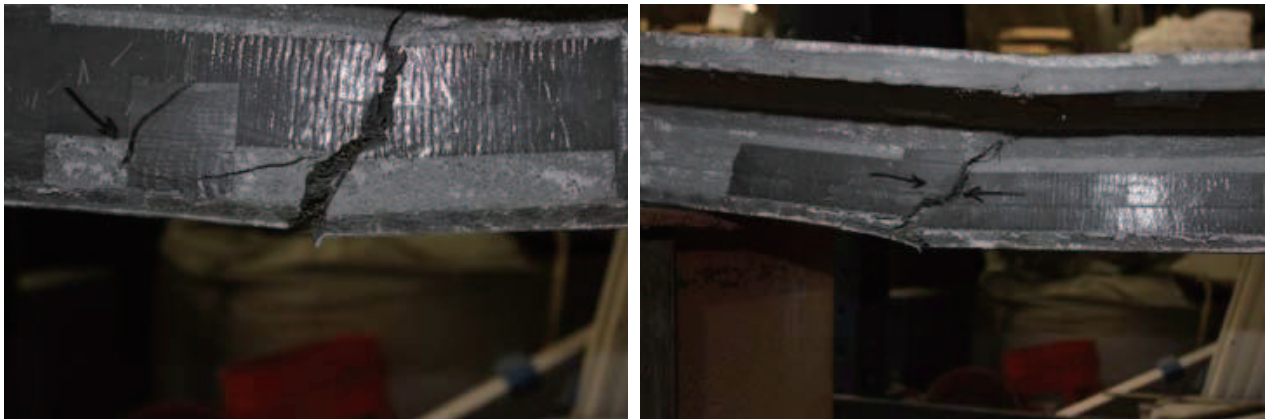


(a) Formation of shear cracks in “UHPC-MMFX” specimen (b) Shear cracks opening in “UHPC-MMFX” specimen

Figure 4.8: Crack observation for “UHPC-MMFX” specimens



Figure 4.9: “UHPC-MMFX” specimen prior to failure



(a) Formation of flexural cracks in “UHPC-CFRP” specimen

(b) Shear cracks opening

Figure 4.10: CFRP cracks

The load versus displacement responses of all three reinforced sections obtained from the test were listed in Fig. 4.11, Fig. 4.12, and Fig. 4.13, respectively. The “UHPC-MMFX” specimens demonstrated apparent plastic yield while the “UHPC-CFRP” specimen demonstrated no apparent yield point. When compared between the two CFRP reinforced sections, the one with less depth

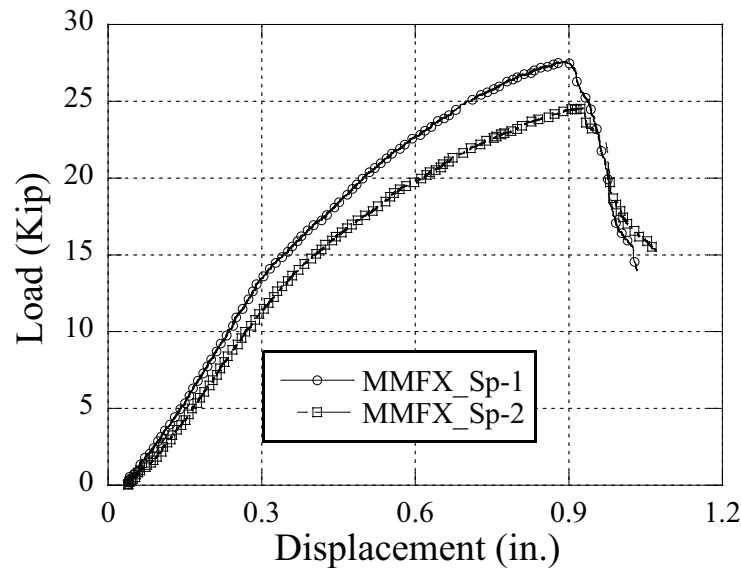


Figure 4.11: Load vs displacement for “UHPC-MMFX” specimens

exhibited larger deflection which qualifies with the maximum deflection theory. On the other hand, It is obviously that the beam reinforced with MMFX exhibited relatively higher peak load as well as smaller deflection which were generally attributed from the anchorage of the bar. For the beams reinforced with CFRP bar, although an end rod was prepared, it seemed the bar slip was not quite effectively prevented. A obvious bar slip was observed after failure of the specimen with photo shown in Fig. 4.5b. The CFRP bars did not achieve the ultimate tensile strength thus did not make the full contribution to the strength resistance. Flexural crack happened due to bar slippage which caused a even larger deflection. Hence, potential optimization such as how to reduce deflection at service load level are required for CFRP reinforced beam.

The load and strain responses of all three reinforced sections were illustrated in Fig. 4.14, Fig. 4.15, and Fig. 4.16, respectively. One strain gage from “UHPC-MMFX” specimen failed while the other one demonstrated a strain of approximately 0.0016 at service level load of 15524 lb. However, the strain obtained from both 4-in and 5-inch “UHPC-CFRP” specimens indicated concrete yield

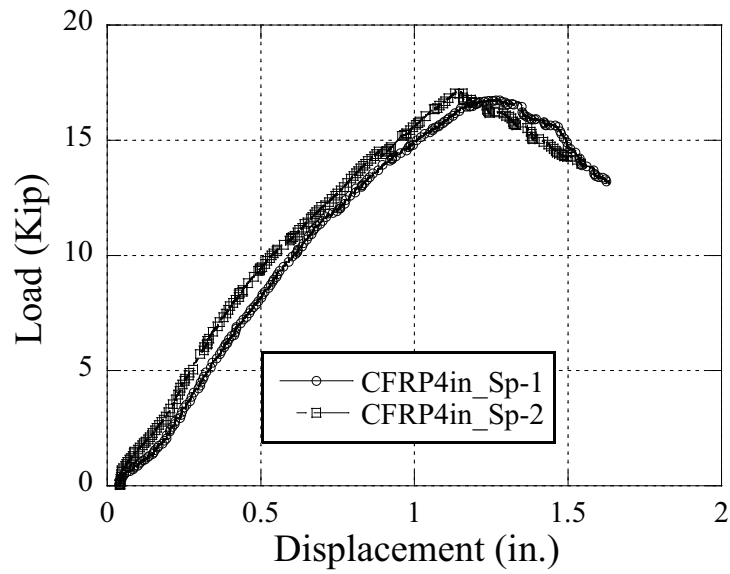


Figure 4.12: Load vs displacement for “UHPC-CFRP” specimens in 4’ height

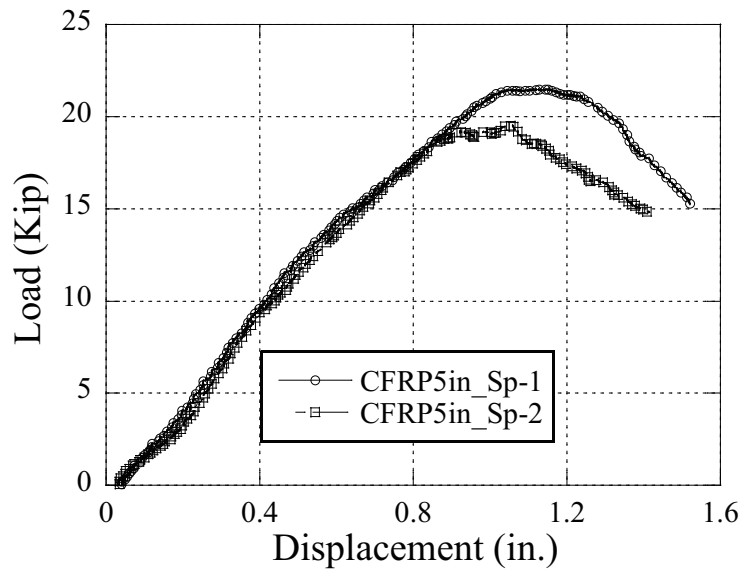


Figure 4.13: Load vs displacement for “UHPC-CFRP” specimens in 5’ height

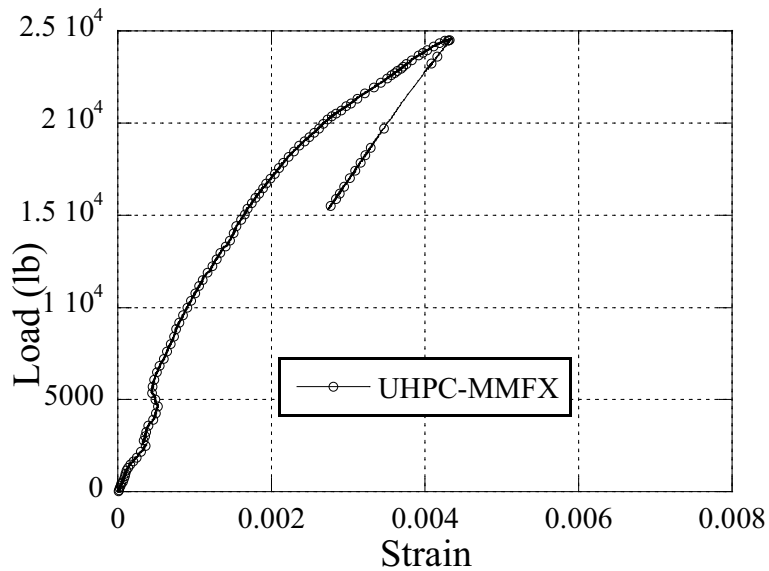


Figure 4.14: Load vs strain for “UHPC-MMFX” specimens

before it reached the service level load.

The MMFX reinforced specimens indicated a much higher excess load capacity than the prediction which was summarized previously in Table 4.2 while CFRP reinforced specimens indicated a very good match of excess load capacity with the predicted 1-D model. Therefore, additional optimization work required for MMFX reinforced section was to reduce material usage at the same load capacity level or reduce bar reinforcing ratio to achieve a design section with highest ratio of load capacity to deck self weight.

In order to reduce the deflection in CFRP reinforced beam, several alternative methods were available. For example, increase the bond capacity of UHPC and CFRP bar, increase the bar size to provide more available bar strength, extend bar length out of the concrete block to minimize bar slippage, or even to lock the CFRP bar at the end to prevent the slippage. By considering the feasibility of real situation, to increase the bar size would be potentially the best solution to the issue. Since a larger bar provides wider contact area with concrete which means a higher bond capacity.

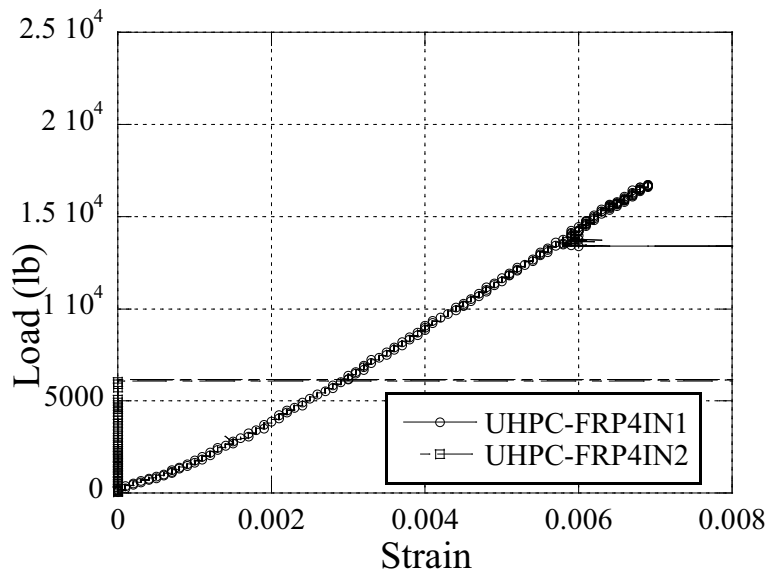


Figure 4.15: Load vs strain for “UHPC-MMFX” specimens in 4’ height

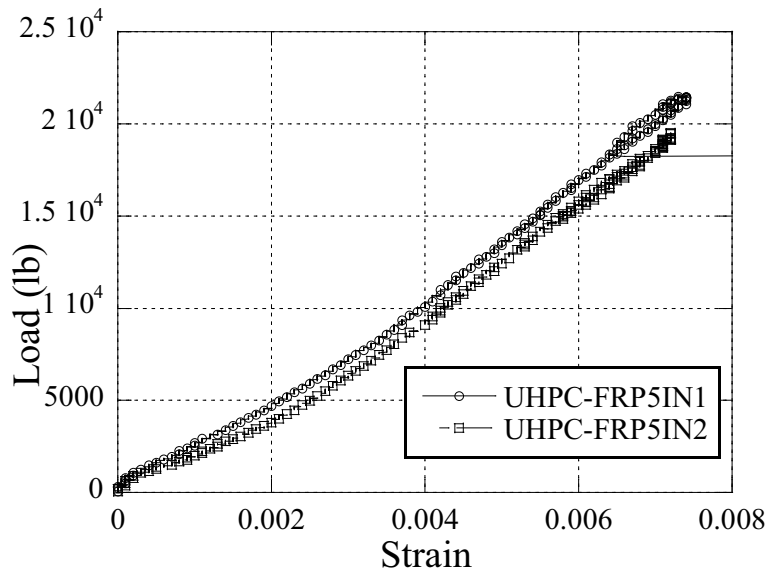


Figure 4.16: Load vs strain for “UHPC-MMFX” specimens in 5’ height



Table 4.2: Test results summary

Section No.	Specimen Type	Specimen No.	Ultimate Displacement (in.)	Ultimate Load(lb) (in.)	Demand Load(lb) (lb)	Average Excess Capacity
1	UHPC-CFRP 4in	1	1.60	16760	15524	9%
		2	1.72	17139	15524	
2	UHPC-CFRP 5in	1	1.44	21527	15524	32%
		2	1.46	19543	15524	
3	UHPC-MMFX 4.5in	1	1.11	27581	15524	68%
		2	1.11	24595	15524	

In addition, a larger bar provides more strength capacity which will offset the bar strength loss due to the slippage. However, the use of CFRP bar with potential slip of the end anchorage motivated a CFRP bar strength utilization ratio study that is presented next.

*Bar strength utilization ratio study*

The T section beam reinforced by MMFX bars adopted in the design was illustrated in Fig. 4.17 with all parameters marked. Apply the differential equation for each segment as shown in Eq. (4.1):

$$\left\{ \begin{array}{l} (EI)_{sys}y_1'' = -M_1 = -x\frac{P}{2} \quad 0 \leq x \leq a \\ (EI)_{sys}y_2'' = -M_2 = -\left(\frac{Px}{2} - \frac{\omega(x-a)^2}{2}\right) \quad a \leq x \leq a + b \\ (EI)_{sys}y_3'' = -M_3 = -(2a + b - x)\frac{P}{2} \quad a + b \leq x \leq 2a + b \end{array} \right. \quad (4.1)$$

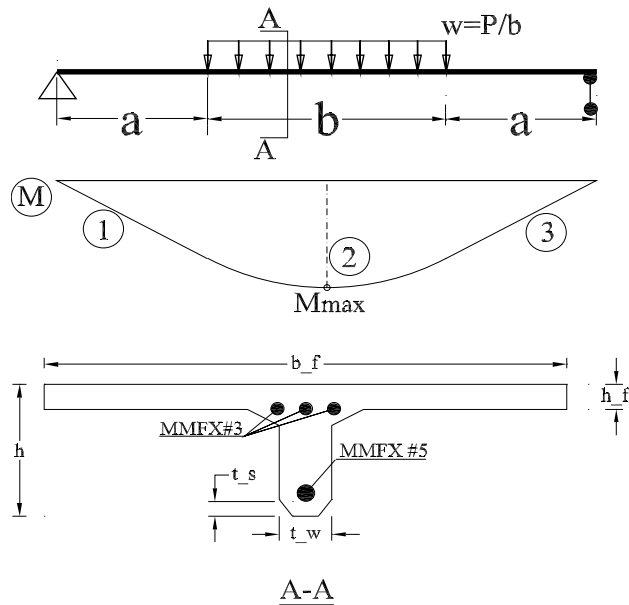


Figure 4.17: MMFX reinforced section with moment illustration

Apply all six boundary conditions (Eq. (4.2))

$$\left\{ \begin{array}{l} y_1(0) = 0 \\ y_3(L) = 0 \\ y_1(L1) = y_2(L1) \\ y_2(L1 + L2) = y_3(L1 + L2) \\ y_1'(L1) = y_2'(L1) \\ y_2'(L1 + L2) = y_3'(L1 + L2) \end{array} \right. \quad (4.2)$$

Since the maximum deflection occurs in the middle of the beam, the maximum deflection there

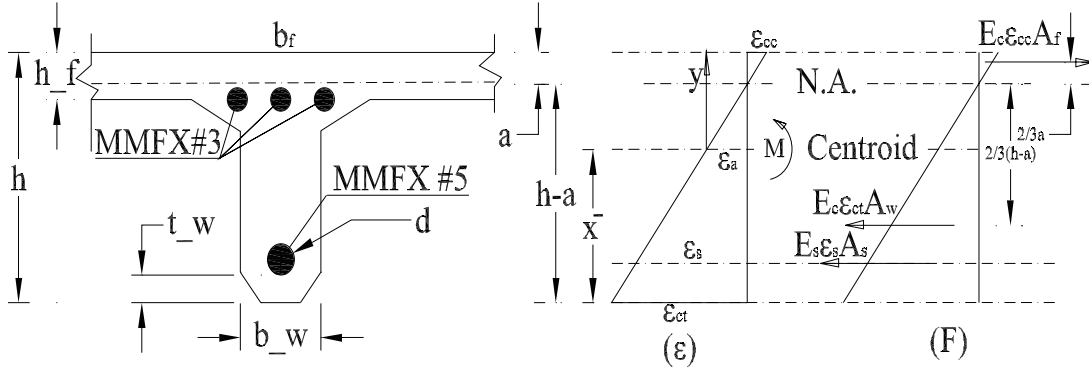


Figure 4.18: MMFX reinforced beam section analysis

can be found by using differential equations shown in Eq. (4.3):

$$E_{sys} I_{sys} y_{max} = \frac{64a^3 + 96a^2b + 40ab^2 + 5b^3}{384} P_m \quad (4.3)$$

where  $P_m$  is the relatively large load of two random data points selected in the elastic zone,  $y_{max}$  is the corresponding deflection with the load.  $E_{sys} I_{sys}$  is the MMFX reinforced beam system stiffness,  $b$  is the length of loading panel, and  $a$  is the distance from support to the loading panel as shown in Fig. 4.17

On the other side, for the single T section reinforced with MMFX illustrated in Fig. 4.18, set the strain at centroid position as  $\epsilon_a$ , strain at top of the flange as of  $\epsilon_{cc}$ , strain at bottom of web as of  $\epsilon_{ct}$ , and strain at the MMFX bar as of  $\epsilon_s$ , respectively. Apply the equilibrium equation as shown in Eq. (4.4):

$$E_c \epsilon_{ct} \frac{1}{2} (h - a) b_w + E_s \epsilon_s A_s = E_c \epsilon_{cc} \frac{1}{2} ab \quad (4.4)$$

where  $E_c$  and  $E_s$  are the modulus of elasticity of concrete and reinforced MMFX bar, respectively,

$h$  is the height of the section,  $a$  is the distance from top flange to neutral axis,  $b_w$  is the web width, and  $A_s$  is the area of the bottom reinforcing bar.

In addition, according to Fig. 4.18, find the moment at neutral axial of the section as expressed in Eq. (4.5):

$$E_c \epsilon_{ct} \frac{1}{2} (h - a) b_w \frac{2}{3} (h - a) + E_s \epsilon_s A_s (h - a - t_w - \frac{r}{2}) - E_c \epsilon_{cc} \frac{1}{2} a b \frac{2}{3} a = M_{exp} \quad (4.5)$$

where  $t_w$  is the width of bottom concrete cover and  $M_{exp}$  represents the experimental moment at the center of the beam span.

Furthermore, apply the geometrical relationship from the strain distribution illustration, the curvature  $\kappa$  can be expressed as in Eq. (4.6), meanwhile, the compression strain, tension strain, and bar strain can also be concluded as in Eq. (4.7).

$$\kappa = \frac{\epsilon_{ct}}{h - a} \quad (4.6)$$

$$\begin{cases} \epsilon_{cc} = \epsilon_a + (h - \bar{x})\kappa \\ \epsilon_{ct} = \epsilon_a - \bar{x}\kappa \\ \epsilon_s = \epsilon_a - (\bar{x} - t_w - \frac{r}{2})\kappa \end{cases} \quad (4.7)$$

Two pairs of data points were taken from the elastic portion of the specimen load-displacement response:  $P_m = 4.226$  kip and  $y_{max}$  of 0.1674 inch,  $P_m = 11.090$  kip and  $y_{max}$  of 0.3240 inch, respectively. Substitute into Eq. (4.3), then combine Eq. (4.4), Eq. (4.5), and Eq. (4.6) as well as Eq. (4.7). The solution yields values of  $E_c = 842$ ,  $a = 0.9321$ , and  $\epsilon_a = 0.008312$ . Applying the

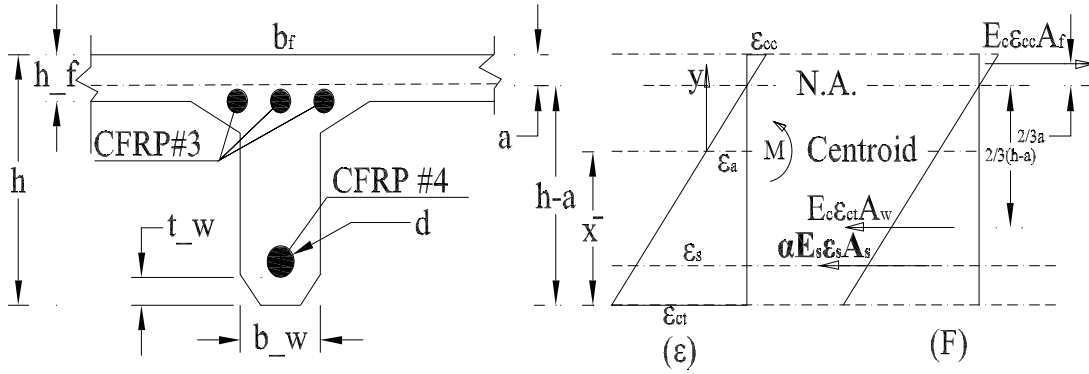


Figure 4.19: CFRP reinforced beam section analysis

section dimensions, it is easy to find the moment of inertia of the T section as  $26.189 \text{ in}^4$ , then compute the stiffness of UHPC as  $E_c I_c = 23306 \text{ k-in}^2$ .

Since the concrete stiffness is constant from the same batch, it should apply to the CFRP reinforced beam as well. As discussed previously, the CFRP bar strength was not fully mobilized due to the relatively large bar slip observed in the test. Hence, assume  $\alpha$  is the ratio of bar strength applied to the reinforced beam, repeat the above procedures with CFRP case as illustrated in Fig. 4.19, revise the force equilibrium equation and moment expression as shown in Eq. (4.8) and Eq. (4.9), respectively.

$$E_c \epsilon_{ct} \frac{1}{2} (h - a) b_w + \alpha E_s \epsilon_s A_s = E_c \epsilon_{cc} \frac{1}{2} ab \quad (4.8)$$

$$E_c \epsilon_{ct} \frac{1}{2} (h - a) b_w \frac{2}{3} (h - a) + \alpha E_s \epsilon_s A_s (h - a - t_w - \frac{r}{2}) - E_c \epsilon_{cc} \frac{1}{2} ab \frac{2}{3} a = M_{exp} \quad (4.9)$$

Substitute the calculated concrete modulus of elasticity obtained above ( $E_c = 842$ ) and the same geometric relationship equations presented previously as well as elastic point data from each CFRP

specimen. The computed curvature  $\kappa$ , neutral axis  $a$  (distance from top flange to neutral axial), and bar strength utilization ratio  $\alpha$  are summarized in Table 4.3.

Table 4.3: Estimated CFRP bar strength utilization ratio

Section	K	a	$\alpha$
CFRP 4"-1	0.002485	0.3484	54.8%
CFRP 4"-2	0.001952	0.4035	73.9%
CFRP 5"-1	0.001718	0.4447	44.8%
CFRP 5"-2	0.001344	0.4627	50.0%

It is obvious that there was only an average of 55% of the CFRP bar strength mobilized in the response of the reinforced beam. In order to reduce the bar slip of the CFRP reinforced section, which is considered the primary reason for the bar strength loss as well as to verify if an even more economical MMFX reinforced section would work, an additional batch of "T" section beams with both CFRP and MMFX reinforcement were casted and tested in September 2013. It was recorded as Cast II with illustration shown in Fig. 4.20). Testing of these beams was also performed at the FIU Structures Lab.

The section property of MMFX reinforced beam from the second cast has been adjusted with the section height decreased from 4.5 inch to 4 inch and the web width increased from 1.625 inch to 1.75 inch. Meanwhile, in order to avoid potential punching shear failure, additional ribs were created under the flange in the transverse direction. In addition, the panel weight and the total bridge deck weight based on the new optimized section was also estimated as listed in Table 4.4 where the estimated capacity from 1-D model was included as well.

The section property of CFRP reinforced beam from the second cast remains the same as that of the first cast except adopting a new anchorage system which consisted of a 10 inch long steel tube filled with an expansive grout at each end of the CFRP bars. Additional ribs also created under the flange by transverse direction and the new section estimation parameters were summarized in

Table 4.4: Section property of MMFX-4in specimen at second cast

Depth (in)	Width (of web) (in)	Panel weight with rib (psf)	Panel weight without rib (psf)	Total bridge deck weight with rib (psf)	Total bridge deck weight without rib (psf)
4.00	1.75	16.67	15.44	21.81	20.59
Demanded capacity				15524	
Established capacity from 1D model				18760	

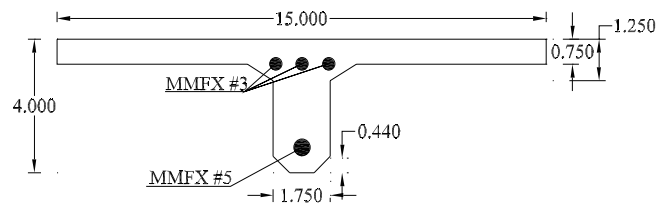
Table 4.5. The test result of load versus displacement relationship compared both from CFRP and MMFX was shown in Fig. 4.26.

Table 4.5: Section property of CFRP-4in specimen at second cast

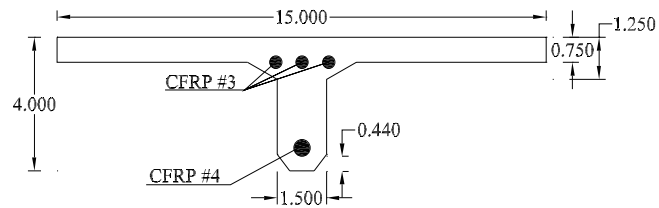
Depth (in)	Width (of web) (in)	Panel weight with rib (psf)	Panel weight without rib (psf)	Total bridge deck weight with rib (psf)	Total bridge deck weight without rib (psf)
4.00	1.5	14.73	13.51	19.24	18.02
Demanded capacity				15524	
Established capacity at 1D model				16523	
*Assume shear reduction factor of 0.2					

With the new anchorage system, there was no obvious bar slip observed in the test. By applying the calculation procedure discussed above, the new effective bar strength attribution ratio was found as listed in Table 4.6

It is seen from the results that the average bar strength utilization ratio with the first anchorage



Section MMFX4IN-2nd Cast



Section CFRP4IN-2nd Cast

Figure 4.20: Optimized section property for the second cast

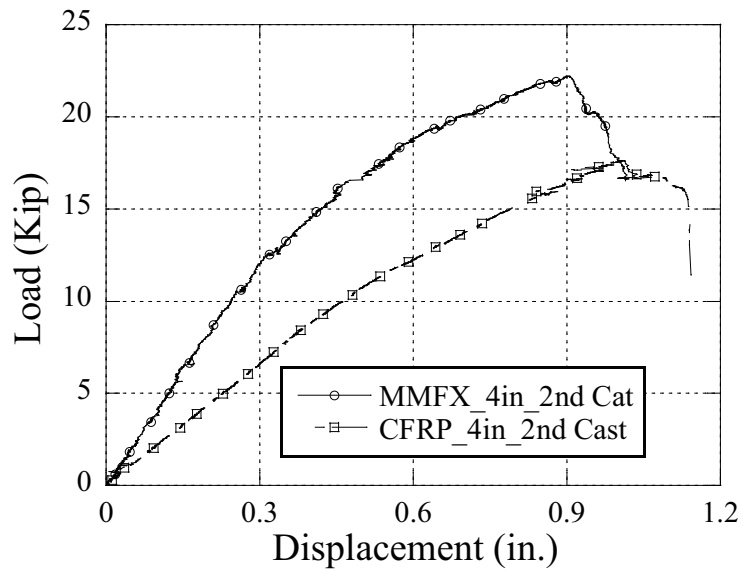


Figure 4.21: Load vs displacement compared with CFRP and MMFX beams at cast II



Table 4.6: Estimated CFRP bar strength utilization ratio from 2nd cast

Section	K	a	$\alpha$
CFRP 4"-1	0.001692	0.4349	84.8%

system was located approximately 64%. However, with the improved anchorage system, the ratio was upgraded significantly to around 85%. It gives the reason why the “UHPC-CFRP” specimens in the first cast had much lower strength capacity. Because the bar contribution was not effectively reflected once a critical slip occurred. Besides, the CFRP surface property might be another factor that influences the slippage. Since the plastic surface has less friction with concrete which means less boundary force. Hence, it is suggested that CFRP bar may be a qualified material for current project if the bar slippage issue can be well resolved.

#### *Shear reduction factor study*

The shear reduction factor of the lightweight aggregate concrete was proposed by the American Concrete Institute building code as 0.85 for sand-lightweight aggregate concrete and 0.75 for all other lightweight aggregate concrete [62]. In addition, Hanson [63], Ivey and Buth [64] proposed that the square root of concrete compression strength in the shear design equations can be replaced by  $f_{ct}/6.7$ . Ramirez et al. [65] revalidated the revised shear design equation for high strength lightweight aggregate concrete.

Since UHPC has no coarse aggregate, the factor from ACI might not be appropriate for use in UHPC design. In this section, the shear reduction factor based on “UHPC-MMFX” combined system will be estimated from the first cast specimens and then verified by specimen data obtained from the second cast.

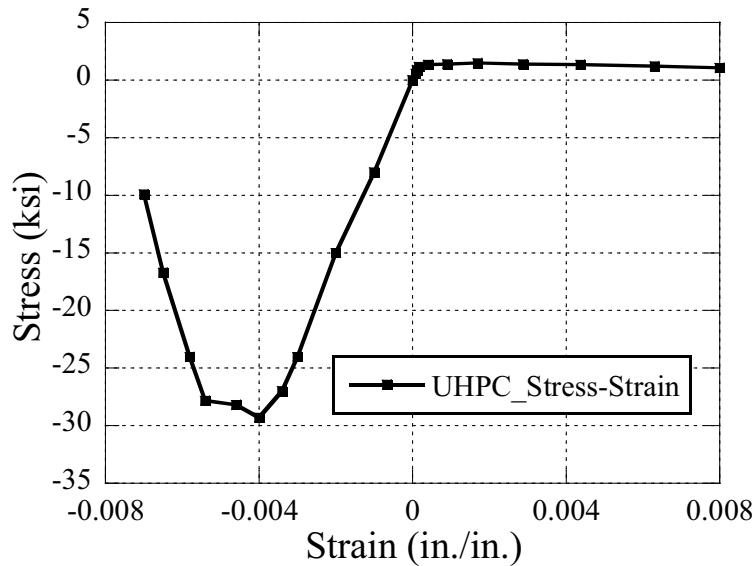


Figure 4.22: Stress-strain of UHPC adopted in OpenSees model

*Estimation of shear reduction factor with specimens from Cast I*

A one dimensional OpenSees model was created to simulate the moment curvature relationship from which the nominal moment can be obtained. Both compressive and tensile responses were considered for current model. The stress-strain data of UHPC as shown in Fig. 4.22 and MMFX as shown in Fig. 4.23 was obtained from previous literatures as well as official MMFX site, respectively.

Apply the MMFX reinforced section properties designed in cast I as shown previously, obtain the simulated moment curvature relationship from OpenSees model as shown in Fig. 4.24. The nominal moment was obtained as 407.6 k-in.

On the other side, the moment along the longitudinal direction of the “T” beam was expressed as in Eq. (4.1). Find the maximum moment in the middle of the beam as written in Eq. (4.10). The

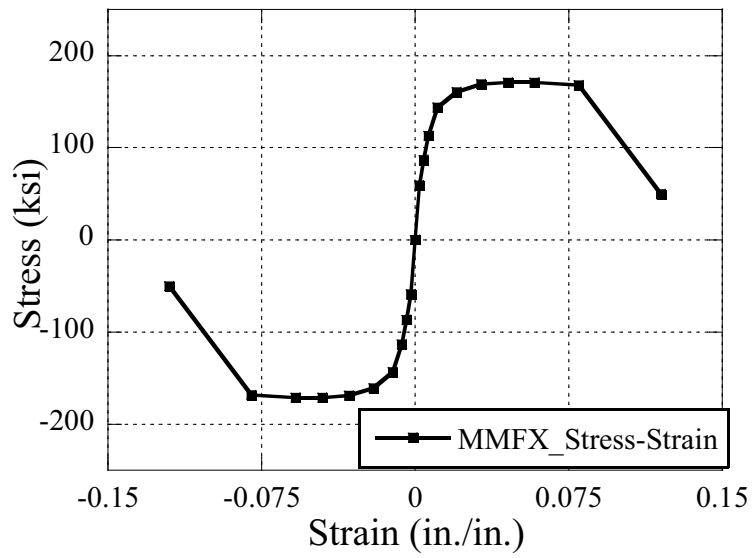


Figure 4.23: Stress-strain relationship of MMFX adopted in OpenSees model

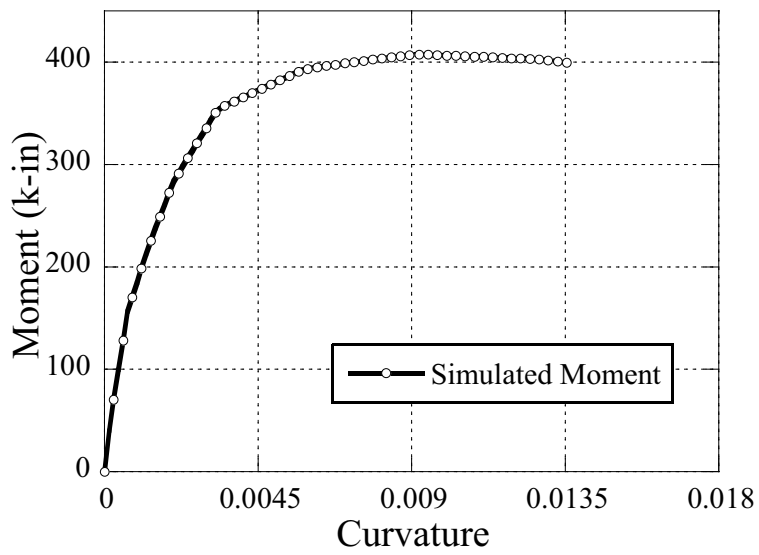


Figure 4.24: Simulated moment curvature of MMFX reinforced UHPC "T" section

corresponding simulated load and estimated shear reduction factor were summarized in Table 4.7

$$M_{max} = 107.5\omega \quad (4.10)$$

Table 4.7: Estimated shear reduction factors from Cast I specimens

Reinforcement	Specimen ID	Max. Test Load (k)	Max. Simulated Load (k)	Estimated Shear Reduction Factor ( $\beta$ )
MMFX	1	27.581	37.916	0.73
MMFX	2	24.595	37.916	0.65

E.g. the average shear reduction factor can be concluded as listed in Eq. (4.11)

$$\beta_{avg} = 0.69 \quad (4.11)$$

#### *Verification of shear reduction factor with specimen from Cast II*

As discussed previously, an optimized “UHPC-MMFX” section was casted as the second cast. Apply the optimized section properties to the created OpenSees model, obtain the simulated moment curvature as shown in Fig. 4.25. The nominal moment was obtained as 360.9 k-in.

Substitute the nominal moment from the optimized section into Eq. (4.10). By considering the estimated shear reduction factor listed above, the maximum force was predicted as shown in Eq. (4.12)

$$P_{pred.} = \beta \frac{M_{n2}}{107.5w} = 23.165k \quad (4.12)$$

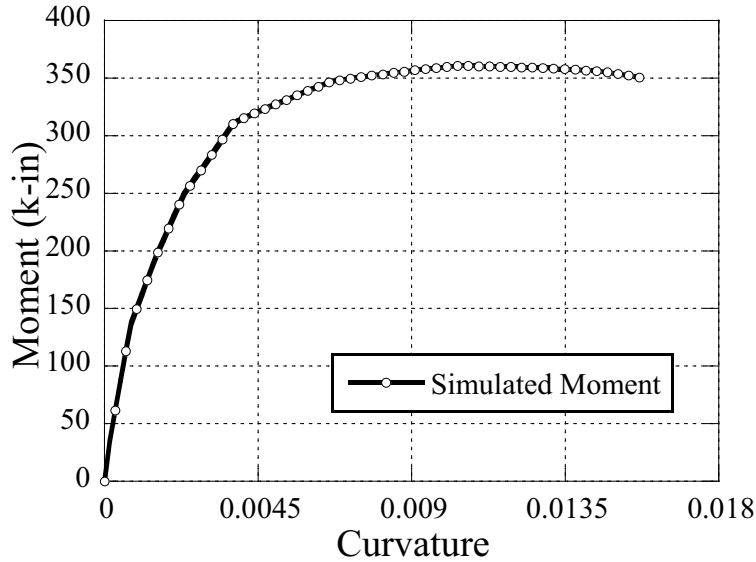


Figure 4.25: Simulated moment curvature of optimized MMFX reinforced “T” section

where  $\beta$  is the estimated shear reduction as shown previously;  $M_{n2}$  is the nominal moment obtained from the optimized “UHPC-MMFX” section;  $\omega$  is the vertical distributed load applied to the “T” section. Refer to Fig. 4.26, it is concluded that the maximum real load from the optimized section was obtained as 22.21kip which was quite close to the predicted number. Hence, the estimated shear reduction factor was reasonable and promising. A brief summary of details was listed in Table 4.8

Table 4.8: Predicted maximum peak load by using estimated shear reduction factor

Reinforcement	Specimen ID	Max. Test Load (k)	Max. Estimated Load (k)	Error in Percentage
MMFX	1	22.210	23.165	4.1%

Obviously, the shear reduction analysis presented above was analyzed with assured concrete section only. It contains constant length and reinforcement. Specifically, the reduction factor computed is based on the assumption that section property was the only one factor that influences the

maximum strength rather than considering other potential factors like reinforcing ratio and length-to-height ratio of the section. Hence, the listed estimation of shear reduction factor might be not adequate to reflect the accurate case. A 2-D low tension model might be required to develop the relationship on how other parameters influence the shear reduction factor in future study.

## **Chapter Discussion**

Compared with the proposed two CFRP systems from the first cast, the one with 4 in by depth was better because it saved more concrete material. The issue with relatively large deflection at service load level could be well improved by applying alternative anchorage system, for example, the anchorage system used during the second cast. Hence, the CFRP reinforced section with 4 in by height was suggested to select for future investigation on multiple continuous sections and spans in order to assess the responses at the negative moment region as well as figure out the load distribution factor.

While compared with both MMFX and CFRP reinforced systems from presented cast I and cast II as illustrated in Fig. 4.26, it was concluded that both of the designated CFRP and MMFX reinforcing beams met the targeted load capacity of 17 psf based on advised parameters even if there was no anchorage made for CFRP beams.

The more economic MMFX reinforced system from the second cast exhibited a lower peak capacity than that from the first cast, however, it still well qualified with the demand load which was located around 70% of the peak load. The deflection at service level of MMFX reinforced system from both two casts were close to each other and as low as 0.4 in. Therefore, the MMFX section design from the second cast was prioritized than that from the first cast.

Peak load from all three designed CFRP sections from both two casts passed the demand load

capacity. The section with the largest depth exhibited the highest load capacity. While compared the sections with the same parameters (e.g. CFRP-4in) from cast I and cast II, they exhibited almost the same peak load. However, the specimen from the second cast demonstrated the deflection with approximately 15% less which was directly attributed from the anchorage improvement.

At the demand load level, the MMFX reinforced section from the second cast reached a deflection close to 0.45 in while the CFRP reinforced section from the second casted reached a deflection of 0.85 in. Since both of the two deflections were under the allowed maximum deflection from American Association of State Highway and Transportation (AASHTO) criteria, the CFRP reinforced system tended to be a better choice than MMFX system for current project. Because CFRP bars had only around 25% of the weight of equivalent size of MMFX reinforcing bar which greatly brought down the weight of the total bridge deck system. Although the initial investment of CFRP system was more expensive than MMFX system, considering the average 30-50 years bridge service life, the CFRP system had a lower life cycle cost due to the low maintenance cost which was benefited from its non corrosive nature and high resistance to chloride ion attack.

The bar strength utilization study gave an approximate strength ratio when CFRP bar enrolled in beam design. The ratio generally was dependent on the anchorage approach applied which was considered as a challenge in design with CFRP reinforcing bar. The computed ratio would give a rough guidance for future design as well.

The shear reduction factor was also focused in this chapter and the factor was verified as even lower than the conservative number of 0.75 suggested by ACI code based on conventional concrete. It should be due to the particular properties of UHPC. A number of 0.68 was suggested to use for future UHPC related beam designs. However, it should be categorically stated that this factor was experimentally derived and contains other factors such as the difference between analytical and experimental responses. Therefore, the true shear reduction factor is likely considerably larger

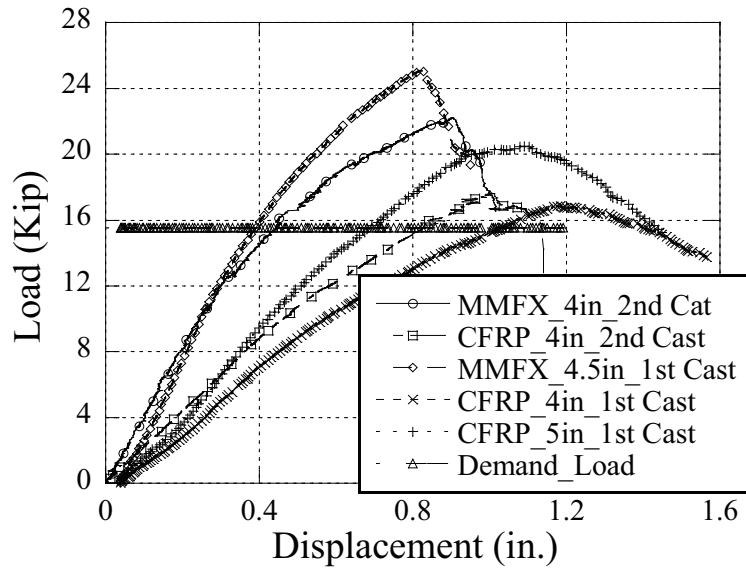


Figure 4.26: Load vs displacement of CFRP and MMFX system at both two casts

than 0.68.



## CHAPTER 5: CONCLUSION

In current research, three structural engineering issues titled dowel action performance, fatigue response and “T” section beam optimization were successfully investigated. The ultra-high performance concrete (UHPC) was used for all three tests and both of two specific bars of MMFX bar and CFRP bar were used as reinforcement where required. These three tests together are trying to further understand the static and fatigue behavior of the passively reinforced UHPC beams, which fail in a ductile shear mode.

Typically, the investigation could include but not limit to the following conclusions:

- 1) A pure dowel action test was successfully completed and the test indicated a peak dowel force as high as 2.88 kip for the regular group specimens (half length) with appropriate parameters in dimensions as well as debond between UHPC and the reinforcing bar.
- 2) The contrast group with well bond between UHPC and reinforcing bar indicated a peak dowel force as of 4.84 kip which is around 68.1% higher than the situation when no bond considered. It means the bond capacity improves dowel force significantly.
- 3) The UHPC tensile modulus was computed through the analysis of dowel action test data and it gives a fundamental guideline for future finite element model simulation on shear strength prediction with even higher accuracy.
- 4) The four designated variables such as concrete block length, reinforcing bar size, concrete side cover and concrete bottom cover were confirmed as impact factor on dowel force resistance. A longer concrete bar indicated a higher tensile modulus  $\beta$  which lead to a higher dowel load and a thicker concrete bottom cover also drove the higher dowel force. On the other side, the side cover as less as 0.5 in had quite limit influence on the ultimate dowel force and the dowel bar size trended no big contribution on the maximum dowel force.
- 5) The fatigue response of component made of UHPC under pure tensile load was performed and

four analysis approaches such as peak strain approach, mean strain approach and maximum vertex strain approach as well as mean stress approach were presented to estimate the material S-N curve. An additional Opensees model was also created to well present the real performance on specimen subjected to unexpected rotation moment or eccentricity. Compared with all of these four approaches, the maximum vertex strain approach performed the best estimation since it effectively considered the eccentricity issue occurred in the test.

6) The linear S-N curve under uniaxial tensile test with UHPC was estimated and it can be involved into the bridge deck design discussed in chapter 4 when life time durability considered.

7) The tests on the additional “T” section beams demonstrated the effects of using different types of reinforcement and revealed the importance of bond strength between rebar and the surrounding UHPC portion. If the bond strength is low, such as what happened in the CFRP reinforced UHPC beams, the capacity will be much lower than the estimated strength from either flexural design or shear design.

8) A shear reduction factor was estimated from the real UHPC “T” beam study and the factor is lower than the number suggested by AASHTO on normal concrete. The study gives fundamental guidance for future UHPC involved economic design.

**APPENDIX A: SAMPLE UHPC APPLICATIONS WORLDWIDE**

## LOUIS VUITTON FOUNDATION FACADE

For this large project, nearly 130,000-square-foot, 150-foot-tall building is moving a head since 2006 and is slated for completion in 2012. Lafarge has been working with the building's project team and Ductal UHPC is used for the project. The foundation's concrete facade will require 16,000 exterior wall panels, each with its own geometry to match the curves of the nearly 97,000-square-foot glass facade. A vacuum-casting process was proposed by Lafarge and its partner Cogitech and project management consortium RFR/TESS. The technology combines a flexible mold that can take on any curvature determined by a 3-D model with a master polystyrene template machined to the desired panel geometry. Named Moulage Sous Vide (MSV). A brief summary of the project is listed in Table 1. Some photos from the project are shown in Figures 1 and 2.

Using the MSV process, ultimately 400 panels with identical dimensions were manufactured, but completely unique curvatures, that were installed in a full-scale first run model at the building site in September 2010. After undergoing the MSV process, each Ductal panel is cured for 20 hours, then mapped to produce a 3-D report of its shape and ensure it is within 1 millimeter tolerance. The 35-pound segments are approximately 4.9 feet long by 1.3 feet high, and less than an inch thick. Because no two are alike, they are cast with a number and a radio frequency ID chip to ensure each can be traced throughout the installation process, which began this spring, and for maintenance in the future.

Table 1: SUMMARY OF LOUIS VUITTON FOUNDATION FACADE

Project Name	Year	Country	Location	Project Size	Remarks
Louis Vuitton Foundation	2006 – 2012	France	Northern entrance of Paris	Large scale structure	Ongoing project photo courtesy: Lafarge

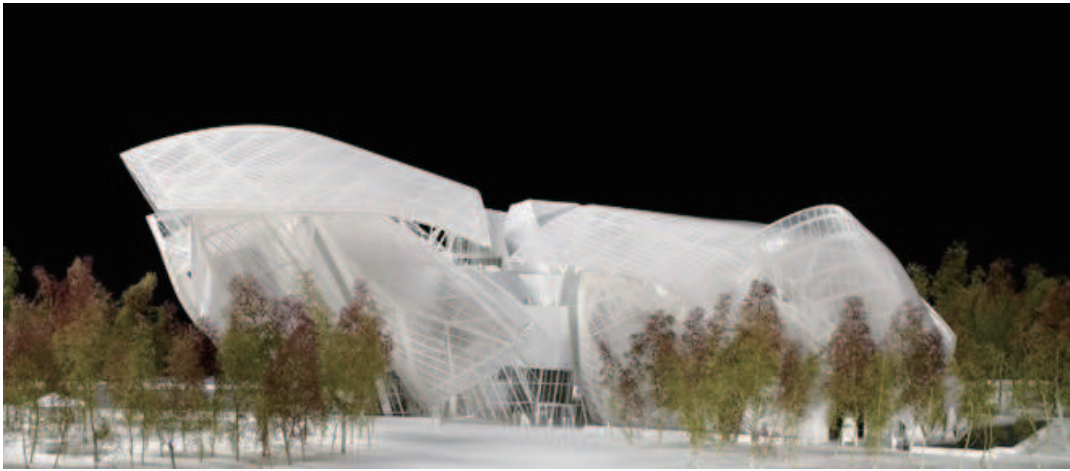


Figure 1: LOUIS VUITTON FOUNDATION OVERVIEW PHOTO 1

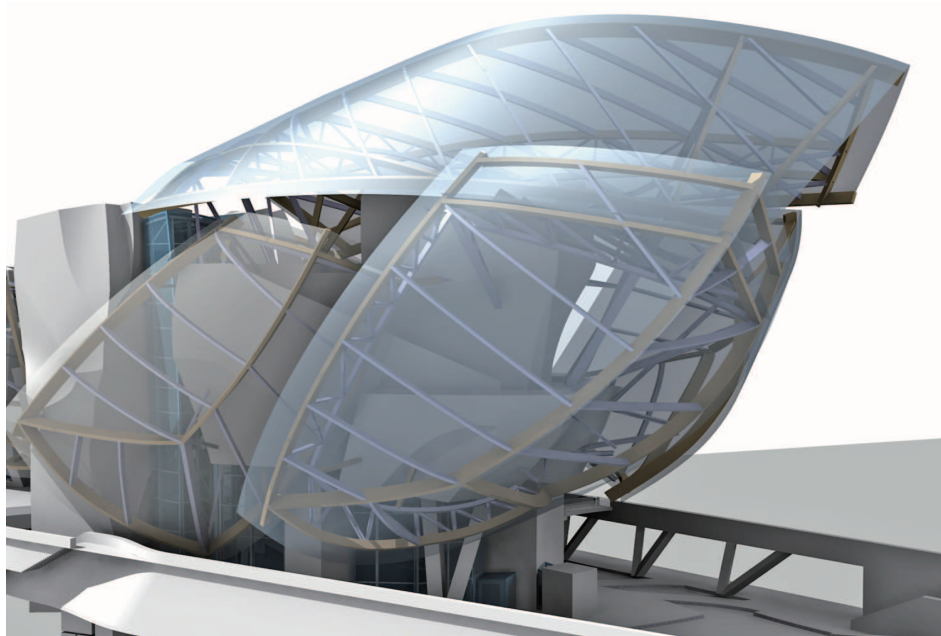


Figure 2: LOUIS VUITTON FOUNDATION OVERVIEW PHOTO 2

## SHAWNESSY LIGHT RAIL TRANSIT STATION

The project was constructed as a part of southern expansion to Calgary’s LRT system and is the world’s first LRT system to be constructed with UHPC (Table 2). The station features 24 thin-shelled canopies, 5.1 m by 6 m (16.7 ft by 19.7 ft), and just 20 mm (0.79 in.) thick, supported on single columns, protect commuters from the elements. UHPC technology has a unique combination of superior technical characteristics including ductility, strength, and durability, while providing highly moldable products with a high quality surface aspect. The contract document specified a minimum requirement of 130 MPa (19,000 psi). In addition to the canopies, the components include struts, columns, beams, and gutters. The volume of material used totaled 80 m<sup>3</sup> (105 yd<sup>3</sup>). Some photos from the project are shown in Figures 3 and 4.

Table 2: SUMMARY OF SHAWNESSY LIGHT RAIL TRANSIT STATION

Project Name	Year	Country	Location	Project Size	Remarks
The Shawnessy Light Rail Transit Station	2003 – 2003	Canada	Calgary	Large scale structure	Finished Project photo courtesy: Portland Cement Association

## THE JAKWAY PARK BRIDGE

It is the first North American highway bridge built with UHPC PI-girders, the first highway bridge to incorporate UHPC batched in a ready-mix concrete truck, and only the third in North America built with UHPC girders (Table 3). "Ductal" was used for the project and compressive strength of the beams in the bridge was 21,500 psi (final). The project received an "Iowa Quality Initiative Structures Research Merit Award" from the Associated General Contractors of Iowa (AGCI) and the Iowa Department of Transportation (IDOT). This three-span bridge is 112 ft 4 in. long and 24



Figure 3: THE SHAWNESSY LIGHT RAIL TRANSIT STATION PHOTO 1

ft 3 in. wide. The UHPC center span is 51 ft 2 in. It includes three precast, prestressed UHPC PI-girders and a cast-in-place slab. The girders are called "PI"-girders because their cross-section resembles the Greek letter "pi". The bridge opened to traffic on November 26, 2008 and an official ribbon cutting ceremony took place on April 15, 2009. Some photos from the project are shown in Figures 5 and 6.

Table 3: SUMMARY OF THE JAKWAY PARK BRIDGE

Project Name	Year	Country	Location	Project Size	Remarks
The Jakway Park Bridge	2008	United States	Buchanan County, Iowa	Large scale structure	Finished Project photo courtesy: Portland Cement Association



Figure 4: THE SHAWNESSY LIGHT RAIL TRANSIT STATION PHOTO 2



Figure 5: THE JAKWAY PARK BRIDGE PHOTO 1

### **MARS HILL BRIDGE IN WAPELLO COUNTY**

It was the first bridge in the United States to use UHPC (Table 4). The bridge comprises 110-ft-long precast concrete modified 45-in-deep Iowa bulb-Tee beams topped with a cast-in-place concrete bridge deck. The concrete offers such considerable strength that the beams were built without any shear reinforcement. "Ductal" supplied by Lafarge North America was used to achieve up





Figure 6: THE JAKWAY PARK BRIDGE PHOTO 2

to 30,000 psi compressive strengths, with ductility. The material provides a real synergy with the pre-stressed concrete industry and also an opportunity to create slender, long-span beams and more graceful bridges without the need for reinforcing bars. In addition, the speed with which the bridge was completed after the testing was verified. Casting the 110-ft-long beams was completed in June and July of 2005, and construction began in August. By the following February, the bridge was opened to traffic. The beam spacing was 9-ft 7-in, with 4-ft overhangs, creating a 24-ft 6-in wide completed structure. Some photos from the project are shown in Figures 7 and 8.

Table 4: SUMMARY OF MARS HILL BRIDGE IN WAPELLO COUNTY

Project Name	Year	Country	Location	Project Size	Remarks
Mars Hill Bridge	2006	United States	Wapello County, Iowa	Large Scale Construction	Finished Project photo courtesy: Wayne A. Endicott



Figure 7: MARS HILL BRIDGE IN WAPELLO COUNTY PHOTO 1



Figure 8: MARS HILL BRIDGE IN WAPELLO COUNTY PHOTO 2

## ARCHITECTURE AND ARTS DESIGN

Ductal has tremendous creative and imitative capacities, making it an exceptional material choice for walls, partitions, parquets, floor slabs, hanging ceilings, etc (Table 5). Thinness and elegance, two of Ductal’s traits, have inspired many new interior designs, that are not typical of original, conventional concrete creations. With Ductal’s unique combination of superior properties, you can create new designs and elements with an exceptional range of potential textures and forms. Leather, fabric and crocodile skin are just some of the finishes imagined by decorators to clad the walls of luxury boutiques or contemporary interiors. This innovative decorative development that relies on Ductal’s resistance, low porosity, watertight matrix and low maintenance can be used in many different areas and applications. Ductal could be the ideal, custom “made-to-order” material that designers have been dreaming of. Some photos from the project are shown in Figures 9 and 10.

Table 5: ARCHITECTURE AND ARTS DESIGN

Project Name	Year	Country	Location	Project Size	Remarks
Architecture and arts designs	Recent years	France	France	Small to medium	Photos courtesy: Lafarge

## THE SHEPHERDS CREEK DUCTAL BRIDGE

It is the world’s first bridge for normal highway traffic to be constructed using Ductal (Table 6). It has a single span of 15m with a 16 degree skew. The superstructure consists of 16 precast prestressed Ductal I-beam and an in-situ 170mm-thick reinforced concrete deck slab. The slab was placed onto thin precast Ductal permanent formwork panels that span between the beams and pro-



Figure 9: BUS SHELTERS MADE OF UHPC



Figure 10: BMI AZULY STREET FURNITURE MADE OF UHPC

vide an additional measure to protect the ordinary concrete slab from the environment of the creek below. The beam have an I-section shape with a total depth of 600mm and are spaced at 1.3m. the formwork slabs are 1.1m wide and 2.4m long, with a thickness of just 25mm. These slabs contain no additional reinforcement. The construction of the bridge followed the dame procedures as in the use of conventional concrete beams and slabs. The beams have the significant advantage that they weigh only 4.2t (280kg/m) for a length of 15.1m compared with about 9t for a conventional prestressed concrete beam. The permanent formwork slabs have the advantage of being extremely light and providing a highly-durable soffit to the deck. Some photos from the project are shown in Figures 11 and 12.

Table 6: THE SHEPHERDS CREEK DUCTAL BRIDGE

Project Name	Year	Country	Location	Project Size	Remarks
Shepherds Bridge	2005	Australia	New South Wales	Large scale Construction	Photos courtesy: Roads and Traffic Authority (RTA)



Figure 11: THE SHEPHERDS CREEK DUCTAL BRIDGE PHOTO 1



Figure 12: THE SHEPHERDS CREEK DUCTAL BRIDGE PHOTO 2

## LIST OF REFERENCES

- [1] National Transportation Statistics from U.S. Department of Transportation. Research and innovative technology administration.
- [2] Dayton Superior Corporation. Bridge deck overlay system.
- [3] A. Mirmiran, A. Saleem, K. Mackie, and J. Xia. Alternatives to steel grid decks. Technical Report FDOT Project No. BD015 PRWO 22, 2009.
- [4] A. Mirmiran, A. Saleem, P. Zohrevand, K. Mackie, J. Xia, and Y. Xiao. Alternatives to steel grid decks–Phase ii. Technical Report FDOT Project No BDK80 977-06, 2012.
- [5] J. Xia and et al. Shear failure analysis on ultra-high performance concrete beams reinforced with high strength steel. *Engineering Structures*, 33(12):3597–3609, 2011.
- [6] American Society for Testing and Materials, West Conshohocken, PA, USA. *ASTM A 1035 (2006), Standard Specification for Deformed and Plain, Low-carbon, Chromium, Steel Bars for Concrete Reinforcement*, 2006.
- [7] Hughes Brothers Inc. Aslan 200 mechanical properties - tensile, modulus and strain.
- [8] French Association Francise deGenie Civil, Paris, France. *Ultra High Performance Fiber-Reinforced Concretes-Interim Recommendations*, 2002.
- [9] A. Tafraoui and et al. Metakaolin in the formulation of uhpc. *Construction and Building Materials*, 23(2):669–674, 2009.
- [10] T.M. Ahlborn, E.P. Steinberg, and J. Hartmann. Ultra-high performance concrete -study tour 2002. Orlando, Florida, 2003. 3rd PCI / FHWA International Symposium On High Performance Concrete.

- [11] Y. Jian and F. Zhi. Shear failure analysis on ultra-high performance concrete beams reinforced with high strength steel. *China Railway Science*, 30(2), 2009.
- [12] B. Graybeal and J. Tanesi. Durability of an ultra-high performance concrete. *Materials in Civil Engineering*, 19(10), 2007.
- [13] J. Ma and Orgass. Creep of ultra high performance concrete. *LACER*, 10, 2005.
- [14] P. Richard and M. Cheyrezy. Reactive powder concretes with high ductility and 200-800 mpa compressive strength. *Concrete technology: past, present, and future*, ACI SP 144:507–18, 1993.
- [15] A. Feylessoufi and et al. Controlled rate thermal treatment of reactive powder concretes. *Adv Cem Based Mater*, 6(1):21-7.7, 1997.
- [16] B Graybeal. Characterization of the behavior of ultra-high performance concrete. *PhD thesis, University of Maryland*, 2005.
- [17] S. Collepardi and et al. Mechanical properties of modified reactive powder concrete. *Superplasticizers and other chemical admixtures in concrete*, ACI SP 173, 1997.
- [18] K. Habel, E. Denarie, and E. Bruhwiler. Experimental investigation of composite ultra-high-performance fiber-reinforced concrete and conventional concrete members. *Structural Journal*, 104(1), 2007.
- [19] K. Habel and et al. Development of the mechanical properties of an ultra-high performance fiber reinforced concrete (uhpfr). *Cement and Concrete Research*, 36(7), 2006.
- [20] B. Graybeal and J. Tanesi. Durability of an ultra-high performance concrete. *Materials in civil engineering*, 19(10), 2007.



- [21] B. Graybeal. Structural behavior of ultra-high performance concrete prestressed concrete i-girders. *FHWA-HRT-06-115, Editor. 2006*, 2006.
- [22] AASHTO. Bridge design specifications and commentary. *A.A.O.S.H.T. Officials*, 2007.
- [23] B. Graybeal and J. Hartmann. Experimental testing of uhpc optimized bridge girders: Early results. in pci national bridge 2005. Technical report, Palm Springs, California, 2005.
- [24] B. Graybeal. Uhpc making strides. in *72-4, P. Roads, Editor*, 2009.
- [25] Ben Graybeal. *Ultra-High Performance Concrete*. FHWA.
- [26] MMFX Steel Corporation of America. *MMFX2 Steel Concrete Reinforcing and Pavement Dowel Bars*. Product Guide.
- [27] Jan-Olof Sperle and Kennet Olsson.
- [28] Chris Kern. *Fastener Technology International*.
- [29] Hatem Seliem, Gregory Lucier, Sami Rizkalla, and Paul Zia. *Behavior of Concrete Bridge Decks Reinforced with MMFX Steel*. Springer Netherlands.
- [30] A Carpinteri, B Chiaia, and G Ferro. Size effect on nominal strength of concrete structures: Multifractality of material ligaments and dimensional transition from order to disorder. *Materials and Structures*, 28:311–317, 1995.
- [31] R Ince and E Arici. Size effect in bearing strength of concrete cubes. *Construction and Building Materials*, 18, 2004.
- [32] Jin-Keun Kim and Yon-Dong Park. Prediction of shear strength of reinforced concrete beams without web reinforcement. *ACI Materials Journal*, 93(3):213–222, 1996.

- [33] Ragip Ince, Erhan Yalcin, and Abdussamet Arslan. Size-dependent response of dowel action in R.C. members. *Engineering Structures*, 29:955–961, 2006.
- [34] P. Soroushian, K. Obaseki, and M.C. Rojas. Bearing strength and stiffness of concrete under reinforcing bars. *ACI Materials*, 84(3), 1987.
- [35] B.F. Friberg. Design of dowels in transverse joints of concrete pavements. *Transactions, American Society of Civil Engineers*, 105, 1940.
- [36] P. Soroushian. Behavior of bars in dowel action against concrete cover. *ACI Structural Journal*, 84(2):170–176, 1987.
- [37] Bilal El-Ariss. Behavior of beams with dowel action. *Engineering Structures*, 29(6):899–903, 2007.
- [38] Helen Dulacska. Dowel action of reinforcement crossing cracks in concrete. *ACI Materials Journal*, 69(12):754–757, 1972.
- [39] Karl-Heinz Reineck. Ultimate shear force of structural concrete members without transverse reinforcement derived from a mechanical model. *ACI Structural Journal*, 88(5):592–602, 1991.
- [40] X. G. He and A. K. H. Kwan. Modeling dowel action of reinforcement bars for finite element analysis of concrete structures. *Computers and Structures*, 79(6):595–604, 2001.
- [41] Swati Roy Maitra, K. S. Reddy, and L. S. Ramachandra. Load transfer characteristics of dowel bar system in jointed concrete pavement. *Journal of Transportation Engineering*, 135(11):813–821, 2009.
- [42] T.D. Bush and S.M. Mannava. Measuring the deflected shape of a dowel bar embedded in concrete. *Experimental Techniques*, 24(3):33–36, 2000.

- [43] Muhammad Azhar Saleem, Amir Mirmiran, Jun Xia, and Kevin Mackie. Ultra-high-performance concrete bridge deck reinforced with high-strength steel. *ACI Structural Journal*, 108(5):601–609, 2011.
- [44] M. Hetenyi. *Beams on elastic foundation; theory with applications in the fields of civil and mechanical engineering*. The University of Michigan press, 1946.
- [45] Benjamin A Graybeal. Material property characterization of ultra-high performance concrete. Technical Report FHWA-HRT-06-103, Federal Highway Administration, 2006.
- [46] C. R. Rilem. Long term random dynamic loading of concrete structures. *Material Structure*, 17(97), 1984.
- [47] L. Gao and T. Hsu. Fatigue of concrete under uniaxial compression cyclic loading. *ACI Materials*, 95(5)(575), 1998.
- [48] H. Horii, H. Shin, and T. Pallewatta. Mechanism of fatigue crack growth in concrete. *Cement Concrete Composite*, 14(83), 1992.
- [49] Paris PC. *The growth of fatigue cracks due to variation in load*. PhD thesis, Lehigh University, Bethlehem, PA, 1962.
- [50] Paris P and Erdogan F. A critical analysis of crack propagation laws. *American Society of Mechanical Engineering*, 34, 1963.
- [51] Subramaniam KV, O’Neil E, popovics JS, and Shah SP. Flexural fatigue of concrete: experiments and theoretical model. *ASCE*, 891-8, 2000.
- [52] E. Su and T. Hsu. Biaxial compression fatigue and discontinuity of concrete. *ACI Materials*, 3(78), 1988.

- [53] W. Yin and T. Hsu. Fatigue behavior of steel fiber reinforced concrete in uniaxial and biaxial compression. *ACI Materials*, 92(1), 1995.
- [54] J. L. Van Ornum. Fatigue of cement products. *Transactions, American Society of Civil Engineers*, 51:443, 1903.
- [55] G. M. Nordby. Fatigue of concrete - a review of research. *American Concrete Institute*, 30(5):191–215, 1958.
- [56] M. Behloul and et al. Fatigue flexural behavior of pre-cracked specimens of special uhpfrc. *Special Publication*, 228, 2005.
- [57] Klausen D. and Weigler H. Fatigue behavior of concrete - effect of loading in the fatigue strength range. *Betonwerk Fertigteil-Tech*, pages 214–220, 1979.
- [58] Benjamin Graybeal and Justin Ocel. Fatigue behavior of an ultra-high performance concrete i-girder. Technical Report Concrete Bridge Conference, 2007.
- [59] M. Saito. Characteristics of microcracking in concrete under static and repeated tensile loading. *Cement Concrete Res*, 17(211), 1987.
- [60] C. HAW. Fatigue failure of concrete in tension. *HERON*, 29(4), 1984.
- [61] J. Zhang, H. Stang, and V.C. Li. Experimental study on crack bridging in frc under uniaxial fatigue tension. *Material in civil engineering*, 2000.
- [62] ACI Committee 318. Building code requirements for structural concrete (aci 318-05) and commentary (aci 318r-05). *American Concrete Institute, Farmington Hills, Mich.*, page 430, 2004.
- [63] J. A. Hanson. Tension strength and diagonal tension resistance of structural lightweight concrete. *ACI Journal Proceedings, Farmington Hills, Mich.*, 58:1–37, July 1961.

- [64] D. L. Ivey and E. Buth. Shear capacity of lightweight concrete beams. *ACI Journal Proceedings*, Farmington Hills, Mich., 64:634–643, Oct. 1967.
- [65] J. A. Ramirez, J. Olek, and B. J. Malone. High-performance structural lightweight concrete. *American Concrete Institute, Farmington Hills, Mich.*, pages 69–90, 2004.